

Copyright Warning & Restrictions

The copyright law of the United States (Title 17, United States Code) governs the making of photocopies or other reproductions of copyrighted material.

Under certain conditions specified in the law, libraries and archives are authorized to furnish a photocopy or other reproduction. One of these specified conditions is that the photocopy or reproduction is not to be “used for any purpose other than private study, scholarship, or research.” If a user makes a request for, or later uses, a photocopy or reproduction for purposes in excess of “fair use” that user may be liable for copyright infringement,

This institution reserves the right to refuse to accept a copying order if, in its judgment, fulfillment of the order would involve violation of copyright law.

Please Note: The author retains the copyright while the New Jersey Institute of Technology reserves the right to distribute this thesis or dissertation

Printing note: If you do not wish to print this page, then select “Pages from: first page # to: last page #” on the print dialog screen

The Van Houten library has removed some of the personal information and all signatures from the approval page and biographical sketches of theses and dissertations in order to protect the identity of NJIT graduates and faculty.

ABSTRACT

REACTIVE IRON MINERAL COATINGS IN REDOX TRANSITION ZONES OF A SITE WITH HISTORICAL CONTAMINATION: ABIOTIC ATTENUATION

by
Xin Yin

Reactive iron mineral coatings are found throughout reduction-oxidation (redox) transition zones and play a significant role in contaminant transformation processes. In this study, an 18.3-meter core is collected, subsampled, and preserved under anoxic conditions to maintain its original redox state. Screening analyses are conducted at sampling increments of 5.08 cm in depth for the following: elemental concentrations with X-ray fluorescence (XRF), sediment pH, sediment oxidation-reduction potential (ORP), total volatile organic carbon (TVOC) in the sample headspace, and abundant bacteria (16S rRNA sequencing). Using the Fe and S gradients correlated with microbial data, five RTZs are delineated. To characterize iron mineral speciation, a six-step sequential extraction is applied in four out of the five RTZs. Based on extraction results, amorphous Fe sulfide minerals, mackinawite and greigite, increase with depth in the Upper Zone, the shallowest RTZ. Because of the abundance of these amorphous minerals and given the extent of contamination at the site, the absence of volatile organic compounds in the sediment headspace suggests (a)biotic attenuation may be significant. In Zone 1, crystalline Fe sulfide mineral nano-coatings are abundant in the presence of sulfate-reducing bacteria *Desulfosporosinus*. In Zone 2, the Fe(II/III) mineral magnetite is dominant, suggesting a biogenic pathway as the iron-reducing bacteria, *Geobacter*, is abundant. Fe mineral coatings in Zone 3 reveal significant variability between each subsample, indicating active Fe cycling with biotic processes

based on the abundance of *Desulfosporosinus* bacteria in the clay lenses. Reactive iron mineral coatings in RTZs supports evidence of (a)biotic processes in natural attenuation.

To understand the contribution of these Fe reactive coatings to attenuation of chlorinated solvents, a bench study is designed for reductive 1,4-dichlorobenzene (1,4-DCB), tetrachloroethylene (PCE), and trichloroethylene (TCE) degradation. Control groups included pure pyrite and siderite minerals. For 1,4-DCB treatment, although dechlorination is not observed over the time period of the study in the control groups, reaction kinetics with RTZ sediments followed second order rate expressions. Chlorobenzene and benzene are detected as byproducts, suggesting hydrogenolysis reduction. The second-order rate constants for the Fe(II) mineral nano-coatings in 1,4-DCB degradation are $1.73 \times 10^{-3} \text{ L g}^{-1} \text{ h}^{-1}$ for pyrite (FeS_2), $1.24 \times 10^{-3} \text{ L g}^{-1} \text{ h}^{-1}$ for mackinawite (FeS), $1.89 \times 10^{-4} \text{ L g}^{-1} \text{ h}^{-1}$ for siderite (FeCO_3), and $1.79 \times 10^{-4} \text{ L g}^{-1} \text{ h}^{-1}$ for magnetite (Fe_3O_4). The high reactivity of these nano-Fe mineral coatings is due to their large surface areas. PCE and TCE reduction are observed in the control and sediment groups, also following second-order rate expressions. Rate constants are of the same order of magnitude for the mineral coating contributions ranging from $(2.45 \pm 0.41) \times 10^{-3}$ to $(4.00 \pm 0.74) \times 10^{-3} \text{ h}^{-1}$. Given the rate constants found, 90% degradation of these COCs occurs over 24 to 39 days demonstrating the importance of these abiotic processes. For these three chlorinated solvents, the trend for abiotic processes with Fe(II) mineral nano-coatings follows: Fe(II) sulfide minerals > magnetite > siderite. As a result, reactive Fe mineral nano-coatings are expected to play an important role in the attenuation of chlorinated solvents in contaminated subsurface environments.

**REACTIVE IRON MINERAL COATINGS IN REDOX TRANSITION ZONES OF
A SITE WITH HISTORICAL CONTAMINATION: ABIOTIC ATTENUATION**

by
Xin Yin

**A Dissertation
Submitted to the Faculty of
New Jersey Institute of Technology
in Partial Fulfillment of the Requirements for the Degree of
Doctor of Philosophy in Environmental Engineering**

John A. Reif, Jr. Department of Civil and Environmental Engineering

May 2022

Copyright © 2022 by Xin Yin

ALL RIGHTS RESERVED

APPROVAL PAGE

REACTIVE IRON MINERAL COATINGS IN REDOX TRANSITION ZONES OF A SITE WITH HISTORICAL CONTAMINATION: ABIOTIC ATTENUATION

Xin Yin

Dr. Lisa B. Axe, Dissertation Advisor Date
Professor and Chair, Department of Chemical and Materials Engineering, NJIT

Dr. Michel Boufadel, Committee Member Date
Professor, Department of Civil and Environmental Engineering, NJIT

Dr. Wen Zhang, Committee Member Date
Associate Professor, Department of Civil and Environmental Engineering, NJIT

Dr. Lucia Rodriguez-Freire, Committee Member Date
Assistant Professor, Department of Civil and Environmental Engineering, NJIT

Dr. Donna E. Fennell, Committee Member Date
Professor and Chair, Department of Environmental Sciences, Rutgers University,
New Brunswick, NJ

Dr. James Dyer, Committee Member Date
Savannah River National Laboratory, Aiken, SC

BIOGRAPHICAL SKETCH

Author: Xin Yin
Degree: Doctor of Philosophy
Date: May 2022

Undergraduate and Graduate Education:

Doctor of Philosophy in Environmental Engineering,
New Jersey Institute of Technology, Newark, NJ, 2022

Bachelor of Science in Water Supply and Drainage Engineering,
Guangdong Institute of Technology, Guangzhou, P.R. China, 2014

Major: Environmental Engineering

Presentations and Publications:

Yin, X., Hua, H., Burns, R.F., Fennell, D., Dyer, J.A., Landis, R., Axe, L. Identifying Redox Transition Zones in the Subsurface from a Site with Historical Contamination, *Science of the Total Environment* 2020: 762, 143105.

Yin, X., Hua, H., Dyer, J.A., Landis, R., Fennell, D., Axe, L. Assessing Reactive Iron Mineral Coatings in Redox Transition Zones with Sequential Extraction, *American Chemical Society (ACS) Earth and Space Chemistry* 2022: 6 (2), 368-379.

Yin, X., Hua, H., Dyer, J.A., Axe, L. Abiotic Degradation of Chlorinated Solvents with Reactive Iron Minerals from Redox Transition Zones, under preparation for publication.

Hua, H., Yin, X., Dyer, J.A., Landis, R., Axe, L. Characterizing Reactive Iron Mineral Coatings in Redox Transition Zones, *American Chemical Society (ACS) Earth and Space Chemistry*, 2020: 4 (12), 2337-2346.

Hua, H., Yin, X., Renno, M.I., Sale, T.C., Dyer, J.A., Landis, R., Axe, L. Impacts of Cryogenic Sampling Processes on Iron Mineral Coatings in Contaminated Sediment, *Science of the Total Environment*, 2020: 765, 142796.

Landis, R., Hua, H., Yin, X., Axe, L., Morgan, S. Biogeochemical Coring and Preservation Method for Unconsolidated Soil Samples, *Groundwater Monitoring and Remediation*, 2021: 41 (3), 72-81.

Hua, H., Yin, X., Fennell, D., Dyer, J.A., Landis, R., Morgan, S., Axe, L. Roles of Reactive Iron Mineral Coatings in Natural Attenuation in Redox Transition Zones Preserved

from A Site with Historical Contamination, *Journal of Hazardous Materials*, 2021: 420, 126600.

Yin, X., Hua, H., Ding, W., Axe, L. Degradation of 1,4-Dichlorobenzene with Natural Reactive Iron Mineral Coatings from the Sediment, American Chemical Society (ACS) Spring 2021 Conference, April 5 -30, 2021.

Yin, X., Hua, H., Burns, R.F., Fennell, D., Dyer, J.A., Landis, R., Axe, L. Determining the Speciation of Reactive Iron Mineral Coatings in Redox Transition Zones with Sequential Extraction. Global Virtual Conference, Goldschmidt 2020, June 21-26, 2020.

Hua, H., Yin, X., Renno, M.I., Sale, T.C., Dyer, J.A., Landis, R., Axe, L. Impacts of Cryogenic Sampling Processes on Iron Mineral Coatings in Contaminated Sediment. American Chemical Society (ACS) Fall 2020 Virtual Meeting and Expo, online poster, March, 2020.

Russell, M.; Yin, X.; and Axe, L. Degradation of 4-Chloroaniline by Activated Persulfate. 2019 American Institute of Chemical Engineers Mid-Atlantic Regional Conference, Penn State, PA, US, April 5-6, 2019.

Axe, L., Hua, H., Yin, X., Ding, W., Russell, M. Abiotic Degradation of 1,4-Dichlorobenzene with Reactive Iron Mineral Coatings. 2019 American Institute of Chemical Engineers Annual Meeting, Hyatt Regency, Orlando, US, November 10-15, 2019.

Yin, X., Hua, H., Axe, L. Determining Reactive Iron Mineral Contributions in Redox Transition Zones with Sequential Extraction. (Poster) 28th Goldschmidt Conference, Goldschmidt 2018, Boston, US, August 12-17.

Hua, H., Yin, X., Axe, L. Reactive Iron Mineral Coatings in Redox Transition Zones (updated version), Session: Reactions at the Mineral-Fluid Interface: Dissolution, Precipitation and Controls on Geochemical Element Cycling, Goldschmidt Conference 2018, Boston, Massachusetts, US, August 12-17, 2018.

Hua, H., Yin, X., Axe, L. Reactive Iron Mineral Coatings in Redox Transition Zones. Session: Site Investigation, 33rd Annual International Conference on Soils, Sediments, Water, and Energy, Amherst, Massachusetts, US, October 2017.

Yin, X., Hua, H., Axe, L. Identifying Redox Transition Zones in the Subsurface. (Poster) 33rd Annual International Conference on Soils, Sediments, Water, and Energy, Session: Site Investigation, Amherst, Massachusetts, US, October 16-19, 2017.

Hua, H., Yin, X., Axe, L. Characterizing Reactive Iron Mineral Coatings in Redox Transition Zones (updated version). Iron and Manganese Oxides: their Formation,

Structure, Reactivity & Applications Symposium, 254th American Chemical Society Meeting and Exposition, Washington DC, US, August 20-24, 2017.

Yin, X., Hua, H., Axe, L. Identifying Redox Transition Zones in the Subsurface. Iron and Manganese Oxides: Their Formation, Structure, Reactivity and Applications Symposium, 254th American Chemical Society Meeting and Exposition, Washington DC, US, August 20-24, 2017.

Hua, H., Yin, X., Axe, L. Characterizing Reactive Iron Mineral Coatings in Redox Transition Zones. Fate and Transport of Environmental Contaminants Symposium, 45th Middle Atlantic Regional Meeting of the American Chemical Society, Hershey, Pennsylvania, US, June 4-6, 2017.

Yin, X., Hua, H., Axe, L. Identifying Redox Transition Zones in the Subsurface. Fate and Transport of Environmental Contaminants Symposium, 45th Middle Atlantic Regional Meeting of the American Chemical Society, Hershey, PA, US, June 4-6, 2017.

To my parents, Zhinong Yin (尹知农) and Yanghong Li (李杨红),

my lover, Yaoxing Li (李耀星),

and my best friend, Yanan Yang (杨雅楠)

for their understanding, support, and love

ACKNOWLEDGMENT

There are many people I would like to thank for their contribution to my PhD dissertation, both directly and indirectly. First, I would like to thank my academic advisor, Dr. Lisa Axe, who is not only the mentor, providing valuable and countless resources and insight for my research studies, but also like an elder friend, giving me constantly support and encouragement.

I also appreciate Dr. Michel Boufadel, Dr. Wen Zhang, Dr. Lucia Rodriguez-Freire, Dr. Donna E. Fennel, and Dr. James Dyers served as my committee member from different experiential areas, offering their valuable and professional input.

I acknowledge the support of my Ph.D. research through a contact with Chemours Company and project managers Ed Lutz and Ed Seger. I also acknowledge of the contribution from Dr. Thomas C. Sale, AECOM, DuPont and Chemours for collecting the Anaerobic Core and Cyro Core at the site. Special thanks are given to Dr. James Dyer and Richard Landis, who provided valuable technical support and methodology development.

Moreover, I would like to thank the Department of Civil and Environmental Engineering for the teaching assistant funding. I would also extend my gratitude to the Chemical and Environment Science Department for their funding as well.

Last but not the least, I appreciate the kindness support and help from the fellow graduate students in my research group, Shuangyi Zhang, Han Hua and Wei Ding.

TABLE OF CONTENTS

Chapter	Page
1 INTRODUCTION	1
2 LITERATURE REVIEW	5
2.1 Iron Cycling in Redox Transition Zones.....	5
2.2 Occurrence of Reactive Iron Minerals in Natural Environment.....	8
2.3 Characterizing Redox Transition Zones in Sediments.....	11
2.4 Dichlorobenzene and Chlorinated Ethenes in the Environment	16
2.5 Abiotic Degradation Mechanisms of Chlorinated Organic Compounds.....	17
2.6 Degradation of 1,4-DCB, PCE, and TCE with Fe Minerals.....	21
2.7 Summary of Literature.....	23
3 OBJECTIVE AND HYPOTHESES	25
4 METHODOLOGY	27
4.1 Quality Assurance and Quality Control (QA/QC) Procedures.....	27
4.2 Site Description.....	28
4.3 Sample Preparation and Preservation.....	28
4.4 Sediment pH and ORP Analysis.....	31
4.5 X-Ray Fluorescence Spectrometer Analysis.....	33
4.6 TVOC Measurement.....	37
4.7 Microbial Deoxyribonucleic Acid (DNA) Sequencing Analysis.....	37
4.8 Sequential Extraction.....	38
4.9 Simulated Groundwater.....	41
4.10 Batch Studies of Chlorinated Solvents Degradation.....	44
5 CHARACTERIZING THE REDUCTION-OXIDATION TRANSITION ZONES OF A SITE WITH HISTORICAL CONTAMINATION.....	48
5.1 Screening Analyses.....	48

TABLE OF CONTENTS
(Continued)

Chapter		Page
	5.1.1 Dominant Element.....	48
	5.1.2 Sediment Redox Potential (ORP).....	51
	5.1.3 Sediment pH.....	53
	5.1.4 PID Measurements.....	55
	5.1.5 Abundant Bacteria.....	55
	5.2 Five Determined Redox Transition Zones.....	59
	5.3 Summary.....	65
6	ASSESSING REACTIVE IRON MINERAL COATINGS IN REDOX TRANSITION ZONES WITH SEQUENTIAL EXTRACTION.....	66
	6.1 Distribution of Reactive Fe Mineral Coatings in Redox Transition Zones.....	66
	6.2 Potential Fe Cycling with Abundant Bacteria.....	73
	6.3 Summary.....	76
7	KINETICS STUDIES OF 1,4-DICHLOROBENZENE, TETRACHLOROETHYLENE, AND TRICHLOROETHYLENE WITH NATURAL REACTIVE IRON MINERALS FROM REDOX TRANSITION ZONES ...	77
	7.1 COC Degradation with Sediment Samples.....	77
	7.1.1 Reductive 1,4-DCB Dechlorination	77
	7.1.2 Potential mechanism for 1,4-DCB Dechlorination	81
	7.1.3 Reductive PCE and TCE Dechlorination.....	84
	7.2 Reaction Rate Constant of Dominant Fe(II) Mineral Nano-Coatings	91
	7.3 Summary.	95

TABLE OF CONTENTS
(Continued)

Chapter	Page
8 CONCLUSIONS AND FUTURE WORK.....	96
APPENDIX A OVERVIEW OF GEOLOGICAL LOG.....	100
APPENDIX B ROTATION SPEED AND REYNOLDS NUMBER.....	104
APPENDIX C PRECIPITATION OF GYPSUM.....	106
APPENDIX D ABUNDANT OPERATIONAL TAXONOMIC UNIT IN ANOXIC CORE.....	108
APPENDIX E RATE CONSTANTS OF REDUCTIVE PCE DECHLORINATION BY FE MINERALS RELATED SYSTEMS.....	111
APPENDIX F RATE CONSTANTS OF REDUCTIVE TCE DECHLORINATION BY FE MINERALS RELATED SYSTEMS.....	112
APPENDIX G THE CALCUALTED CONCENTRATIONS OF ACETYLENE IN THE TETRACHLOROETHYLENE AND TRICHLOROETHYLENE STUDIES.....	113
APPENDIX H THE DATA OF SCREENING ANALYSES BY A SUITE OF COMPLEMENTARY TOOLS.....	116
APPENDIX I SEQUENTIAL EXTRACTION DATA OF SEDIMNET SAMPLES FROM REDOX TRANSITIION ZONES.....	129
APPENDIX J GAS CHROMATOGRAPH DATA OF 1,4-DICHLOROBENZENE, TETRACHLOROETHYLENE, TRICHLOROETHYLENE CONCENTRATIONS.....	143
REFERENCES	156

LIST OF TABLES

TABLE		Page
2.1	Chemical and Physical Properties of 1,4-dichlorobenzene, Chlorobenzene, and Benzene.....	19
2.2	Chemical and Physical Properties of Tetrachloroethylene and Trichloroethylene.....	20
4.1	Summary of Hydrogeology Beneath the Studied Site.....	30
4.2	XRF Soil Mode	34
4.3	XRF Mining Mode	35
4.4	The Methodology of the Six-Step Sequential Extraction.....	39
4.5	Ion Concentrations in Groundwater Samples.....	43
4.6	Ion Concentrations in Simulated Groundwater.....	43
4.7	Initial Concentrations of Experimental Groups.....	46
5.1	Summary Table of Screening Parameters in Five Redox Transition Zones.....	60
7.1	Observed Pseudo-First-Order Reaction Rate Constants of 1,4-DCB, PCE, and TCE with Sediment Samples Collected from Four Redox Transition Zones.....	82
7.2	Calculated Second-Order Reaction Rate Constants of 1,4-DCB, PCE, and TCE Studies.....	92

LIST OF FIGURES

FIGURE	Page
2.1	Amperometric technique conducted mediated electrochemical analyses..... 12
2.2	Overview of non-mediated (top) and mediated (bottom) electrochemical analyses..... 14
4.1	Groundwater D14-MLS (Multilevel Monitoring System) results from the area of concern along with the geological strata. 29
4.2	O ₂ concentration (ppm) in the headspace of subsample as a function of depth (m)..... 32
4.3	XRF measurements for intact (left) and non-intact (right) sediment samples..... 36
4.4	Equilibrium time in each extraction reaction for the non-milled sediment with a nonuniform particle size was determined in time studies..... 40
5.1	Dominant elements from X-ray fluorescence spectrometry (XRF) analysis as function of depth in the 18.3-meter core [left axis: elevation to the sea level (in NAVD 88 system) (m); right axis: depth below surface (m)]. Aquifer and aquitard information are shown as well..... 49
5.2	Profiles of sediment pH, sediment oxidization-reduction potential (ORP) (mV), photoionization detector (PID) reading reported as chlorobenzene (ppm), and Fe and S concentrations (mg/kg) from X-ray fluorescence spectrometry (XRF) analyses. The left axis shows elevation (m) and the lithology; the right axis gives depth below surface (m). Five redox transition zones highlighted in blue are identified based on the data..... 52
5.3	pH-E _h diagram for Fe-CO ₂ -S-H ₂ O system (25°C; 100 bars; 1 mol/kg of Fe; 10 ⁻³ mol/kg of S; 10 ⁻³ mol/kg of C; E ₀ vs. SHE) (modeled with Geochemist’s Workbench 13) ¹ . Fe and S concentrations depicted in the model are representative of sediment samples with these element concentrations..... 54
5.4	Aquifer, aquitard, and general matrix information from the Geo-log, Fe and S concentration (mg/kg) from XRF analysis, and abundant bacteria from 16S rRNA sequencing analyses..... 56

LIST OF FIGURES

FIGURE	Page	
5.5	Potential cycling between Fe/S ion, microorganism, and chlorinated contaminants in the three redox transition zones: (a) Upper Zone, (b) Zone 1, and (c) Zone 2, where Fe(II) and Fe(II)/(III) mineral coatings are expected.....	62
6.1	Fe concentrations (mg/kg) from the six-step SE (left) compared with XRD-defined Fe mineral coatings (right) in Upper Zone (3.96 to 4.57 m DBS) and Zone 1 (6.40 to 6.96 m DBS). Fe mineral coatings characterized by FESEM/EDX from these two RTZs (top) include: (A) framboidal greigite and pyrite, (B) greigite, (C) mackinawite, and (D) pyrite.....	67
6.2	Fe concentrations (mg/kg) from SE in Zone 2 (9.45 to 10.46 m DBS) and Zone 3 (14.63 to 15.24 m DBS) are presented at left, along with characterized Fe mineral coatings (XRD)* at right. Fe(III) mineral coatings* including (E) goethite (needle shape), ferrihydrite (irregular spherical shape), and lepidocrocite (scale or tablet shape) and (F) hematite were identified by FESEM/DEX (top).....	68
6.3	Distribution of Fe minerals in total extracted Fe (%) in sediment from the four redox transition zones.....	70
7.1	Reductive dechlorination of 1,4-DCB studies. (A) The concentration of 1,4-DCB (mg/L) versus time in blank, standard pyrite, and standard siderite were consistent over 97 h. Natural logarithm values of 1,4-DCB concentration versus time of Upper Zone, Zone 1 and Zone 3 were plotted in (B), (C), and (D), respectively. The natural logarithm value of 1,4-DCB and time is linear with a good fit.....	78
7.2	Concentration of 1,4-DCB, CB, and BZ in four sediment groups versus time (h).....	79
7.3	Potential reductive dehalogenation for 1,4-DCB (right) and chlorinated ethenes (left) with reactive iron mineral coatings was summarized.....	80
7.4	Reductive dechlorination of PCE in blank and control groups. No reduction of PCE was observed in the blank group as a function of time (h). The degradation of PCE in standard pyrite and siderite groups followed pseudo-first-order reaction.....	86

LIST OF FIGURES

FIGURE		Page
7.5	Reductive dechlorination of TCE in blank and control groups. No reduction of PCE was observed in the blank group as a function of time (h). The degradation of TCE in standard pyrite and siderite groups followed pseudo-first-order reaction.....	87
7.6	Natural logarithm values of PCE concentration versus time (h) of Upper Zone, Zone 1 and Zone 3 sediments were plotted. Regression results show the degradation fit pseudo-first-order reaction.....	88
7.7	Natural logarithm values of TCE concentration versus time (h) of four sediments from RTZs, were plotted and fit the pseudo-first-order model.....	90

CHAPTER 1

INTRODUCTION

The purpose of this research is to understand the contribution of reactive iron (Fe) mineral coatings in subsurface systems that have historical contamination. To pursue this goal, it is important to 1) identify the redox transition zones (RTZs) in a contaminated system where reactive Fe mineral coatings are present, 2) characterize and quantify the Fe mineral coatings in RTZ sediment samples, and 3) conduct studies on degradation kinetics for chlorinated solvents found at sites with reactive Fe mineral coatings.

Redox transition zones (RTZs) are characterized by gradients in the oxidation / reduction potential (ORP) where reduced and oxidized iron minerals, also known as reactive iron minerals, are found. In these subsurface systems, microorganisms derive energy through the reduced iron and sulfur oxidation processes (Geelhoed et al., 2009; Roden, 2012). Additionally, abundant biogeochemical processes impact carbon and nitrogen sources as well as the attenuation of contaminants. Reactive iron mineral coatings in redox transition zones act as electron donors that affect contaminant mobility, transformation, and attenuation. For example, in a study at the Hanford site, the ferruginous clay mineral smectite in a sediment sample was found to partially reduce Cr(VI) to sparingly soluble Cr(III) (Qafoku et al., 2017). At the same site, siderite (FeCO_3) was found to be responsible for Tc(VII) reduction (Peretyazhko et al., 2012). At the Rifle Site (Colorado, USA), mackinawite (FeS) was observed to serve as an electron donor for reducing dissolved U(VI) to U(IV) (e.g., UO_2) through both abiotic and biotic pathways

(Bargar et al., 2013). These studies demonstrate the importance of reactive iron mineral coatings in contaminant attenuation. However, because of the challenge of preserving the redox condition as a function of depth, there has not been a systematic study in identifying and characterizing redox transition zones in a contaminated subsurface environment. This study, a profile screening with complementary biogeochemical tools was conducted for RTZ identification.

Reactive iron mineral coatings are defined as iron minerals formed under reduced as well as oxidized conditions and are expected to be abundant in redox transition zones. Reduced iron sulfide minerals have been studied in the lab for treating chlorinated organic compounds (He et al., 2009), radioactive waste (Bargar et al., 2013; Qafoku et al., 2017), and pharmaceutical waste (Bae et al., 2013). For organic waste, abiotic dehalogenation by reactive iron sulfide minerals has been found to play an important role in, for example, chlorinated solvents (He et al., 2015; Stefaniuk et al., 2016), which including chlorinated ethenes (Han and Yan, 2016; Usman et al., 2018a), chlorinated methanes (Butler and Hayes, 2000; Czinnerová et al., 2020), and chlorinated alkanes (Choi et al., 2009). Although the transformation of a number of halogenated aliphatic compounds with crystalline iron minerals has been evaluated in lab-scale experiments, other metastable forms of iron sulfides found in natural systems (e.g., framboidal greigite) have not been studied. Furthermore, because of the challenge in preserving the redox condition of a sediment core, contaminated sediments have not been studied to the same extent. As a result, a study is needed for characterizing reactive Fe minerals in the RTZs as well as its contribution to chlorinated contaminants degradation. Such a study requires a systematic approach where

the redox condition is preserved to ensure biogeochemical processes can be isolated and evaluated.

In this study, an 18.3-m anaerobic core was collected from an industrial site with historical contamination, where the constituents of concern (COCs) include aniline, nitrobenzene, and chlorinated solvents such as chlorobenzene. A critical part of collecting the core was preserving the redox condition during transportation and storage, which are vital concerns for oxygen sensitive sediments. This study is possibly the first to identify and investigate redox transition zones in a sediment core using complementary analyses with tools that provide insights down to a scale of nm. The complementary analyses contribute to the multiple lines of evidence for locating redox transition zones. Mineralogy, morphology, and semi-quantitative analyses of reactive Fe mineral coatings in sediment samples from RTZs were characterized with X-ray diffraction (XRD) and field emission scanning electron microscopy with energy dispersive X-ray spectroscopy (FESEM/EDX) in the previous studies (Hua et al., 2020). However, these tools are limited in quantifying ion exchangeable Fe²⁺ and amorphous Fe mineral coatings due to their poor crystallinity and relatively low concentrations (less than 3% mass) in sediments (Hua et al., 2020). Nevertheless, studies demonstrate the importance and abundance of amorphous and metastable minerals in sediments (Burton et al., 2009; Ikogou et al., 2017; Stolze et al., 2019). Therefore, this study is to isolate and quantify reactive Fe mineral phases in four (out of five) RTZs; a vertical profile of the distribution of reactive Fe mineral coatings as a function of depth is evaluated with a six-step sequential extraction (SE) process.

To help resolve contributions of the reactive Fe mineral coatings in abiotic attenuation, studies were designed to evaluate reaction kinetics for constituents of concern

(COC): 1,4-dichlorobenzene (1,4-DCB), tetrachloroethylene (PCE), and trichloroethylene (TCE). The study focused on applying well characterized sediments with Fe mineral coatings from the RTZs to address reaction rate expressions and rate constants in the degradation process for each of the select COCs. To the best of our knowledge, it is the first study to resolve the abiotic dechlorination processes of chlorinated ethene and benzene in the presence of natural Fe(II) mineral nano-coatings. This study helps support MNA with reactive Fe mineral coatings found in the subsurface and in RTZs.

This dissertation includes a literature review, Chapter 2, on studies of iron cycling in redox transition zones, studies with naturally occurring reactive iron mineral coatings, methodologies for characterizing the redox transition zone, chlorinated solvent abiotic degradation pathways, and recent studies on degradation of chlorinated ethenes and benzene by reactive iron minerals. In Chapter 3, the objectives and hypotheses for this study are presented and are followed by Chapter 4 Methodology. The results are discussed in Chapters 5, 6, and 7. The concluding chapter summarizes the findings and reviews future work.

CHAPTER 2

LITERATURE REVIEW

In this literature review, studies conducted on iron speciation through biogeochemical cycling in redox transition zones are presented. The occurrences of reactive iron mineral coatings in natural environment are reviewed and includes iron minerals such as pyrite (FeS_2), mackinawite (FeS), greigite (Fe_3S_4), and siderite (FeCO_3). In addition, recent studies on methodologies to characterize the redox transition zones will be reported. The mechanism of chlorination solvents degradation through abiotic pathway are reviewed based on previous studies. The recent studies of chlorinated benzene and ethenes will be summarized in the last section.

2.1 Iron Cycling in Redox Transition Zones

Iron is the fourth most abundant element in the Earth's crust. As a result, the importance of iron in biochemistry cycling cannot be overemphasized (Bishop et al., 2020; Huang et al., 2021; Kenneke and Weber, 2003). In wetlands, riverbed sediments, and groundwater, iron and sulfur minerals play a role in trace metal transformation and organic solvent degradation (Burton et al., 2011; Rasigraf et al., 2020). Therefore, the dissolution and precipitation of reactive iron mineral coatings in the redox transition zone influence the mobility of contaminants. Amorphous iron oxyhydroxide and sulfide minerals that form initially in the precipitation process are generally more reactive than crystalline forms; reactive minerals can build up over time under reduced redox conditions (Du Laing et al., 2009). These amorphous, reactive iron mineral coatings found in redox transition zones are

important in abiotic contaminant attenuation. At the same time, biotic contributions cannot be neglected in iron cycling, where microbial communities depend on iron oxidation and reduction cycling at various spatial and temporal scales in nature.

Iron redox cycling takes place across a wide range of subsurface and near-surface environments, potentially encompassing spatial scales from molecular (nm) to pore (μm to m) size. In redox transition zones (or the oxic-anoxic interface) input of an oxidizing agent, such as oxygen, drives Fe(II) oxidation to Fe(III). Because Fe(III) is sparingly soluble under ambient groundwater conditions, iron (III) (oxyhydr)oxides precipitate (e.g., goethite ($\alpha\text{-FeOOH}$), hematite (Fe_2O_3), ferrihydrite ($\text{Fe}_2\text{O}_3 \cdot 0.5(\text{H}_2\text{O})$), and lepidocrocite (FeOOH)) in aerobic environments (Cornell and Schwertmann, 2003; Lindsay, 1988). Fe(III) oxide minerals have significant surface area, surface charge density, and microporosity, therefore, they play an important role as sorbents for organic and heavy metal contaminants (Trivedi and Axe, 2000).

Reduction of Fe(III) minerals to Fe(II) occurs through either abiotic or biotic pathways resulting in dissolution, precipitation, and/or adsorption. Compared to crystalline Fe(III) (oxyhydr)oxides such as goethite ($\alpha\text{-FeOOH}$) and hematite (Fe_2O_3), poorly crystalline ferrihydrite has been observed to reduce more quickly (Brennan and Lindsay, 1998) under higher redox potentials (Du Laing et al., 2009). For example, in glucose-enriched sediment, reduction rates of amorphous ferrihydrite is fifty-fold greater than crystalline hematite (Lovley and Phillips, 1986). The reason for this phenomenon is that freshly precipitated mineral coatings have larger ($>200 \text{ m}^2/\text{g}$) surface area and a smaller grain size distribution with highly irregular morphology (Ford et al., 1997; Stumm and Sulzberger, 1992). Iron-reducing bacteria play a significant role in driving Fe (III)

(oxyhydr)oxides to a reduced form. Direct microbial reduction coupled to oxidation of organic carbon and H₂ generation is recognized as the dominant mechanism for Fe(III) mineral reduction in anaerobic soil or sediment without sulfidogenic bacteria (Lovley et al., 2004; Lovley and Phillips, 1986). This process contributes to oxidation of both natural organic matter and organic contaminants in sedimentary environments and affects the mobility and behavior of trace metals and radioactive contaminants (Lovley and Anderson, 2000). Moreover, the Fe(II) minerals act as a strong reductant for Fe(III) (oxyhydr)oxides and form secondary minerals such as goethite (α -FeOOH), siderite (FeCO₃), magnetite (Fe₃O₄) and green rust (Borch et al. 2010). Oxidation of reduced sulfur (both biotic and abiotic) was found in sulfur-rich sediment driving Fe(III) to Fe(II) (Thamdrup, 2000). The function of bacterial catalysis is also important in Fe(III) reduction and can be coupled to oxidation of both organic carbon and reduced S in acidic sediments (Johnson et al., 1993; Küsel et al., 2000; Küsel et al., 1999). When Fe(II) is in contact with oxygen, Fe(III) precipitates into an oxyhydroxide (Taillefert et al., 2000). It is worth noting that, due to the larger surface area, amorphous fine-grained, iron sulfides and framboidal pyrite oxidize more rapidly than crystalline forms (Merinero et al., 2009).

In redox transition zones, reactive iron mineral coatings are vital to ecosystems in participating as electron donors or accepters in microbial processes. However, to a large extent this cycling has been conducted in the laboratory on synthesized minerals. To have better understanding of complex reactive iron mineral coatings found in the subsurface, studies on the occurrence of reactive iron mineral coatings in the environment are discussed in the next section.

2.2 Occurrence of Reactive Iron Minerals in Natural Environment

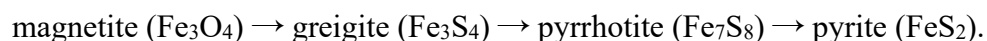
Iron is the fourth most abundant element (6.3%) in the earth's crust that can be present in a number of oxidation states; as a result, varieties of reactive iron mineral coatings are observed in the environment as a function of the biogeochemical conditions. The occurrences of Fe sulfide, Fe(II) carbonate, Fe(II)/(III) and Fe(III) minerals are discussed in the following.

Iron sulfide minerals are strong reducing agents, providing electrons in contaminant degradation (Butler and Hayes, 1999b). Pyrite (FeS_2) and mackinawite (FeS) are two iron sulfide minerals commonly observed in reduced environments ((Rickard and Morse, 2005). As the most thermodynamically stable iron sulfide mineral in the reduced environments, pyrite has been found, for example, in wetland sediments (Burton et al., 2011), in bay and estuary sediments (Buzas-Stephens et al., 2018), in sediment from acid mine drainage systems (Đorđievski et al., 2018), and in subsurface sediment (Atekwana and Abdel Aal, 2015). Furthermore, pyrite has been observed with distinct morphological characteristics including aggregates framboids, and single framboids with nanometer grains (Chen et al., 2018). The iron monosulfide mackinawite, considered a precursor to pyrite, is observed as nanometer particles with a poorly crystalline amorphous structure resulting in a larger surface area than crystalline pyrite. Under anaerobic conditions, mackinawite has been produced with sulfate-reducing bacteria (Zhou et al., 2019) and through precipitation from FeCl_2 and Na_2S suspension in the lab (Hyun and Hayes, 2015). This metastable mineral has been observed under anoxic conditions at a radioactive waste site (Carpenter et al., 2015; Noël et al., 2017), at a site with heavy metal contamination (Jonsson et al., 2012), and at sites with chlorinated solvents (Szczepanik and Sawlowicz, 2010).

Fe(II) carbonate, siderite (FeCO_3), occurs widely in sediments under reduced conditions as well. Previous studies have observed siderite mineral coatings in sediments: at a site with radioactive contamination (Thorpe et al., 2014). Siderite has been found to form biogenically by metal reducing bacteria for example, in the Bengal Delta sediments with As contamination (Islam et al., 2004), in cenozoic sediment (Griffioen et al., 2016), and organic-rich subsurface sediment (Qafoku et al., 2014). Furthermore, siderite has been studied in abiotic dehalogenation of chlorinated organics (e.g., hexachloroethane and 4-chloronitrobenzene (Elsner et al., 2004)) and of inorganic wastes (e.g. chlorate and perchlorate (Brundrett et al., 2019)).

In aquatic and terrestrial environments, the Fe(II)/(III) minerals also play important roles in the redox transition zones. For example, recently, magnetite (Fe_3O_4) has been observed in riverbed sediment (Ergin et al., 2018; Kinnaird et al., 2017), in coal ash (Cowan et al., 2017), in acid mine sediment (Đorđiević et al., 2018; Eberle et al., 2017), and in Fe-rich soil sand sediments from an oil field with PAH contaminations (Rijal et al., 2012). In contrast to magnetite, highly reactive and metastable Fe(II)/(III) green rust ($\text{Fe(III)}_x\text{Fe(II)}_y(\text{OH})_{3x+2y-z}(\text{A}^-)_z$; $\text{A}^- = \text{Cl}^-$; $1/2 \text{SO}_4^{2-}$) has not been widely reported in sediment to the same degree as magnetite (Usman et al., 2018b). Recently, however, green rust was observed at the oxic-anoxic interface of an acid mine drainage site with uranium contamination (Johnson et al., 2014), in the active volcanic geogenic CO_2 site with CO_2 -rich soil (Rennert et al., 2012), in an iron-rich oxic-anoxic layer (Zegeye et al., 2012), and in ochreous sediment from a coal mine drainage system (Bearcock et al., 2006). Metastable green rust may be found in oxic to anoxic transition areas in the subsurface. Greigite (Fe_3S_4) is another important Fe(II)/(III) mineral, which has the same inverse spinel structure as

magnetite with stable magnetization (Opdyke and Channell, 1996). In anoxic environments, greigite has been found under sulfate-reducing conditions in mud and deep-sea sediment (McElhinny and McFadden, 1999). A pathway from magnetite to greigite to thermodynamically stable pyrite has been reported (Rogers, 2015):



As a metastable mineral, occurrence of greigite generally is accompanied by mackinawite in the subsurface, for example, in organic-rich radioactive waste sediments (Janot et al., 2016) and re-flooded wetland sediments (Burton et al., 2011).

Many different types of microorganisms accept electrons as an energy source in oxidizing Fe(II) minerals. Fe(II) minerals in the presence of iron-oxidizing bacteria (e.g., photoautotrophic *Rhodobacter ferrooxidans* strain (Kappler and Newman, 2004) and *Ferroplasma acidiphilum* (Edwards et al., 2000)) have been oxidized to Fe(III) (oxyhydr)oxides resulting in, for example, ferrihydrite ($\text{Fe}_2\text{O}_3 \cdot 0.5(\text{H}_2\text{O})$), goethite ($\alpha\text{-FeO(OH)}$), hematite (Fe_2O_3), and lepidocrocite ($\gamma\text{-FeOOH}$). These Fe (oxyhydr)oxides are part of the iron cycling; for example, they have been found in redox transition zones that include iron-rich mine tailing sediment (Khoeurn et al., 2019); microbial-mediated transformations (Xiu et al., 2019), abiotic oxidation of aqueous Fe^{2+} forming ferrihydrite (Ouyang et al., 2019). During these processes, ferrihydrite, the amorphous oxyhydroxide, has been observed to be immobilize contaminants including As (Nur et al., 2019) and Lu(III) (Finck et al., 2019).

2.3 Characterizing Redox Transition Zones in Sediments

To identify areas with highly reactive iron mineral coatings, it is necessary to probe and define zones over which gradients in the redox potential can be observed. Traditionally, at sites with contamination, the redox potential of a groundwater sample may be measured with the silver/silver chloride (Ag/AgCl) electrode (reference) and Pt electrode (working). However, preserving the sample redox condition can be challenging given the immediate equilibration of water with the atmospheric oxygen. Other methods for characterizing the redox potential in groundwater have included collecting the dissolved oxygen concentration (Cherry et al., 1979), the aqueous Fe^{2+} concentration (Grenthe et al., 1992), the concentration of the redox couple $\text{H}_2\text{S}/\text{SO}_4^{2-}$ (Stefánsson and Arnórsson, 2002), and dissolved H_2 concentration (Chapelle et al., 1996). However, as a number of studies (Gorny et al., 2018; Stefánsson et al., 2005) have demonstrated, preserving the redox condition for these measurements is challenging and results are often not reproducible. In addition, the groundwater from a monitoring well may not accurately represent processes at the mineral water interface. Therefore, evaluating the redox condition of sediments is of utmost importance. Methods to characterize redox conditions are discussed.

Sediment ORP is an important indicator in understanding biogeochemical processes. Therefore, the methodology of evaluating sediment ORP has received more attention recently. Two techniques: amperometric and potentiometric are used in the sediment ORP measurements. Amperometric techniques are conducted with three-electrode cells that include a working electrode (e.g., carbon, gold), a reference electrode (e.g., Ag/AgCl), and a counter (or auxiliary) electrode (e.g., Pt) (Figure 2.1) (Faulkner and Bard, 2002). The potentiostat records the current (I) passing between the working and

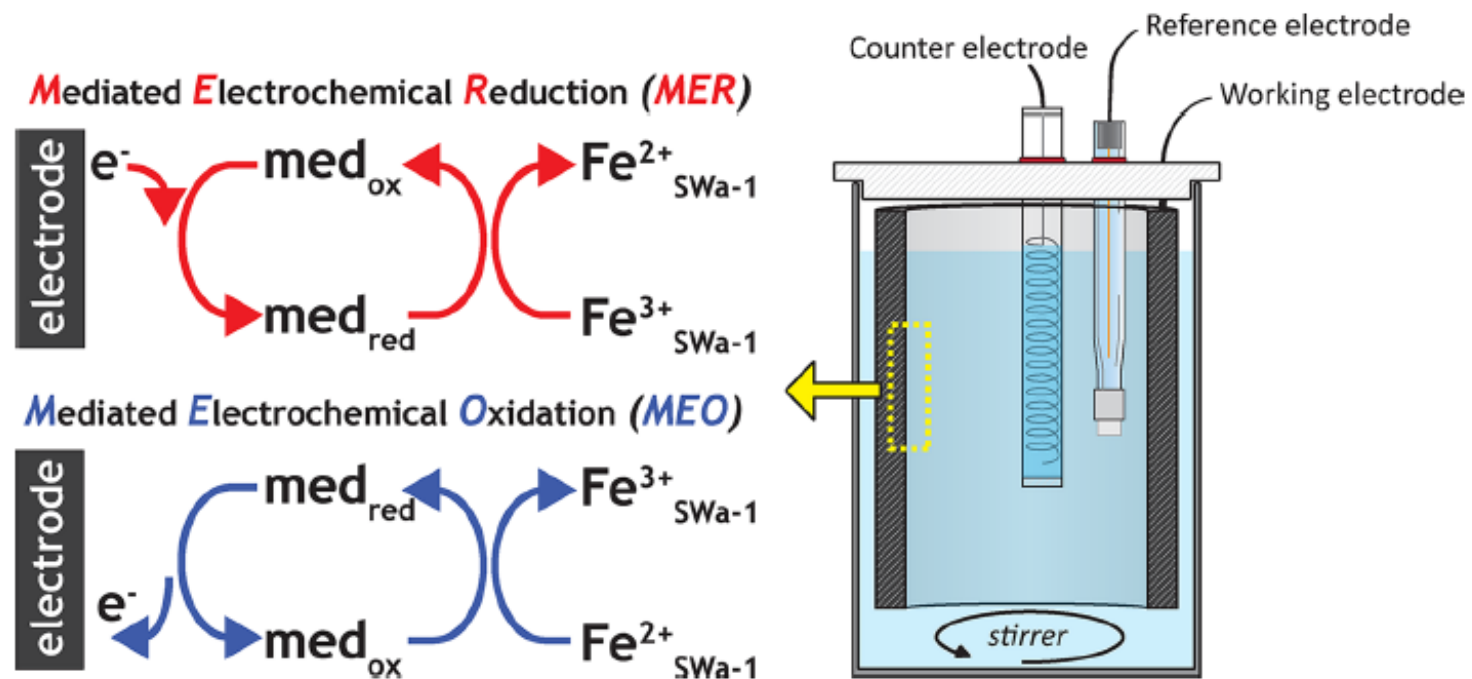


Figure 2.1. Amperometric technique conducted mediated electrochemical analyses

Source: Gorski et al. (2012)

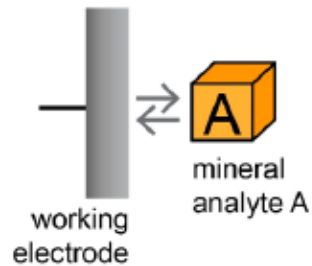
counter electrode. Based on the electrons transfers from or to the working electrode, a reductive or oxidative environment exists. Potentiometric techniques require a defined reference state. Usually, a combined electrode (e.g., a Pt working electrode combined with Ag/AgCl reference probe) is necessary. While potentiometric measurements are relatively easy to carry out, the potential is accurate only if equilibrium has been achieved between the electrode and phase that the electrode is in contact with. Generally, being at equilibrium is the most significant challenge for both techniques. For sediment samples, (slow or) non-existing redox equilibration has been reported with suspended reactive iron minerals (Shi et al., 2011; Silvester et al., 2005). On other hand, in sediment where more than one reactive mineral is present, the measured redox potential is the mixed redox potential. In sediments, electron transfer is measured from multiple phases to the working electrode at different rates and therefore the reaction(s) are not at equilibrium (Mackay and Boethling, 2000; Power and Ritchie, 1983).

To establish equilibration between the working electrode and the measured phases, two methods are commonly used including: non-mediated analysis and mediated analysis (Figure 2.2) (Aeppli et al., 2019). These two approaches can be used in both amperometric and potentiometric electrochemical techniques. Non-mediated electrochemical analyses involve taking measurements with the working electrode directly in contact with the minerals (Figure 2.2). Three different approaches may be used including (i) compact crystal electrodes, (ii) direct mineral immobilization, and (iii) composite electrodes (Sander et al., 2015). Equilibrium has been achieved with a single mineral or evenly packed conductive minerals becoming the working electrode, which is referred to compact crystal electrode. This method can be adopted for studying corrosion mechanisms (Vivier et al., 2000) and nanoparticle ORP where there is a lack of thermodynamic reference (Gorski et al., 2009; Nurmi et al., 2005). Direct mineral

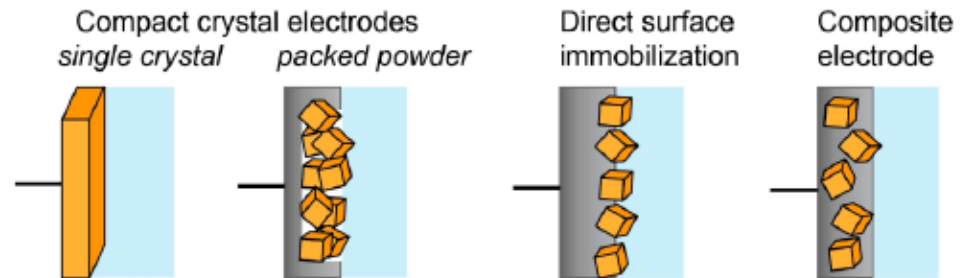
Non-mediated electrochemical analyses

direct electron transfer & redox equilibration (\rightleftharpoons)

concept:



approaches:



Mediated electrochemical analyses

mediated electron transfer & redox equilibration ($\zeta M \zeta$)

concept:



approaches:

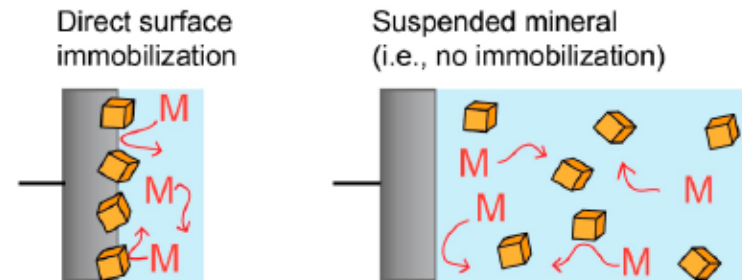


Figure 2.2 Overview of non-mediated (top) and mediated (bottom) electrochemical analyses;

Source: Sander et al.(2015)

immobilization involves impregnating the conductive mineral into a soft host electrode, such as graphite and gold. Little sample is required in this measurement where the host electrode may be present as a μm thin layer. This approach can be applied to characterize the kinetics of reductive dissolution of iron (oxyhydr)oxides (Grygar, 1995). Composite electrodes are prepared by mixing minerals with a conductive binder material (Gruner et al., 1993). This method is appropriate for minerals that lack the intrinsic high conductivity required for compact crystal electrode measurements. However, the embedded mineral may react with conductive additive (Scholz and Meyer, 1994). The three non-mediated analyses are suitable for pure minerals samples with modifications to address conductivity, however, they are not applicable for non-conductive and complex samples like Fe-rich mineral coatings.

In mediated electrochemical analyses, dissolved redox mediators are applied to rapidly equilibrate with both the working electrode and solid phase in suspension (Figure 2.2 bottom) (Sander et al., 2015). Redox potential through mediated analyses can be used for measuring redox reactions with reduced organic matter (Yu et al., 2016) and iron clay minerals (Sander et al., 2015). Studies focused on Fe-rich clay minerals (Gorski et al., 2012c) have demonstrated electron transfer with natural organic matter using mediated electrochemical reduction (MER) and oxidation (MEO). The one-electron-transfer mediating compounds facilitate electron transfer between samples to working electrode. To maintain constant E_h during the measurement, an electrochemical cell with a pH-buffer solution is required. Aeppli et al. (2019) modified the mediated electrochemical analysis by extending the time for measuring the current in a magnetite-goethite mixture; they concluded that because the current was constant for a 20-minute period, the system was at equilibrium. However, without complementary analyses to support the mechanistic processes, the system may be

transient with a slow process not observed in 20 minutes. Nevertheless, this method is useful for measuring the redox potential of a well-defined system with a single mineral surface. However, at this time, this approach is not suitable for natural heterogeneous sediment samples with complex geochemistry.

Yu and Rinklebe (2013) reported the ORP of soil-water suspension (with a sediment to water ratio 1:4) with potentiometric analysis (e.g., Pt and Ag/AgCl combination probe), this method may not be applicable for measuring an accurate ORP from sediment due to the complex matrix of the sediment-water suspension and the likely non-equilibrium condition. However, the ORP measurements and gradients observed from studying a sediment profile can provide critical evidence for redox transition zones. In addition, with measurements of Fe and S concentrations in sediment, their gradients coupled with the ORP gradients provide substantive information that can be used to isolate zones of interest in the subsurface. Furthermore, with newer molecular techniques such as amplify genus level bacteria with 16S rRNA gene sequencing (Burns, 2016), the abundant bacteria can provide further evidence of the redox conditions and transition zones.

2.4 Dichlorobenzenes and Chlorinated Ethenes in the Environment

Contamination of subsurface systems with chlorinated solvents (such as 1,4-dichlorobenzenes (1,4-DCB), tetrachloroethylene (PCE), and trichloroethylene (TCE)) is a pressing problem due to their past usage, mobility in the environment, and legacy at sites worldwide (Jordan et al., 2021; U.S.EPA, 1980; U.S.EPA, 2020). The U.S. produced approximately 2 billion pounds of chlorinated solvents each year during the period of 1940-1980 (Moran et al., 2007). According to the U.S. Environmental Protection Agency (U.S.EPA., 2021) Toxic Release Inventory dataset, from 2018 to

2020, total releases of 1,4-DCB, PCE, and TCE were approximately 0.05 million kg, 1.2 million kg, and 2.0 million kg, respectively. Because of their low solubility, relatively slow attenuation rates (Pankow and Cherry, 1996), and past disposal practices, releases into the subsurface and groundwater have been problematic.

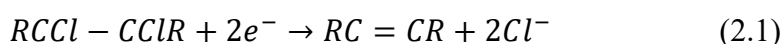
Aromatic compounds dichlorobenzenes (DCBs) have three isomeric forms: 1,2-dichlorobenzene (1,2-DCB), 1,3-dichlorobenzene (1,3-DCB), and 1,4-DCB. 1,4-DCB, the most commercially important isomer, is a volatile colorless to white crystalline material (PubChem Database, 2019). It is used as a fumigant for the control of moths, mildews, and molds and has been used as an air deodorant for restrooms and refuse containers (U.S. EPA, 1980). An important source of 1,4-DCB in the environment is its release from air deodorants and moth repellants into the atmosphere. Some 1,4-DCB entered in the soil and water from hazardous waste site (U.S.EPA., 2021). Physical and chemical properties of 1,4-dichlorobenzene impact its activity in environment (Table 2.1). Chlorinated ethenes, such as PCE and TCE, are widely used for dry-cleaning fabrics and metal degreasing operations. Because of their usage in industry, PCE and TCE have been detected in ambient air and drinking water supplies from contaminated groundwater source (U.S.EPA, 2012). A long term exposure to these two compounds will damage kidney, liver, immune system, and hematologic system ((ATSDR), 1997). The chemical and physical properties of PCE and TCE are listed in Table 2.2

2.5 Abiotic Degradation Mechanisms of Chlorinated Organic Compounds

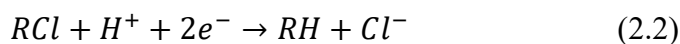
He et al. (2015) conducted a review of studies involving abiotic dehalogenation with reactive iron minerals reporting experimental conditions, products, and rate constants for the dehalogenation of chlorinated ethenes, methanes, and alkanes. They

summarized four main mechanisms for chlorinated solvents reductive dehalogenation: reductive elimination, hydrogenolysis, dehydrohalogenation, and hydrolysis.

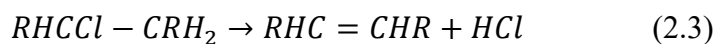
Reductive elimination is the most common abiotic pathway for chlorinated solvents dechlorination. Reductive elimination, including α -elimination and β -elimination, is a process transferring two-electron and the elimination of two chlorine atoms (De Wildeman and Verstraete, 2003). The reaction is usually observed in chlorinated ethene and alkanes transformations, and can be described in Eq. 2.1:



Hydrogenolysis is a reductive reaction where the carbon-chlorine bond is broken, and hydrogen atoms replace the chlorine atoms with simultaneous addition of two electrons to the molecule (Tobiszewski and Namieśnik, 2012). Sequential hydrogenolysis involves the sequential replacement of chloro-substituents with protons, releasing chloride (Holliger et al., 2003). The reaction is described:



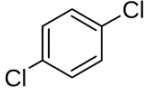
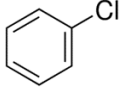
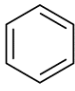
Dehydrohalogenation is a non-reductive elimination reaction involving chlorinated alkanes in which a chlorine atom is removed from a carbon atom along with removal of a hydrogen atom from a neighboring carbon atom and the resulting formation of a double bond (Goltz et al., 2005). This reaction results in the formation of less saturated compounds and increases bond order.



Hydrolysis is substitution reaction that a compound (RCl) reacts with water, and the halogen (Cl) is replaced with a hydroxyl ($-OH$) group (Goltz et al., 2005).

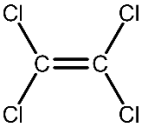
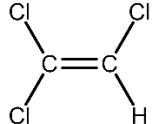


Table 2.1 Chemical and Physical Properties of 1,4-Dichlorobenzene, Chlorobenzene, and Benzene

Parameters	1,4-Dichlorobenzene (1,4-DCB)	Chlorobenzene (CB)	Benzene (BZ)
Molecular Formula	C ₆ H ₄ Cl ₂	C ₆ H ₅ Cl	C ₆ H ₆
Structure			
Molecular Weight (g/mol)	147.0	112.56	78.1
Boiling Point	174.0 °C	131.7 °C	80.0 °C
Melting Point	52.09 °C	-45.20 °C	5.42 °C
Solubility (25 °C; in water; mg/L)	81.3	499	1.79 × 10 ³
Density (g/cm ³)	1.2475	1.11	0.891
Vapor Pressure (25 °C; mmHg)	1.74	11.8	94.8
Octanol/Water Partition Coefficient (log K _{ow})	3.44	2.84	2.13
Octanol/Air Partition Coefficient (log K _{oa})	4.46	3.31	2.78
Heat of Vaporization (25 °C; kJ/mol)	49.0	40.97	33.83
Henry's Law Constant (20 °C; atm·m ³ /mol)	2.41e-3	3.11e-3	5.55e-3

Source: PubChem database (access in January 2022)

Table 2.2 Chemical and Physical Properties of Tetrachloroethylene and Trichloroethylene

Parameters	Tetrachloroethylene (PCE)	Trichloroethylene (TCE)
Molecular Formula	C ₂ Cl ₄	C ₂ HCl ₃
Structure		
Molecular Weight (g/mol)	165.8	131.38
Boiling Point	121.3 °C	87.0 °C
Melting Point	-22.3 °C	-83.5 °C
Solubility (25 °C; in water; mg/L)	206	1,280
Density (g/cm ³)	1.62	1.44
Vapor Pressure (25 °C; mmHg)	18.5	69.0
Octanol/Water Partition Coefficient (log K _{ow})	3.40	2.99
Octanol/Air Partition Coefficient (log K _{oa})	3.48	2.51
Heat of Vaporization (25 °C; kJ/mol)	39.72	34.54
Henry's Law Constant (20 °C; atm·m ³ /mol)	1.77e-2	9.85e-3

Source: PubChem database (access in January 2022)

2.6 Degradation of 1,4-DCB, PCE, and TCE with Fe Minerals

The chlorinated benzene 1,4-DCB is chemically stable (see Table 2.1) and is the byproduct of producing long-chain aromatic compounds, such as alpha-hexachlorobenzene (γ -HCH). While there have not been many studies focused on abiotic dehalogenation and degradation, Liu et al. (2003) reported 1,4-DCB was a dominant byproduct of γ -HCH transformation via reductive elimination and dehydrochlorination by mackinawite (FeS). Reduction of γ -HCH was also observed in a bimetallic system where Fe was catalyzed by less active metal such as Ag (Xu and Zhang, 2000), Cu (Zheng et al., 2009), and Pb (Nie et al., 2013). However, products from further reduction of 1,4-DCB in these systems have not been reported. Abiotic degradation of 1,4-DCB has been reported with hydroxyl radicals, activated persulfate (Garcia-Cervilla et al., 2022; Huang et al., 2005), and ozone (Real et al., 2007). Reductive biodegradation of 1,4-DCB has been studied to a greater extent under anaerobic conditions (Alfán-Guzmán et al., 2017; Fung et al., 2009; Kurt and Spain, 2013; Lawrence, 2006; Qiao et al., 2018). For example, degradation of 1,4-DCB was observed within 11 days by microcosms in the sediment collected from a contaminated industrial site (Fung et al., 2009). In other studies (Liang et al., 2011; Nelson et al., 2014; Qiao et al., 2018), *Dehalobacter* has been found to degrade 1,4-DCB; byproducts included chlorobenzene (CB) and benzene (BZ) via the hydrogenolysis pathway. Although many studies focused on 1,4-DCB biodegradation, reductive dechlorination of 1,4-DCB has not received the same attention. With a stable aromatic ring, degradation of 1,4-DCB is challenging through reductive abiotic pathways.

In field studies (Weatherill et al., 2018), degradation of chlorinated ethenes (e.g., PCE and TCE) primarily followed biotic pathways such as halorespiration and cometabolism under anaerobic conditions. With a better understanding of iron (Fe)

minerals in natural systems, abiotic dehalogenation has been recognized in the degradation of chlorinated ethenes in monitored natural attenuation (MNA) (He et al., 2009; He et al., 2015; Whiting et al., 2014). Most studies on PCE and TCE degradation have been reported based on laboratory experiments with synthesized zero-valent iron (ZVI) nanoparticles (Garcia et al., 2021), pyrite (FeS_2) (Butler and Hayes, 1999a), mackinawite (FeS) (Jeong et al., 2007), vivianite ($\text{Fe}^{2+}_3(\text{PO}_4)_2 \cdot 8\text{H}_2\text{O}$) (Bae and Lee, 2012), magnetite (Fe_3O_4) (Culpepper et al., 2018), and green rust ($\text{Fe}^{2+}_{4.5}\text{Mg}_{1.5}\text{Fe}^{3+}_2(\text{OH})_{18} \cdot 4(\text{H}_2\text{O})$) (Liang et al., 2009; Maithreepala and Doong, 2005). In the abiotic processes studied, reductive elimination is the dominant pathway for chlorinated ethene, with acetylene as the major byproduct (He et al., 2015). While hydrogenolysis has been reported to some extent (Jeong et al., 2007; Liang et al., 2009), it is the primary pathway for biotic transformation with byproducts 1,1-dichloroethylene (1,1-DCE), cis-1,2-dichloroethylene (cis-DCE), vinyl chloride (VC), and ethene. The byproduct VC is more toxic than PCE and TCE (McCarty, 1997), as such abiotic degradation may be a more attractive strategy. In field studies, abiotic degradation of PCE and TCE was observed with Fe(II) minerals in low permeability source zones (Berns et al., 2019), dense non-aqueous liquids (DNAPLs) (Puigserver et al., 2022), and clay soils (Entwistle et al., 2019; Schaefer et al., 2017). However, contributions of nano-size reactive Fe mineral coatings in the degradation process have not yet been reported.

Reactive Fe minerals play an important role in the mineral-water interface (Kotopoulou et al., 2022). Under sulfate- and iron-reducing conditions, abiotic reduction of chlorinated solvents driven by synthesized reactive Fe minerals has been widely reported in laboratory-scale studies (He et al., 2009). With a better understanding of mineral solubility (Table S2), reactive iron minerals such as siderite

(Bruno et al., 1992), pyrite (Rickard and Luther, 2007), and magnetite (Rickard and Luther, 2007) were applied in field studies. The target compounds have included chlorinated ethenes (e.g., PCE (Butler and Hayes, 1999a; Jeong and Hayes, 2007; Liang et al., 2007a; Nunez Garcia et al., 2020) and TCE (Audí-Miró et al., 2015; Velimirovic et al., 2013)), chlorinated methanes (e.g., carbon tetrachloride (CCl₄) (Choi and Lee, 2009; Rodríguez-Fernández et al., 2018; Zhang et al., 2021b; Zwank et al., 2005)), and chlorinated alkanes (e.g., 1,1,1-trichloroethane (Butler and Hayes, 2000; Choi et al., 2009; Gander et al., 2002)). Based on studies with pure minerals, the general trend of mineral activity for chlorinated solvent degradation was summarized by He et al. (2015) as the following: disorder mackinawite > mackinawite > ZVI > pyrite > sorbed Fe²⁺ > green rust = magnetite > biotite > vermiculite. On the other hand, the reactivity of iron minerals in natural systems has been more difficult to resolve. Multiple studies demonstrated Fe(II)-bearing clay (e.g., illite, chlorite, and riebeckite) and pyrite present in rock matrices participated in PCE and TCE dechlorination (Entwistle et al., 2019; Schaefer et al., 2018b; Schaefer et al., 2017; Yu et al., 2018). However, several minerals in the matrix contribute to contaminant attenuation. With rates that are environmentally relevant, further work is needed in resolving degradation kinetics from Fe(II) mineral contributions (Berns et al., 2019; Schaefer et al., 2013).

2.7 Summary of Literature

In this chapter, discussion of iron cycling and transformation of reactive iron minerals in the environment were reported. The literature demonstrates the importance of reactive iron mineral coatings in abiotic and biotic processes. These processes are most significant redox transition zones. Multiple tools can be applied to better define these zones in the subsurface. Additionally, dichlorobenzenes and chlorinated ethenes (PCE

and TCE) have been released in the environment becoming serious problems. The abiotic degradation mechanism of these compounds with reactive Fe minerals has been summarized in this chapter, indicating reactive Fe minerals in contaminated systems play an important role in contaminant attenuation. In the Chapter 3, objectives and hypotheses are presented.

CHAPTER 3

RESEARCH OBJECTIVES AND HYPOTHESES

The presence of reactive iron minerals has led to a number of studies to understand their formation, transformation, and geochemical cycling in redox transition zones. Studies have demonstrated iron speciation is a function of the redox potential and gradient, pH, and microbial activity in the system. However, these studies have been conducted for the most part in the lab and therefore there have not been studies conducted that examined the scale of these redox transition zones and the iron mineral coatings formed while preserving the redox condition. Therefore, the objectives of this study are to:

Determine the biogeochemical conditions (e.g., sediment pH, sediment ORP, TVOC, and elemental concentration) in 18.3-m anoxic core sediment as a function of depth with the redox condition preserved.

Identify the location of redox transition zones with complementary analyses probing samples from the meter down to nano scale.

Develop the understanding of Fe and S cycling in the redox transition zones based on the iron species correlating with microbial data.

Evaluate reaction kinetics for the abiotic dehalogenation of chlorinated solvents with reactive iron mineral coatings.

The following hypotheses will be tested:

Reactive iron mineral coatings play a significant role in abiotic reactions in the subsurface oxic-anoxic environment.

Based on Fe and S concentrations as a function of depth, gradients observed correlate with redox potential gradients in the subsurface.

Transition zones with reactive mineral coatings can be identified based on sediment pH, redox potential, composition, constituents of concern (COC), and abundance of bacteria.

The speciation of reactive iron minerals forming on bulk surfaces can be characterized using tools such as sequential extraction. These surface coatings control the desired (a)biotic reactions and are a signature of the biogeochemical processes that are active.

Sediments with reactive iron mineral coatings contribute to the degradation of 1,4-dichlorobenzene (1,4-DCB), tetrachloroethylene (PCE) and trichloroethylene (TCE) in

the redox transition zones; the reaction rate expression is expected to fit a pseudo-first order reaction given the elevated concentration of Fe mineral coatings in the subsurface.

CHAPTER 4

METHODOLOGY

In this section, methods used in screening sediment samples from the 18.3-m core are reviewed for investigating metal concentration and distribution, sediment ORP, sediment pH, and TVOCs in the headspace. In addition, to assess the speciation and forms of the Fe mineral coatings, sequential extraction will be applied, and the methodology is reviewed in this chapter. Moreover, a bench study protocol will be conducted to evaluate the dechlorination kinetics of 1,4-DCB, PCE, and TCE with reactive iron mineral coatings. Laboratory quality assurance and quality control (QA/QC) are based on the Standard Methods for the Examination of Water and Wastewater (Rice et al., 2017) including cleaning process, duplicate iron concentration measurement by flame atomic absorption spectroscopy (FAA). All reagents are prepared with chemicals of ACS grade and in O₂ free deionized (DI) water (30 minutes N₂ purged until loaded in the glovebox).

4.1 Quality Assurance and Quality Control (QA/QC) Procedures

All non-disposable sample containers, test chambers, and other equipment that were in contact with sediment are washed initially with a Micro 90 detergent and rinsed with deionized water (USEPA, 2000). Glassware was then soaked in a 10% HNO₃ solution for 2 days and 1 day for high-density polyethylene (HDPE) (Nalgene[®]) containers (John, 2003). After the acid wash, the glassware and HDPE containers were rinsed in DI water and stored in a particle-free environment (i.e., sealed in plastic bags).

4.2 Site Description

The studied site is underlain by approximately 152.4 m of unconsolidated Coastal Plain sediment (Table 4.1) deposited during the Holocene epoch (B-Aquifer and B-C Clay), Pleistocene epoch (Aquifers C and D), and Cretaceous period (Aquitard D-E Clay) (URS, 2013). The dominant bulk minerals in this system include quartz (SiO_2), kaolinite ($\text{Al}_2\text{Si}_2\text{O}_5(\text{OH})_4$), and illite ($(\text{K},\text{H}_3\text{O})\text{Al}_2\text{Si}_3\text{AlO}_{10}(\text{OH})_2$). The upper 3.35 m depth below the surface (DBS) is comprised of fill material, which is not part of this study. From 3.35 m to 5.49 m (DBS), the unconfined B-Aquifer is recharged by groundwater. The C-Aquifer is located at a DBS of 6.86 m to 10.45 m with significant hydraulic communication with the B Aquifer. The D-Aquifer is hydraulically connected to the C-aquifer and is located at 10.45 m to 14.63 m (DBS). A pump and treat system is centrally located on the site and controls groundwater flow.

4.3 Sample Preparation and Preservation

An 18.3 m by 10.16 cm diameter outfitted anoxic core was collected with a hybrid Vibracore core barrel and Rotosonic drilling technique from an industrial site with historical contamination. Constituents of concern (COCs) present in the groundwater include aniline, nitrobenzene, and chlorinated solvents such as chlorobenzene (COCs in the groundwater are shown in Figure 4.1). Sixty-one cm long core samples were collected with stainless steel liners as they are chemically resistant and a barrier to oxygen; each was capped with aluminum foil covered stainless-steel disks and Fernco cap on site (Landis et al., 2021). To preserve the *in situ* redox conditions of the sediment, each core was loaded in a PVC tube that was purged with analytical grade argon (0.10 – 0.14 bar outlet pressure ($2.84 \times 10^{-4} \text{ m}^3/\text{s}$)), sealed, delivered (in approximately 2 hours) to New Jersey Institute of Technology (NJIT), and stored at 4 °C (Burt and Staff, 2014).

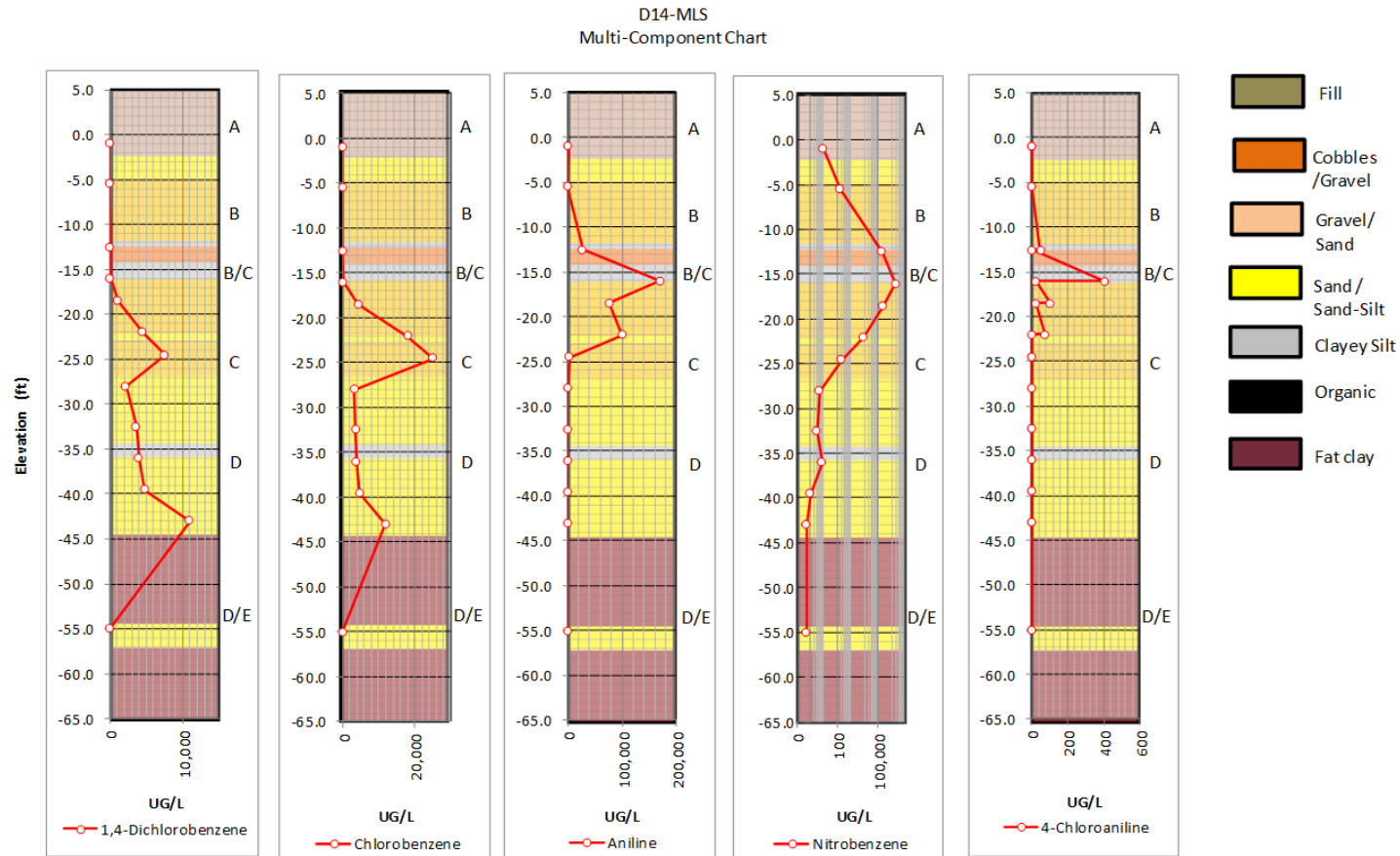


Figure 4.1. Groundwater D14-MLS (Multilevel Monitoring System) results from the area of concern along with the geological strata. The five dominant COCs are 1,4-dichlorobenzene, chlorobenzene, aniline, nitrobenzene, and 4-chloroaniline. This figure is adapted from the Chemours Chambers Works Site SAB server. The contractor AECOM collected samples and compiled the data (AECOM, 2016)

Table 4.1. Summary of Hydrogeology Beneath the Studied Site

Aquifer/Aquitard	Geologic Age	Depth Below the Surface (m)	Geologic Description	Hydrogeologic Characteristic
B	Holocene	3.35 – 5.49	Interbedded clays, silts and sands	Aquifer: B-Aquifer is less permeable than C and D Aquifers. Unconfined
B-C	Holocene	5.49 – 6.89	Gray to black silt or clay	Aquitard: Thin to absent or sandy in the eastern portion of the site and in the vicinity of the basins.
C	Pleistocene	6.86 – 10.45	Coarse sand with some cobbles	Aquifer: C-Aquifer is significantly more permeable than B-Aquifer. Additionally, C-Aquifer is similar to D Aquifer. Hydraulically connected to the B-Aquifer.
D	Pleistocene	10.45 – 14.63	Poorly sorted coarse sand with some cobbles	Aquifer: Deposits filled paleovalley that was cut into Cretaceous age sediments. Hydraulically connected to the C-Aquifer.
D-E	Cretaceous	14.63 – 20.12	Red clay or variegated (red, white, yellow and gray clay)	Aquitard: Regionally effective aquitard.

Source: DuPont. Conceptual site model: Hydrogeology and remediation of contaminated groundwater. Internal Report, 2006.

The analyses began once the core samples were delivered.

All experiments were conducted in a glovebox (Vacuum Technology) under a 99.999% N₂ environment (O₂ < 0.1 ppm). An electrically powered hydraulic jack system was designed and operated in the glovebox for extruding core samples from the stainless-steel sleeves into approximately 5.08 cm thick, 7.62 cm diameter subsamples. A total of 225 subsamples were logged photographically and included reporting (Soil and Rock, 2017) dominant geology (sand, clay, silt, and gravel), aquifer and aquitard information, water content, grain size, color, and oxygen concentration in the sediment headspace (Appendix A and Figure 4.2). Sediment from an aquifer at a DBS of 15.24 to 17.17 m was not retrieved (Appendix A). Subsamples were stored in DURAN® borosilicate wide-mouthed sample containers with 5.08×10^{-3} cm PTFE film and 6.10×10^{-2} cm aluminum foil lined caps; the containers were heat sealed in 0.127 mm Mylar bags with a 99.999% N₂ headspace to maintain the redox condition. The samples were placed in Nalgene® containers to ensure safe handling in moving samples from the refrigerator to the glovebox. All the samples were stored at 4 °C.

4.4 Sediment pH and ORP Analysis

Sediment pH and sediment ORP were measured with an Orion Star A211 Benchtop Meter (Thermo Scientific). For each 5.08 cm sample, 5 g of sediment (wet weight) was mixed in a 0.01 M CaCl₂ solution resulting in a solid to liquid ratio of 1:3 (w/v) (Burt and Staff, 2014; Sumner, 1994). This ratio with an electrolyte was found to reduce the suspension effect on pH along with minimizing the liquid junction potential and fluctuations in pH measurements. The pH measurement was conducted at room temperature ($20 \pm 2^\circ\text{C}$) with a three point (pH = 4.01, 7.00, 10.01) calibrated glass probe (8302BNUMD, Thermo Scientific). For measuring the sediment redox potential, a

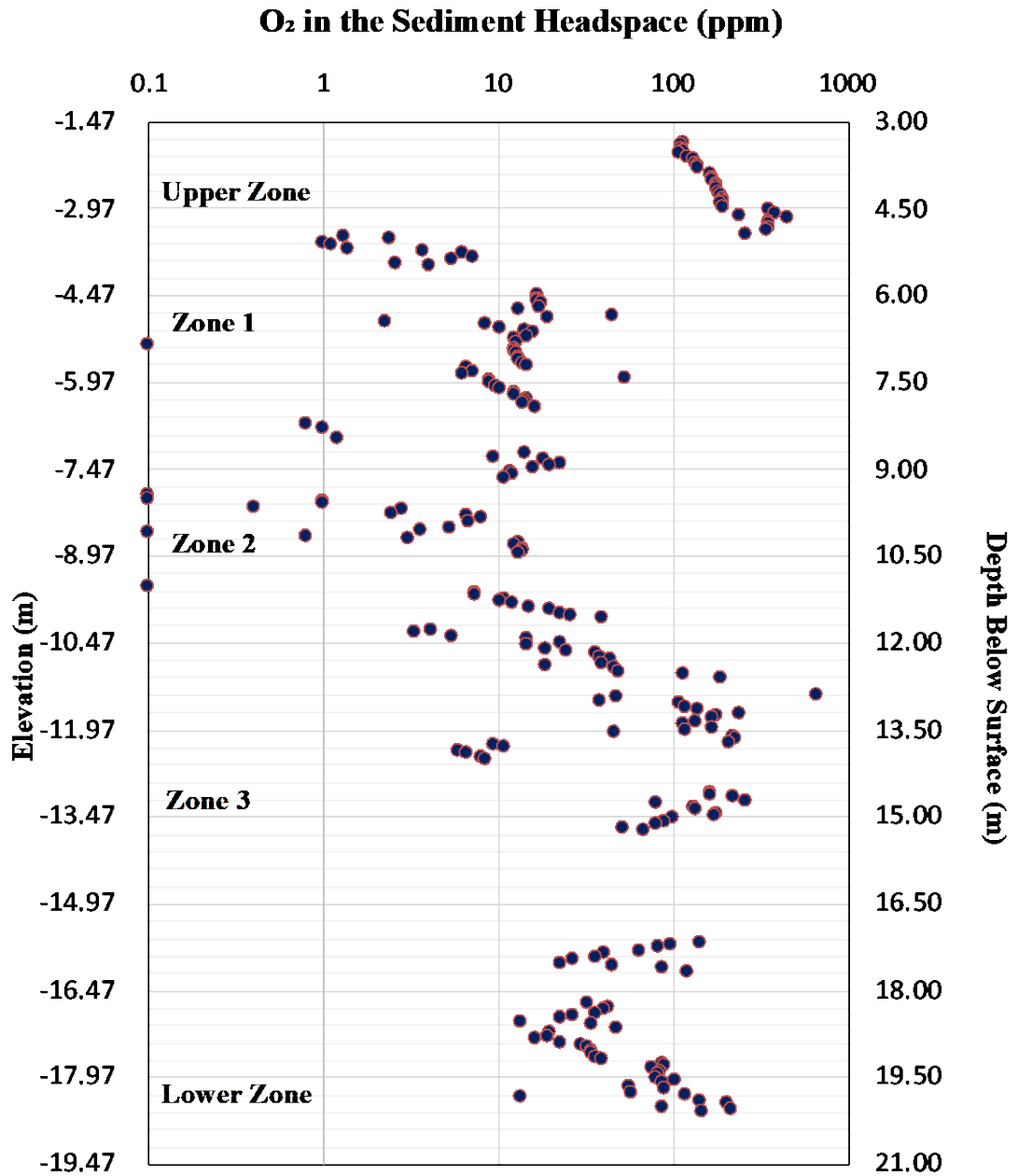


Figure 4.2 O₂ concentration (ppm) in the headspace of subsample as a function of depth (m).

sediment/DI water ratio of 1:4 (w/v) was applied (Yu and Rinklebe, 2013). The completely mixed suspension was measured using a combination (Pt redox sensor and Ag/AgCl reference system) ORP probe (9179BN, Thermo Scientific); this approach has been reported to result in more accurate measurements compared to the bulk soil measurement with spear-probe (Herbel et al., 2007). The measurement stabilized at an equilibration period of 15 mins. The ORP is reported using an Ag/AgCl reference electrode and was not converted.

4.5 X-Ray Fluorescence Spectrometer Analysis

X-Ray fluorescence (XRF) is an effective and non-destructive method for conducting sediment elemental analysis. Elemental (atomic number > 12) concentrations (mg/kg) in the sediment were measured using a Niton™ XL3t GOLDD+ XRF Analyzer (Thermo Scientific) in both soil mode (metal concentration < 1% w/w) and mining mode (metal concentration >1% w/w) (Tables 4.2 and 4.3) following EPA 6200 Method (U.S.EPA., 2007). The XRF used in this study is equipped with a built-in calibration program. Each 5.08 cm subsample was classified as either intact or non-intact. Fifteen sampling locations were measured in each cylindrically shaped, intact (*in situ*) sample where clay and silt were dominant (Figure 4.3). For non-intact samples, five subsamples were collected into 12 ml disposable XRF containers and covered with a transparent membrane. Each non-intact subsample was measured in triplicate (Figure 4.3). The standard error in Fe and S concentrations is ± 228 mg/kg and ± 212 mg/kg, respectively.

Table 4.2 XRF soil mode (Thermo Scientific Niton XL3t GOLDD+ Series Manual).

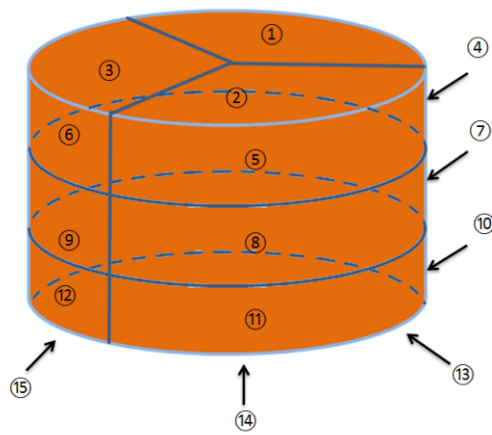
Soil Mode Limits of Detection in ppm (mg/kg)				
Element	Time	60s per filter		
	Matrix	SiO ₂	SiO ₂ +Fe+Ca	SRM
Mo		3	3	3
Zr		3	4	7
Sr		3	3	7
U		5	4	7
Rb		3	3	5
Th		4	4	5
Pb		5	8	8
Se		3	4	4
As		4	7	7
Hg		6	9	9
Au		7	9	9
Zn		7	10	12
W		20	30	30
Cu		10	13	15
Ni		25	30	30
Co		20	90	90
Fe		25	N/A	N/A
Mn		35	50	65
Cr		10	22	30
V		10	25	60
Ti		20	60	150
Sc		10	75	80
Ca		40	N/A	N/A
K		45	150	N/A
S		75	275	350
Ba		35	45	45
Cs		30	35	35
Te		30	35	35
Sb		15	20	20
Sn		15	20	20
Cd		10	12	12
Ag		A/S	A/S	A/S
Pd		10	12	12

A/S = Application-specific N/A= Not applicable

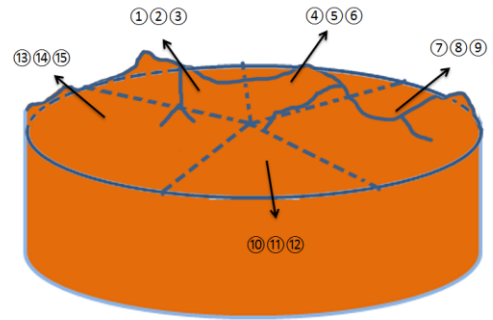
Table 4.3 XRF Mining Mode (Thermo Scientific Niton XL3t GOLDD+ Series Manual).

Mining Mode Limits of Detection in ppm (mg/kg)							
Element	Time	60s per filter w/out He					
	Matrix	SiO ₂	SiO ₂ +Fe+Ca		SRM		
Ba		35	40		45		
Sb		12	15		15		
Sn		15	18		20		
Cd		8	10		10		
Pd		5	5		5		
Ag		A/S	A/S		A/S		
Mo		3	3		3		
Nb		3	3		3		
Zr		3	3		5		
Sr		3	3		5		
Rb		3	3		3		
Bi		3	5		5		
As		3	5		5		
Se		3	3		3		
Au		16	20		20		
Pb		5	10		10		
W		40	60		60		
Zn		8	15		15		
Cu		12	15		15		
Ni		25	30		39		
Co		20	100		100		
Fe		35	N/A		N/A		
Mn		60	65		85		
Cr		20	30		35		
V		10	20		35		
Ti		10	20		60		
Ca		50	N/A		N/A		
K		40	N/A		N/A		
Cl		60	50*	80	65*	75	65*
S		70	55*	90	75*	125	90*
P		250	200*	400	330*	300	230*
Si		N/A	N/A	N/A	N/A*	N/A	N/A*
Al		500	220*	1000	500*	2500	1000*
Mg		3500	750*	6000	1500*	6500	2000*

A/S = Application-specific N/A= Not applicable



Sample locations for XRF analysis of cylinder (Intact)



XRF scan for samples non-intact

Figure 4.3 XRF measurements for intact (left) and non-intact (right) sediment samples. In this study, XRF tube excitation reached 50 keV. For each subsample (5.08 cm), 15 scans were collected. To preserve the redox condition of core samples and the heterogeneity of the sample as well, sediment was not milled outside of the glovebox. Based on the density of the material, the penetration depth for sediment sample is from 0.3 to 1.6 cm.

4.6 TVOC Measurement

To obtain a relative understanding of total volatile organic compounds (TVOC) (volatiles and semi-volatiles) present, triplicate photoionization detector (PID) measurements were collected of each sample's headspace (Jian et al., 2014). Chlorobenzene is one of the dominant COCs in the area of concern based on multilevel monitoring system (MLS) groundwater analyses (Figure 4.1). As a result, the PID (MiniRAE 3000 with 11.7 eV lamp, Honeywell) was calibrated with isobutylene and reported as chlorobenzene (RAE, 2010).

4.7 Microbial Deoxyribonucleic Acid (DNA) Sequencing Analysis

Sterile sampling tools and vials were used for collecting and storing samples for DNA extraction. Each 5.08 cm subsample was examined macroscopically and 0.2 g of material was retrieved (Iker et al., 2013) from each subsample so that visibly differing material within the subsample was represented. This material was then mixed and processed for DNA isolation using a PowerSoil™ (Qiagen) kit with five one-minute agitation cycles using a MiniBead beater 96 (Biospec Products). DNA from each 5.08 cm subsample was used for microbial community analysis by amplification of the 16S rRNA gene V4 region using primers described previously (Raju et al., 2018), sequencing DNA from each subsample to a read depth of greater than 50,000 reads. Sequences were then error corrected, and subject to de novo operational taxonomic unit (OTU) clustering, relative abundance of each OTU was determined in each sample, and genus level taxonomic assignment of the OTUs generated using the Mothur analysis pipeline (Kozich et al., 2013).

4.8 Sequential Extraction

A six-step SE (Table 4.4) was conducted where two samples from each subsample were collected and were run in duplicate. The total Fe concentration of each sample was measured with XRF (Niton™ XL3t GOLDD+, Thermo Scientific) in triplicate using soil mode (metal concentration < 1% w/w) and mining mode (metal concentration > 1% w/w) (U.S.EPA., 2007) in a glovebox. To preserve the redox condition and mineralogy of sediment samples, sediment could not be milled outside of the glovebox and the native particle size of the sediment was used. As a result, each extraction was evaluated on sediment samples representative of the core (i.e., silt, sand, and clay) as a function of time to ensure equilibrium was attained. A total of 1 g sediment was placed in 40 mL centrifuge tube with 10 mL extractant in the extraction. Samples were continuously shaken in the glovebox at 500 rpm during extraction. After each reaction, residual sediment and supernatant were separated (in air-tight, sealed centrifuge tubes) outside of glovebox at 13,000 rpm for 30 mins (with N₂ headspace). To reduce interference between each step, residual sediment was rinsed in the glovebox with DI water three times (except for the samples from Zone 1). The concentration of Fe in each extract was evaluated with flame atomic absorption (FAA) or inductively coupled plasma-mass spectrometry (ICP-MS) (U.S. EPA method 7000B and 6020B). With Octopole Reaction System installed in Agilent 7900 ICP-MS, plasma-based interference can be reduced for Fe measurements (Yamada et al., 2002).

SE analyses are affected by particle size, pH, and mineral structure (Rodgers et al., 2015), therefore, resolving the period of extraction for the sediment core collected is necessary before applying SE. In a time study of each extraction step, the concentration of extracted Fe increased with time in all but Step 5 of the extractions (Figure 4.4). Based on these results, the maximum Fe recovery rate increased by as

Table 4.4 The Methodology of the Six-Step Sequential Extraction

Extraction step	Targeted species	Extractant	Applied time (h) ^a	References
1	Ion exchangeable Fe ²⁺	1 M calcium chloride (CaCl ₂), pH 7	3	(Heron et al., 1994; Tessier et al., 1979)
2	Carbonate-associated Fe: siderite along with partial mackinawite	1 M sodium acetate (NaAc), pH 4.5	40	(Poulton and Canfield, 2005; Zhu et al., 2016)
3	Poorly crystalline Fe: mackinawite, ferrihydrite, greigite	1 M hydrochloric (HCl)	11	(Cooper and Morse, 1998; Lerner et al., 2006; Scouller et al., 2006)
4	Reducible oxides: Goethite, akaganeite, hematite	0.29 M sodium dithionite (Na ₂ S ₂ O ₄) buffered to pH 4.8 with 0.35 M acetic acid (CH ₃ COOH) and 0.2 M sodium citrate (Na ₃ C ₆ H ₅ O ₇)	7	(Poulton and Canfield, 2005)
5	Magnetite	0.2 M ammonium oxalate ((NH ₄) ₂ C ₂ O ₄) buffered to pH 3.2 with 0.17 M oxalic acid (C ₂ H ₂ O ₄)	6	(Poulton and Canfield, 2005)
6	Pyrite	Concentrated nitric acid (15.9 M HNO ₃)	4	(Claff et al., 2010)

^a The applied times for sediment in which the particle size is not uniform were determined in a reaction equilibrium time study (Figure 4.4)

Reaction Time

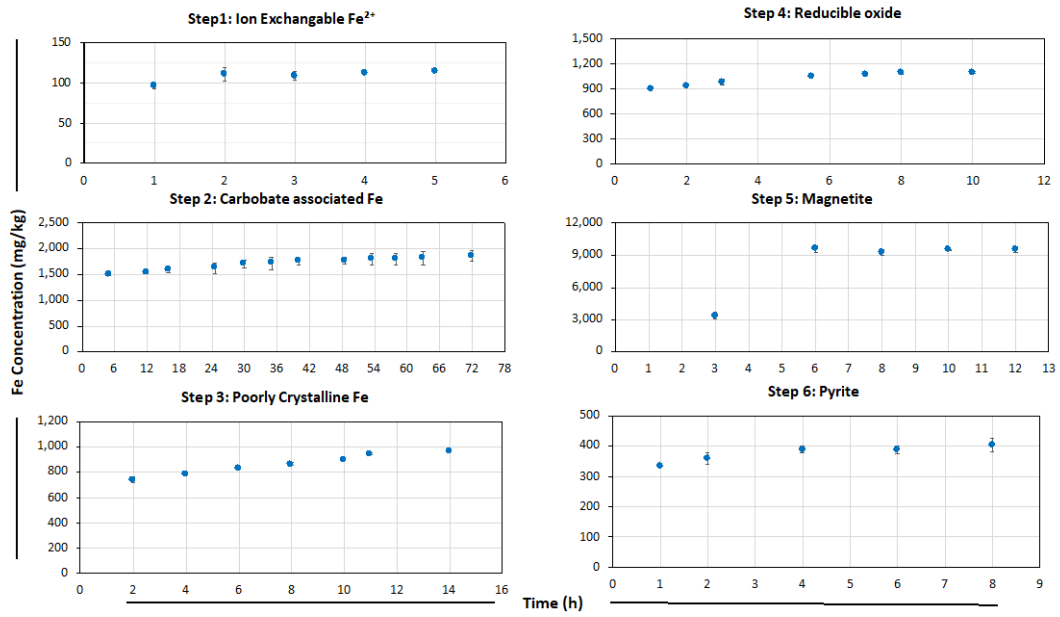


Figure 4.4 Equilibrium time in each extraction reaction for the non-milled sediment with a nonuniform particle size was determined in time studies. Two samples were collected and run through the six-step SE. The equilibrium time (h) as a function of Fe concentration (mg/kg) with double measurements are reported and compared to the theoretical time from the literature (see Table 4.4).

much as 21%, thereby effectively improving Fe extraction in the core samples. The six-step SE with modified extraction times included:

Step 1: To extract the exchangeable trace metals, which includes adsorbed Fe^{2+} in the sediment, 1 M CaCl_2 or MgCl_2 solution was added to sediment at pH 7 (Heron et al., 1994; Tessier et al., 1979) and the extraction time was extended from 1 to 3 h (14% improvement in recovery).

Step 2: Fe carbonate siderite ($\text{FeCO}_3(\text{s})$) was extracted with sodium acetate (NaCH_3COOH , referred to as NaAc) (Tessier et al., 1979). Poulton and Canfield (2005) reported NaAc at pH 4.5 can effectively target siderite; however, the extraction is not complete for highly crystalline structures. In this study, siderite was extracted by 1 M NaAc at pH 4.5 and the extraction time was extended from 24 h to 40 h (10% improvement in recovery). In this step, a fraction of mackinawite is dissolved as well (Zhu et al., 2016).

Step 3: 1 M hydrochloric acid (HCl) was used to extract > 99% poorly crystalline Fe sulfides (e.g., mackinawite (FeS)) (Cooper and Morse, 1998), 40-67% of greigite (Fe_3S_4) (Cornwell and Morse, 1987), and (92-98%) the amorphous mineral ferrihydrite ($\text{Fe}_2\text{O}_3 \cdot 0.5(\text{H}_2\text{O})$) (Claff et al., 2010) with an extension of time from 4 to 11 h (21% improvement for recovery).

Step 4: Reducible Fe (oxyhydr)oxides (i.e., goethite ($\alpha\text{-FeOOH}$), lepidocrocite ($\gamma\text{-FeOOH}$), and hematite (Fe_2O_3)) were extracted with 0.29 M sodium dithionite ($\text{Na}_2\text{S}_2\text{O}_4$) at pH 4.8 (buffered with 0.35 M acetic acid and 0.2 M sodium citrate) (Poulton and Canfield, 2005) with an extension of time from 2 to 7 h (14% improvement in recovery).

Step 5: The extraction for Fe (II/III) mineral magnetite (Fe_3O_4) was conducted for 6 h (no additional time was needed) with 0.2 M ammonium oxalate at pH 3.2 and buffered with 0.17 M oxalic acid (Phillips and Lovley, 1987; Poulton and Canfield, 2005).

Step 6: Pyrite was extracted with concentrated HNO_3 at a room temperature for 4 h instead of the 2 h reported in literature (Claff et al., 2010).

4.9 Simulated Groundwater

Analytical grade chemicals (Certified ACS) used in this study included 1,4-dichlorobenzene ($\text{C}_6\text{H}_4\text{Cl}_2$, 99%), tetrachloroethylene (PCE, >99.5%), trichloroethylene (TCE, >99%), hydrochloric acid (HCl, 37.3%), methanol (CH_4O , 99.9%), tris(hydroxymethyl)aminomethane ($\text{C}_4\text{H}_{11}\text{NO}_3$, 99.8%), sodium sulfate (Na_2SO_4 , 99.9%), sodium bicarbonate (NaHCO_3 , 100.3%), sodium chlorate (NaCl , 100.4%), magnesium chlorate (MgCl_2 , 99.8%), and calcium chlorate (CaCl_2 , 100.5%);

they were purchased from Thermo Fisher Scientific. Concentrations of dominant ions were measured in the groundwater with a Multi-Level Sampling (MLS) system adjacent to the location of the core (Table 4.5). Dominant ion contributions were used to simulate groundwater conditions: Na^+ for alkali metal ions, Ca^{2+} and Mg^{2+} for alkaline earth metal ions, and Cl^- for the halogen ions. In addition, given their presence in groundwater, other anions included SO_4^{2-} (due to its abundance) and HCO_3^- with the presence of the carbonate system. MINEQL+ (version 5.0) was used to simulate the groundwater chemistry, ionic strength, and charge balance (Schecher and McAvoy, 2001); results were compared to the original groundwater charge balance. The simulated waters for the three RTZs were used in this study (Table 4.6).

Abiotic degradation processes of PCE and TCE have been widely studied in the laboratory with synthesized Fe(II) sulfide minerals from pH 7 to 9 (Butler and Hayes, 1999a; Kim et al., 2013; Liang et al., 2007b). Given the reaction rate increased with increasing pH, PCE and TCE studies were conducted at pH 9. Although abiotic degradation of 1,4-DCB with reduced iron minerals has not been specifically studied, the degradation of γ -HCH has been, with 1,4-DCB being the primary byproduct in the process (Liu et al., 2003). Liu et al. (2003) reported the reaction rate at pH 8.3 was greater than that at pH at 6.9. Badea et al. (2021) studied dehalogenation of γ -HCH by nano-FeS from pH 2 to 11, where the reaction rate again increased with pH. As a result, pH 9 was selected in the bench-scale study for three COCs (1,4-DCB, PCE, and TCE). Tris(hydroxymethyl)-aminomethane and hydrochloric acid (Tris-HCl) buffer solution was used to maintain a constant pH.

Table 4.5 Ion Concentrations in Groundwater Samples

Upper Zone		Zone 1		Zone 3	
Species	Concentration (mol/L)	Species	Concentration (mol/L)	Species	Concentration (mol/L)
SO ₄ ²⁻	6.84× 10 ⁻⁴	SO ₄ ²⁻	1.36× 10 ⁻³	SO ₄ ²⁻	3.96× 10 ⁻³
Na ⁺	6.36× 10 ⁻³	Na ⁺	1.44× 10 ⁻²	Na ⁺	1.44× 10 ⁻²
K ⁺	2.73× 10 ⁻⁴	K ⁺	2.65× 10 ⁻⁴	K ⁺	3.00× 10 ⁻⁴
Mn ²⁺	1.63× 10 ⁻⁵	Mn ²⁺	4.96× 10 ⁻⁵	Mn ²⁺	9.74× 10 ⁻⁵
Mg ²⁺	7.96× 10 ⁻⁴	Mg ²⁺	8.40× 10 ⁻⁴	Mg ²⁺	2.47× 10 ⁻³
F ⁻	1.34× 10 ⁻⁴	Cl ⁻	5.58× 10 ⁻³	Fe ²⁺	1.75× 10 ⁻³
Cl ⁻	5.73× 10 ⁻³	Ca ²⁺	1.49× 10 ⁻³	Cl ⁻	1.71× 10 ⁻²
Ca ²⁺	1.99× 10 ⁻³	HCO ₃ ⁻	1.12× 10 ⁻²	Ca ²⁺	1.81× 10 ⁻³
HCO ₃ ⁻	5.09× 10 ⁻³			HCO ₃ ⁻	8.69× 10 ⁻⁴
Charge balance error	0.34%	Charge balance error	0.19%	Charge balance error	2.02%

Source: AECOM, (2016). Analytical and wellhead data collected at the multi-port samplers at the DSA high-density sampling test array at the Chambers Works Site (secure server).

Table 4.6 Ion Concentrations in Simulated Groundwater

Upper Zone (GW1)		Zone 1 (GW2)		Zone 3 (GW3)	
Species	Concentration (mol/L)	Species	Concentration (mol/L)	Species	Concentration (mol/L)
SO ₄ ²⁻	6.84× 10 ⁻⁴	SO ₄ ²⁻	1.36× 10 ⁻³	SO ₄ ²⁻	3.96× 10 ⁻³
Na ⁺	6.63× 10 ⁻³	Na ⁺	1.47× 10 ⁻²	Na ⁺	1.47× 10 ⁻²
Cl ⁻	5.86× 10 ⁻³	Cl ⁻	5.58× 10 ⁻³	Cl ⁻	1.71× 10 ⁻²
Ca ²⁺	1.99× 10 ⁻³	Ca ²⁺	1.49× 10 ⁻³	Ca ²⁺	1.81× 10 ⁻³
Mg ²⁺	8.12× 10 ⁻⁴	Mg ²⁺	8.90× 10 ⁻⁴	Mg ²⁺	4.32× 10 ⁻³
HCO ₃ ⁻	5.09× 10 ⁻³	HCO ₃ ⁻	1.12× 10 ⁻²	HCO ₃ ⁻	8.69× 10 ⁻⁴
Charge balance error	0.34%	Charge balance error	0.19%	Charge balance error	2.02%

4.10 Batch Studies of Chlorinated Solvents Degradation

Three types of sample groups were used in this study:

A Blank Group without minerals or sediments but with the same groundwater conditions and COC;

Two control groups using siderite and pyrite minerals that include the pure mineral, groundwater condition, and the COC;

Sediments from the Upper Zone, Zone 1, and Zone 3 with the associated groundwater and COCs.

The standard solutions of benzene (C_6H_6), mono-chlorobenzene (C_6H_5Cl), 1,4-dichlorobenzene ($C_6H_4Cl_2$), PCE, TCE, chloroacetylene, 1,1-dichloroethylene (1,1-DCE), 1,2-dichloroethylene (*cis*-DCE) and vinyl chloride (VC) for gas chromatography measurements were purchased from Restek. The bench-scale experiments for studying abiotic dehalogenation of each COC (i.e., 1,4-DCB, PCE, and TCE) were conducted in a glovebox; the method used is a modification from Schaefer et al. (2018a). In the 1,4-DCB study, approximately 38 ml of simulated groundwater and sediment (targeting 3 g L⁻¹ of Fe(II) concentration) were added to each amber 40-ml borosilicate vial with PTFE Mininert valve caps (Thermo Scientific) and sealed with PTFE tape. Each reactor was filled without headspace for GC analyses with the aqueous sample. 1,4-DCB solution was added to each amber vial with a PTFE gastight glass syringe and an initial concentration of 30 mg L⁻¹. In PCE and TCE studies (Table 4.7) an initial concentration of 20-30 mg L⁻¹ was applied and 5 ml of headspace in each 40 ml vial remained for gas-phase analyses. All reactors were orbitally shaken at 400 rpm for turbulent conditions (Appendix B). In the 1,4-DCB, PCE, and TCE studies, sample periods were extended to 138 h, 68 h, and 68 h, respectively. After the last sample collection, sample vials were centrifuged (1000 rpm for 1 hour) to remove the aqueous phase and methanol was added for VOC extraction from the sediment (EPA 5035a (2002)).

The aqueous phase concentrations of 1,4-DCB, chlorobenzene, and benzene were determined following EPA Methods (5030C (U.S.EPA, 2003) and 502.2 (U.S.EPA, 1995)). Samples (0.01 ml) were collected from each 40 ml vials, diluted with DI water, and filtered for analysis (U.S.EPA, 1995). Samples were injected into Tekmar LSC2 for 12 minutes, purged with a N₂ flow of 40 ml/min, trapped on a Carboxen B/Carboxen 1000 & 1001 trap (Supelco) at room temperature, and then desorbed at 250 °C for 6 minutes. The GC (Varian 3400) was equipped with Restek column (105 m × 0.53 mm × 3.0 μm Rtx-502.2) and PID (hydrogen pressure 11.0 psi; temperature program: initial 40 °C hold for 2 minutes with an increase to 240°C at 8°C/min and held for 5 minutes). The retention time for each sample was 28 minutes. The column temperature was raised to 260 °C for 4 minutes between each sample. The total concentration of 1,4-DCB was based on aqueous and sediment extraction.

In PCE and TCE studies, the gas phase sample (10 μL) was collected from each 40 ml reactor with a gastight syringe following EPA 5021A (U.S.EPA, 2014) Method. Samples were manually injected into GC (Hewlett Packard 6890) equipped with Restek fused silica column (30 m × 0.25 mm × 0.25 μm) and MS (Agilent 5973). Six compounds analyzed included PCE, TCE, chloroacetylene, 1,1-dichloroethylene (1,1-DCE), 1,2-dichloroethylene (*cis*-DCE), and vinyl chloride (VC) and were quantified with an MSD ChemStation E.02.01.117 (Agilent Technologies). Acetylene and reduced gases (e.g., ethene and ethane) were qualified with ion chromatograph extraction (Smoluch et al., 2019). Aqueous concentrations were calculated based on Henry's law (20°C) (Table S1). Concentrations reported the pseudo-first-order kinetic model has been frequently used to characterize iron-mediated degradation of contaminants reduction (Johnson et al., 1996). At a constant pH, the rate expression for dechlorination of COC is expected to follow a second-order rate expression in Equation (4.1):

Table 4.7 Initial Concentrations of Experimental Groups

Group	Initial Sediment weight (g)	Iron Mineral Concentration (g/L)				Total Fe(II) Concentration with SE (g/L)
		Mackinawite (FeS)	Pyrite (FeS ₂)	Siderite (FeCO ₃)	Magnetite (Fe ₃ O ₄)	
Pyrite	0.1	NA	2.57	NA	NA	NA
Siderite	0.19	NA	NA	4.75	NA	NA
Upper Zone	7.3	1.18	1.10	0.65	2.28	2.68
Zone 1a	4.7	0.19	2.07	1.15	2.78	2.99
Zone 1b	3	0.73	1.88	1.00	1.08	2.35
Zone 3	10.23	1.23	0.97	8.55	0.55	5.64

NA=no applicable

$$-\frac{d[\text{COC}]}{dt} = k_1 [\text{Iron Mineral}][\text{COC}] \quad (4.1)$$

where k_1 is the second-order rate constant ($\text{L g}^{-1} \text{h}^{-1}$), and $[\text{Iron Mineral}]$ (g L^{-1}) and $[\text{COC}]$ (g L^{-1}) are the concentrations of Fe mineral coatings and COC, respectively. Because the concentrations of reactive Fe minerals are much greater than the COC concentration, the rate expression is treated as pseudo-first order in Equation (4.2):

$$-\frac{d[\text{COC}]}{dt} = k_1' [\text{COC}] \quad (4.2)$$

where k_1' is the pseudo-first order rate constant (h^{-1}). Four dominant Fe(II) mineral coatings were found in RTZs sediment: mackinawite (FeS), pyrite (FeS_2), siderite (FeCO_3), and magnetite (Fe_3O_4). Each reactive iron mineral coating contributes to the dechlorination process, and hence the rate expression can be written as Equation (4.3):

$$k_1' = k_{(\text{FeS})}[\text{FeS}] + k_{(\text{FeS}_2)}[\text{FeS}_2] + k_{(\text{FeCO}_3)}[\text{FeCO}_3] + k_{(\text{Fe}_3\text{O}_4)}[\text{Fe}_3\text{O}_4] \quad (4.3)$$

where $k_{(\text{FeS})}$, $k_{(\text{FeS}_2)}$, $k_{(\text{FeCO}_3)}$, and $k_{(\text{Fe}_3\text{O}_4)}$ are the forward second order rate constants ($\text{L g}^{-1} \text{h}^{-1}$); and $[\text{FeS}]$, $[\text{FeS}_2]$, $[\text{FeCO}_3]$, and $[\text{Fe}_3\text{O}_4]$ are the concentrations (g L^{-1}) of Fe mineral coatings in the system. In the four RTZs sediments, four pseudo-first order reaction rate constants were observed based on Equation (4.2); the second-order rate constants (based on the mass) of dominant Fe(II) mineral coatings can be determined through Equation (4.3).

CHAPTER 5

CHARACTERIZING THE REDUCTION-OXIDATION TRANSITION ZONES OF A SITE WITH HISTORICAL CONTAMINATION

In this section, results from profile analyses were instrumental in determining redox transition zones in the 18.3-m anoxic core sediment. The gradients from geochemical data correlated with dominant bacteria supporting the Fe cycling expected in contaminated systems.

5.1 Screening Analyses

Elemental concentrations in the sediment help to resolve the composition of bulk and mineral coatings and are an indicator of mineral coating precipitation and dissolution which highlighted the potential transition zones. In the discussion below, correlating sediment composition with other characteristics including sediment ORP, pH, abundant bacteria, and TVOCs, the resulting gradients helped to resolve redox transition zones.

5.1.1 Dominant Element

Dominant element (atomic number >12) concentrations in sediment (Figure 5.1) included silicon, iron, aluminum, phosphorus, titanium, and sulfur. Silicon was the most abundant. The second most abundant element observed in the sediment was Fe, which was extensively used at the site. Sulfur, abundant from the use of sulfuric acid, was another important raw material used extensively. Additionally, phosphorus compounds were among the raw materials used on site (Dupont, 2006). As a result, P concentrations were relatively constant with depth, with one exception being the 17.69 m to 19.52 m DBS interval where P concentrations increased from 3,508 mg/kg to 18,629 mg/kg. Interestingly, Ti trended similarly with Al throughout the 18.3 m core,

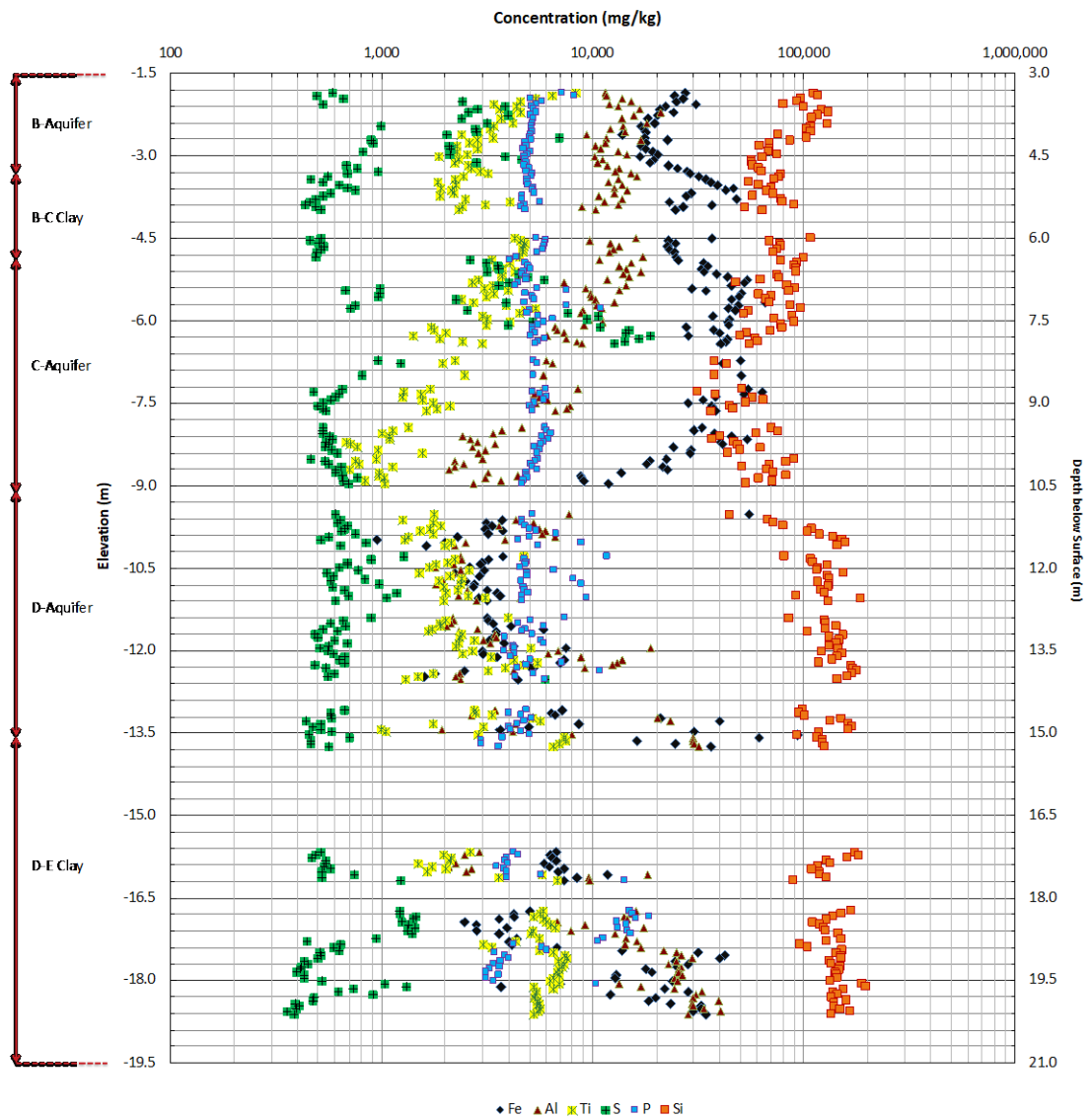


Figure 5.1 Dominant elements from X-ray fluorescence spectrometry (XRF) analysis as function of depth in the 18.3-meter core [left axis: elevation to the sea level (in NAVD 88 system) (m); right axis: depth below surface (m)]. Aquifer and aquitard information are shown as well.

which may be due to both Al and Ti being associated with bulk minerals such as albite, muscovite and feldspars.

Gradients in Fe and S concentrations are important in identifying redox transition zones. As a function of DBS, increases in sediment S concentration over several orders of magnitude together with corresponding increases in Fe concentration suggest precipitation of Fe sulfide minerals in a reduced environment (Figure 5.1). On the other hand, in an oxidized environment, increasing S may suggest the presence of sulfate minerals, such as gypsum. Concentrations observed of both Ca and S demonstrate saturation of gypsum at 10.07 to 10.22 (m) DBS, 11.44 to 11.59 (m) and 13.58 to 13.73 (m) (Appendix C). While the elevated Fe and S concentrations reflect the reactive mineral coatings present as well as potentially bulk mineralogy, their gradients in subsamples of the 18.3 m core are evidence of the redox transition zones (Figure 5.1). Fe gradients reflect cycling of the reactive Fe mineral coatings in redox transition zones. As the redox condition becomes more reduced and Fe(III) transforms to Fe(II), the latter species will undergo dissolution owing to the greater solubility of ferrous versus ferric minerals (Diakonov et al., 1999). Moreover, when S is present, sulfate-reducing conditions result in its transformation to a range of reduced-sulfur intermediates, including sulfide. Fe(II) sulfide minerals are sparingly soluble, resulting in increased concentrations of sulfide associated with sediments (Rickard and Luther, 2007). The solubility of Fe(II) in siderite (FeCO_3) is greater than that in mackinawite (FeS) (Bénézeth et al., 2009). Therefore, gradients in Fe concentrations will be observed when the system becomes more reduced and Fe(II) dissolution occurs. With sulfate-reducing conditions (and in the presence of S species), S and Fe concentrations associated with the solids (sediments) will increase because of Fe sulfide precipitation

(Canfield et al., 1992; Ford et al., 1997; Noël et al., 2014; Qafoku et al., 2009). Overall, gradients in Fe and S concentrations are important in identifying redox transition zones.

Fe and S concentrations demonstrate several significant gradients ($p < 0.05$) throughout the 18.3 m profile (Figure 5.2). At shallower depths [DBS: 3.97 m – 4.58 m (Upper Zone) and 6.41 m – 7.32 m (Zone 1)] where Fe and S concentrations increase, precipitation of iron sulfide minerals is expected. From 9.46 m to 11.48 m DBS, Fe levels decrease by an order of magnitude, and when coupled with lower S concentrations in the sediment, Fe(II)-mineral dissolution is expected. Under this condition, Fe(II) carbonate (siderite) and Fe(II)/(III) minerals such as magnetite are potential mineral coatings in the zone. Between the D-Aquifer and D-E Clay, the Fe concentration gradient spans an order of magnitude over a 0.61 m interval corroborating the need for a more detailed analysis of surface coating composition, Fe speciation, mineralogy, and morphology ((Hua et al., 2020)).

5.1.2 Sediment Redox Potential (ORP)

Sediment redox potential (ORP) revealed several significant zones of gradients over the depth of the 18.3-meter core (Figure 5.2). Gradients were observed in ORP data ranging from a low of -200 mV to a high of +700 mV, coinciding with regions where sediment Fe and S concentration gradients were also observed. These conditions are likely a result of both abiotic and biotic processes as well as dissolved O₂ via groundwater flow. In the redox transition zones (DBS: 9.46 m -10.68 m and 14.95 m -15.25 m), as the sediment ORP decreases as a function of depth and the condition becomes more reducing, dissolution of Fe(II) will lower the sediment Fe concentration, which is expected at lower S concentrations (< 1,000 ppm). Under sulfate-reducing conditions (e.g., indicated by presence of OTUs matching to known genera of sulfate-reducing

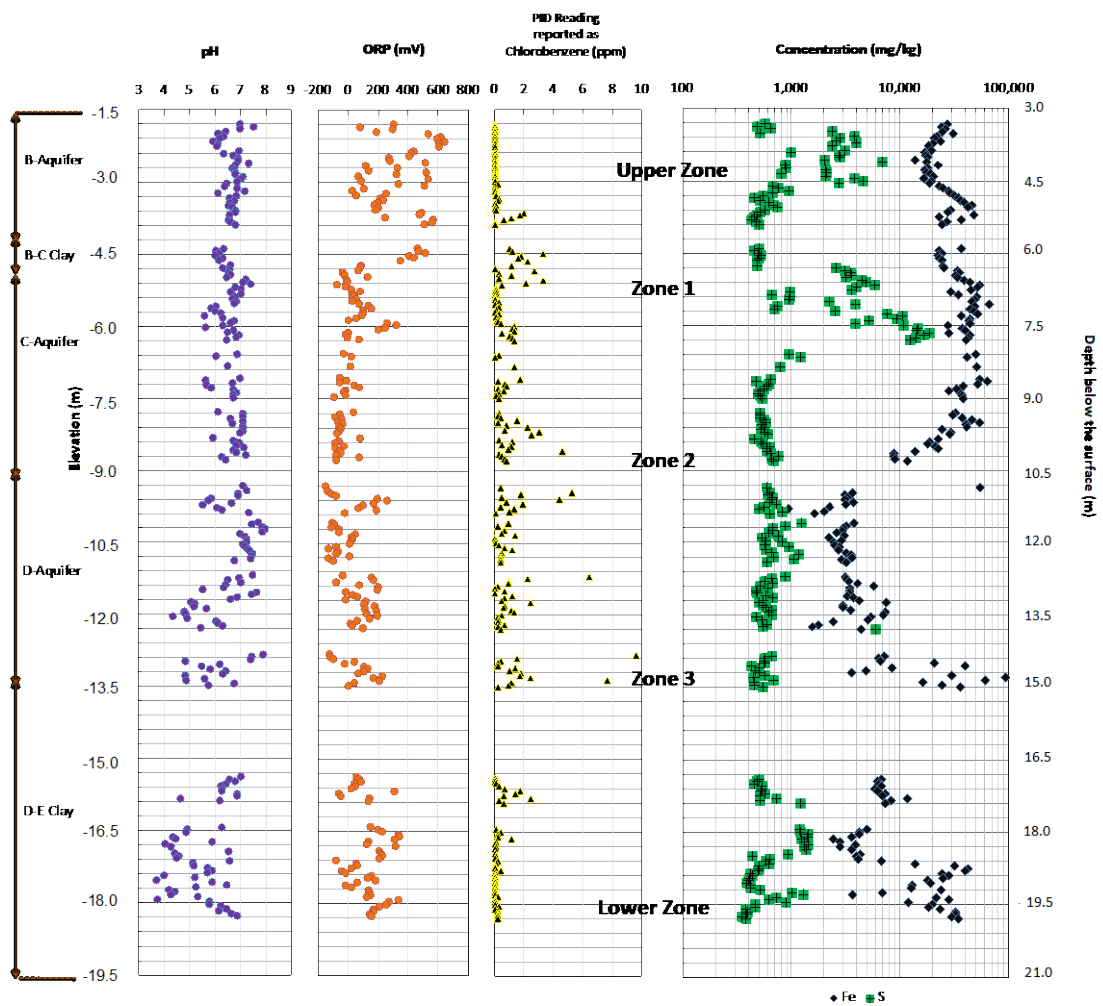


Figure 5.2 Profiles of sediment pH, sediment oxidization-reduction potential (ORP) (mV), photoionization detector (PID) reading reported as chlorobenzene (ppm), and Fe and S concentrations (mg/kg) from X-ray fluorescence spectrometry (XRF) analyses. The left axis shows elevation (m) and the lithology; the right axis gives depth below surface (m). Five redox transition zones highlighted in blue are identified based on the data.

bacteria and low ORP), S concentrations increased in the sediment and precipitation of sparingly soluble Fe sulfide minerals is expected (DBS: 6.41 m -7.32 m). From 6.71 m to 7.02 m (DBS), although the ORP increases from -63 mV to +136 mV, still reflecting an overall reduced environment, Fe and S concentrations increase in the sediment; Fe sulfide minerals are expected to dominate. Similar conditions of increasing ORP are observed at a DBS of 14.64 m to 14.95 m where siderite and magnetite are also expected to be dominant in the sediment. While the redox potential for a pure or well-defined mineral phase can be determined through mediated electrochemical analyses (Gorski et al., 2012b; Hoving et al., 2017), in a complex system such as a sediment where there are multiple reactive mineral coatings, the redox potential between the sample and the working electrode is likely dynamic and not at equilibrium (Gorski et al., 2012a). In addition, the measured ORP is likely a mixed potential reflecting the reactive (Fe) minerals coatings present.

5.1.3 Sediment pH

Sediment pH ranged from 3.8 to 8 with several gradients throughout the 18.3-meter (Figure 5.2). At depths where Fe and S concentration gradients were found (i.e., 3.32 – 4.58 m, 6.41 m – 7.02 m, and 9.46 m – 10.68 m DBS), these potential redox transition zones are in circumneutral pH environments. Generally, the observed pH conditions were conducive to conditions required by observed associated bacteria. For example, pH 6 to 8 is conducive for the Fe-reducing bacteria *Geobacter* which is likely abundant at DBS 3.05 m to 13.12 m (Schwertmann and Fitzpatrick, 1993; Straub et al., 2001). Several gradients in sediment pH were observed at the deeper depths, where clay lenses are found. Over the course of site operations, over 700 products were produced; sulfuric acid was used throughout its history. As a result, contaminants including acids may

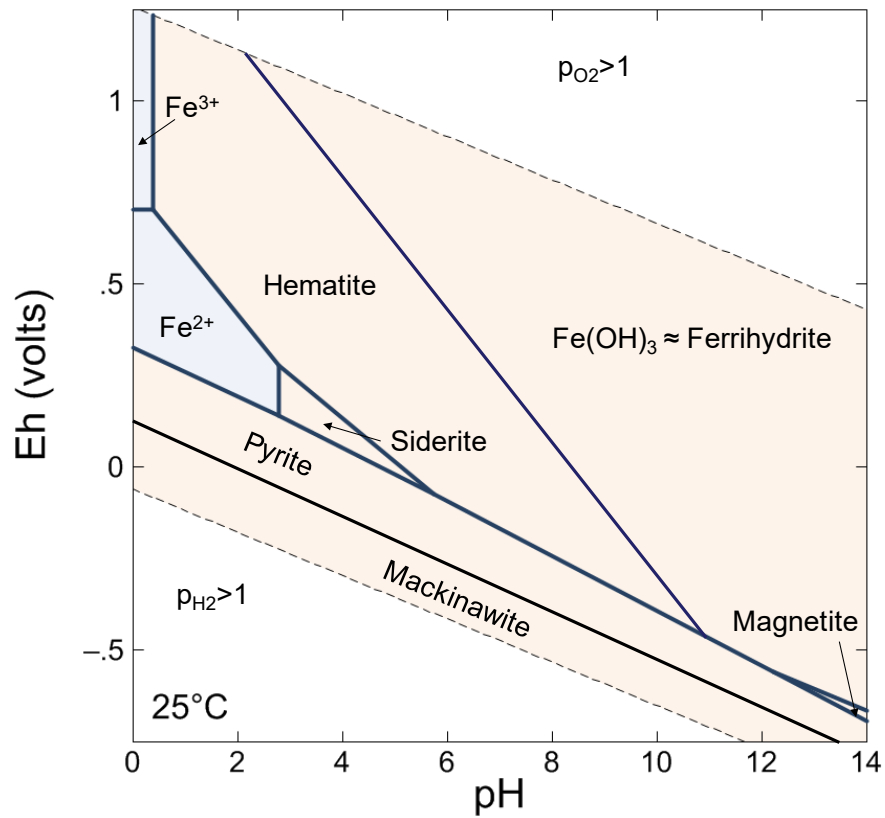


Figure 5.3 pH-E_h diagram for Fe-CO₂-S-H₂O system (25°C; 100 bars; 1 mol/kg of Fe; 10⁻³ mol/kg of S; 10⁻³ mol/kg of C; E₀ vs. SHE) (modeled with Geochemist's Workbench 13)¹. Fe and S concentrations depicted in the model are representative of sediment samples with these element concentrations.

¹Bethke, Craig M. *Geochemical and biogeochemical reaction modeling*. Cambridge University Press, 2007.

accumulate in aquitard layers reducing sediment pH. At a mineral-aqueous interface, biogenically reduced Fe(II) and Fe(II) sulfide minerals (e.g., pyrite and mackinawite) may exist in less reduced environments (E_h ranges -450 mV to -250 mV) under acidic to neutral conditions (pH ranging from 4 to 8) compared to a more alkaline condition (Ning et al., 2013). At higher potentials, the thermodynamically stable Fe minerals hematite and magnetite, for example, and metastable ferrihydrite could be expected to precipitate as well in the anaerobic core over a pH ranging from 3.8 to 8 (Figure 5.3). In identifying redox transition zones, although sediment pH is not a direct indicator, the conditions resolve whether the environments support related (a)biotic processes (see in 5.1.4 Abundant Bacteria).

5.1.4 PID Measurements

PID measurements were collected for each 5.08 cm sample headspace (Figure 5.2). Elevated TVOC concentrations (reported as chlorobenzene) indicate contamination of sediment and what may be locations for potential (a)biotic degradation. However, nondetectable concentrations (DBS: 3.97 m -4.58 m and 18.91 m -20.13 m) may also suggest that degradation is active and an important process as well. In addition, nondetectable concentrations in the deepest samples from the core may indicate contaminants are not present. Using molecular results on the abundance of Fe and/or S reducing bacteria can support additional evidence of redox transition zones.

5.1.5 Abundant Bacteria

Abundant bacteria in the sediment are another important indicator of redox transition zones. Although we cannot exclude the impact of less abundant bacteria on overall processes, in several zones, certain OTUs made up $\geq 30\%$ of OTUs that support

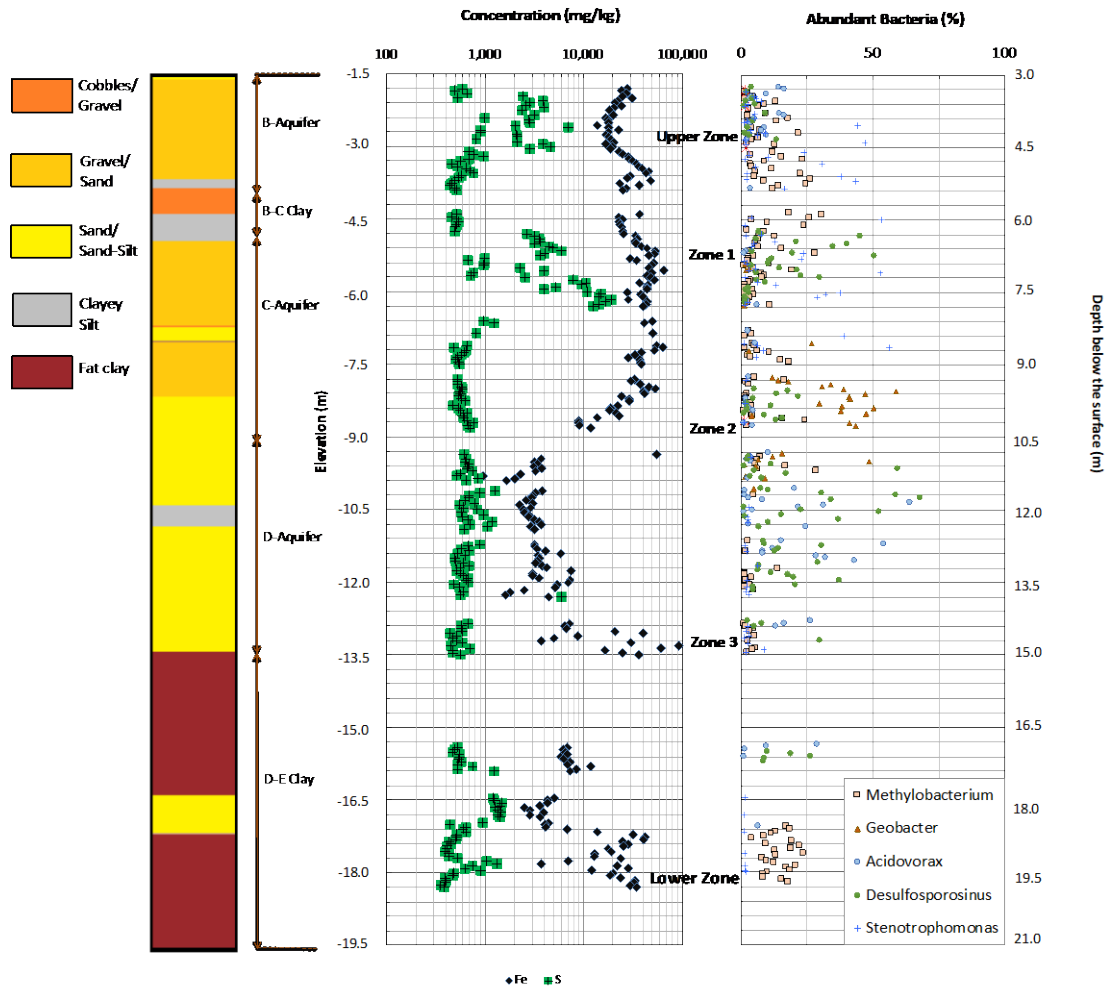


Figure 5.4 Aquifer, aquitard, and general matrix information from the Geo-log, Fe and S concentration (mg/kg) from XRF analysis, and abundant bacteria from 16S rRNA sequencing analyses.

theorized redox conditions in these locations. Five abundant OTUs observed throughout the 18.3-meter core matched up to 80% to the genera *Stenotrophomonas*, *Desulfosporosinus*, *Geobacter*, *Acidovorax*, and *Methylobacterium* (Figure 5.4 and Appendix D). At DBS 3.97 m to 5.49 m and 7.02 m to 8.85 m, OTUs matching to *Stenotrophomonas* were the most abundant (56% of OTUs). Palleroni and Bradbury (1993) classified the *Stenotrophomonas* genus and today there are more than 10 species reported. For example, *Stenotrophomonas maltophilia* MK2 is a facultative anaerobic bacterium isolated from a hydrocarbon-fed microbial electrochemical remediation system (MERS) that demonstrates hydrocarbonoclastic behavior for petroleum hydrocarbon (Venkidusamy and Megharaj, 2016). *S. maltophilia* strain C6 can utilize phenanthrene as a sole source for carbon and energy, degrading it to benzocoumarin (Gao et al., 2013). Other species in the genus of *Stenotrophomonas* have been found to be degraders of acenaphthylene, phenanthrene, 4-chloroanilines, and chlorocatechol (Andreoni et al., 2004; Nayak et al., 2009; Radianingtyas et al., 2003). On the other hand, *Stenotrophomonas* sp. with siderophores can transfer Fe^{3+} to Fe^{2+} (Jurkevitch et al., 1992). At DBS 3.97 m – 8.85 m, abundant OTUs match to genera *Stenotrophomonas* (56% of OTUs) and *Methylobacterium* (30% of OTUs); the *Methylobacterium* was also among the most dominant bacteria (30% of OTUs) at DBS 19.22 m to 20.13 m. *Methylobacterium* sp. have been found to degrade phenol (Khongkhaem et al., 2011), dichloromethane (Yu et al., 2017), N,N-dimethylformamide (Lu et al., 2019), and polycyclic aromatic hydrocarbons (PAHs) (Andreoni et al., 2004). Abundance of these organisms at DBS 3.97 m to 4.58 m and 19.22 m to 20.13 m could indicate active degradation zones because TVOC concentrations in the headspace were below the detection limit of the PID. Although this study did not directly measure the activity of the organisms, the bacteria genera

correlated with geochemical results can contribute to evidence in delineating redox transition zones.

At DBS 6.40 m to 7.02 m and 11.29 m to 15.25 m, OTUs matching to *Desulfosporosinus* were most abundant (67% of OTUs) in the sediment. *Desulfosporosinus* (at the genus level) was proposed as a sulfate-reducing bacteria in 1997 (Stackebrandt et al., 1997) and has been found in a PAH-contaminated (shallow) aquifer (Robertson et al., 2000), in an arsenic-contaminated groundwater (Zhang et al., 2017), and at a uranium disposal site (Bondici et al., 2016). *Desulfosporosinus* sp. strain GBSRB4.2 identified from an acid mine drainage system was observed with Fe(II) and Fe(III) minerals such as greigite (Fe_3S_4) (Bertel et al., 2012b).

From DBS 9.46 m to 10.68 m, an OTU closely related to *Geobacter* is most abundant at a maximum of 58% OTUs. Given the lower concentrations (<1,000 ppm) of S compared to Fe (>10,000 ppm), reduction of Fe is expected to result in its dissolution to $\text{Fe}^{2+}_{(\text{aq})}$ resulting in a lower Fe concentration associated with the sediment. The Fe-reducer *Geobacter* have the ability to consume energy from organic compounds using Fe(III) as the electron acceptor and are important organisms in the subsurface environment (Lovley, 1991). Biogenic Fe(II) minerals formed by *Geobacter* have also been found to play a role in the abiotic degradation of benzene (Anderson et al., 1998), Hg-methylation degradation (Kerin et al., 2006), and in transformation of dissolved U(VI) to sparingly soluble U(IV) such as UO_2 (Holmes et al., 2002). With Fe(III)-citrate as the electron acceptor and acetate as the electron donor at pH 7, vivianite ($\text{Fe}(\text{II})_3(\text{PO}_4)_2 \cdot 8\text{H}_2\text{O}$) was observed; when ferrihydrite was the electron acceptor, magnetite was found (Islam et al., 2005). With S present at concentrations (<1,000 ppm) an order of magnitude from less than Fe (>10,000 ppm) at DBS from 9.46 m to 10.68

m, the Fe(II) mineral siderite (FeCO_3) and the Fe(II)/(III) mineral magnetite (Fe_3O_4) are expected to be dominant.

At DBS 11.29 m to 15.25 m, the most abundant OTU (64% of total) is closely related to the genus *Acidovorax*. *Acidovorax* sp., are facultative bacteria, and are known degraders of PAHs (Eriksson et al., 2003) and poly(3-hydroxybutyrate) (Mergaert et al., 1993). Additionally, *Acidovorax* sp. strain BoFeN1 plays a role in reducing nitrate and oxidizing Fe(II) (Klueglein et al., 2014). At DBS 14.64 m to 14.95 m, Fe(III) minerals (e.g., goethite, hematite) may be forming to some extent in the presence of *Acidovorax*. From 14.95 m to 15.25 m (DBS), with a change in abundant bacteria to an OTU with similarity to *Desulfosporosinus*, a sulfate reducer, a more reduced environment is observed. At DBS 14.95 m to 15.25 m, decreased Fe concentrations and ORP measurements (Figure 5.2) revealed gradients indicative of a reduced environment as well. Therefore, at DBS 14.64 m to 15.25 m, dominant mineral coatings may range from oxidized Fe(III) minerals (e.g., goethite, hematite) in the shallowest part of the zone to reduced Fe(II) and Fe (II/III) minerals (e.g., siderite, magnetite) deeper in the zone. Surface coating mineralogy in transition zones is probed in other detail analysis (Hua et al., 2020).

5.2 The Redox Transition Zones

In summary, five redox transition zones were delineated based on gradients observed in Fe and S concentrations, the presence of abundant bacteria that correlated with Fe and S gradients, sediment ORP gradients, and to a lesser extent TVOC of sediment headspace (Figure 5.2 and Table 5.1):

Upper Zone (DBS: 3.97 m – 4.58 m; B-Aquifer with clay lenses)

Zone 1 (DBS: 6.41 m – 7.02 m; interface of B-C Clay and C-Aquifer)

Table 5.1. Summary Table of Screening Parameters in Five Redox Transition Zones

Identification (Depth below the surface (m))	pH (range)	ORP Readings (mV)	Highest PID Reading as chloro-benzene (ppm)	Fe Concentration (1000 ppm)			S Concentration (1000 ppm)			Abundant Bacteria
				Min.	Max.	Ave.	Min.	Max.	Ave.	
Upper Zone (3.97 – 4.58)	6.38 - 7.38	+76.1 - +538.6	Below detection limit	13.8	22.7	18.0	0.81	6.93	2.54	<i>Stenotrophomonas</i> <i>Methylobacterium</i> <i>Desulfosporosinus</i> <i>Acidovorax</i>
Zone 1 (6.41 – 7.02)	6.34 - 7.45	-63.5 – +136	3.3	29.4	54.0	38.2	0.67	5.90	3.39	<i>Desulfosporosinus</i> <i>Methylobacterium</i> <i>Stenotrophomonas</i>
Zone 2 (9.46 – 10.68)	5.98 - 7.27	-78.2 – +80.3	4.6	8.7	54.0	26.0	0.52	0.77	0.59	<i>Geobacter</i> <i>Methylobacterium</i> <i>Desulfosporosinus</i>
Zone 3 (14.64 – 15.25)	4.87 – 7.94	-108.6 - +233.8	9.6	3.6	93.1	27.1	0.44	0.70	0.53	<i>Desulfosporosinus</i> <i>Acidovorax</i>
Lower Zone (18.91 – 20.13)	3.74 - 6.91	-69.2 - +340	Below detection limit	3.67	42.2	16.1	0.36	1.32	0.61	<i>Methylobacterium</i> <i>Stenotrophomonas</i>

Zone 2 (DBS: 9.46 m – 10.68 m; interface of C-Aquifer and D-Aquifer)

Zone 3 (DBS: 14.64 m – 15.25 m; interface of D-Aquifer to D-E Clay)

Lower Zone (DBS: 18.91 m – 20.13 m; D-E Clay with silty sand layers)

Zones 1, 2, and 3 developed at the aquifer-aquitard interface, while the Upper Zone is an aquifer with clay lenses and the Lower Zone is an aquitard with a silty sand layer.

This result suggests that this interface plays potentially an important role in the development of these redox transition zones.

Upper Zone is located in the B-Aquifer with clay lenses (DBS 3.97 m - 4.58 m). The ORP ranges from a low of +76.1 mV to a high of +538.6 mV with a number of gradients in this 0.61-meter interval (Figure 5.2). The ORP at the shallowest depth is indicative of a reduced environment but then increases and decreases over a 400 mV range. Based on the O₂ concentration of sediment in the headspace (Figure 4.2), sharp gradients of sediment ORP may be driven by infiltration of rainwater into this shallowest aquifer. From 4.27 m to 4.58 m DBS, sediment Fe and S concentrations increase by as much as 20,000 ppm where metastable Fe sulfide minerals are expected to be abundant (Hua et al., 2020). The presence of *Stenotrophomonas* (degrader for petroleum hydrocarbons (Venkidusamy and Megharaj, 2016) and 4-chloroaniline (Radianingtyas et al., 2003)) and *Methylobacterium* (degrader for polycyclic aromatic hydrocarbons (PAHs) (Andreoni et al., 2004) and dichloromethane (Muller et al., 2011)) together with low TVOC concentrations suggest biotic degradation may be important (Figure 5.5). *Stenotrophomonas* is a facultative bacteria that has a high tolerance for variable oxygen concentrations compared to Fe- and S-reducing bacteria. In a reduced environment, Fe sulfide minerals such as pyrite (FeS), mackinawite (FeS₂), and greigite (Fe₃S₄) are expected to play an important role in dehalogenation.

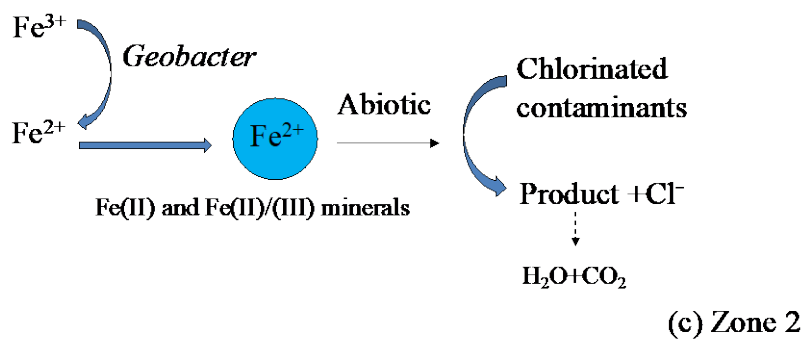
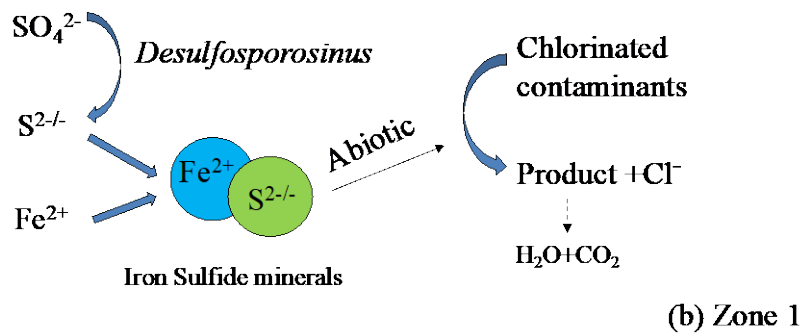
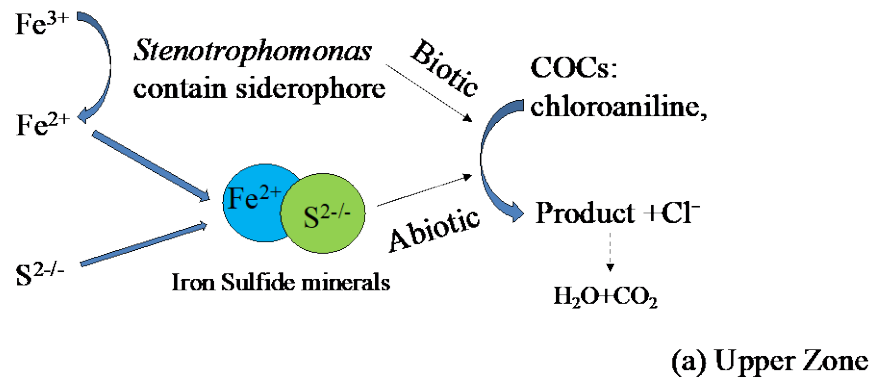


Figure 5.5 Potential cycling between Fe/S ion, microorganism, and chlorinated contaminants in the three redox transition zones: (a) Upper Zone, (b) Zone 1, and (c) Zone 2, where Fe(II) and Fe(II)/(III) mineral coatings are expected.

Zone 1 falls within the transition region between the B-C Clay and the C-Aquifer (Figure 5.4). Increasing Fe and S concentrations in the sediment were observed from DBS 6.41 m to 6.71 m where ORP also decreased (from 85.4 mV to -14.7 mV), resulting in the likely precipitation of Fe sulfide minerals. The presence of *Desulfosporosinus* (sulfate-reducing bacteria) based on OTUs further supports an anoxic environment (Figure 5.4). Given the gradient in TVOC concentrations along with elevated COC concentrations from MLS groundwater analyses (e.g., 170 mg/L aniline and 1,900 mg/L nitrobenzene (Figure 2.1)), degradation is expected. At 6.71 m to 7.02 m DBS, sediment ORP increases slightly from a more-reduced to a less-reduced environment. The Fe concentration in sediment increases, while the S concentration decreases. In this zone, Fe sulfide minerals may transform to Fe(II)/(III) minerals such as magnetite (Fe_3O_4) and greigite (Figure 5.5)

Zone 2 (DBS 9.46 m to 10.68 m) is delineated based on significant gradients ($p < 0.05$) observed using complementary analyses (Figure 5.2). Fe decreased over one order of magnitude at lower S concentrations while ORP readings were less than 0 mV, indicative of a reduced environment with Fe(II) minerals. The most abundant bacterial OTU is closely related to *Geobacter*, which suggests the cycling of Fe(III) to Fe(II) minerals. Reduced-iron mineral coatings such as siderite (FeCO_3) and the Fe(II)/(III) mineral magnetite (Fe_3O_4) are expected. Given the gradient in TVOC concentration, abiotic degradation may be an important process in this zone (Figure 5.5).

Zone 3 (DBS 14.64 m to 15.25 m) is located in the transition region from D-Aquifer to the D-E Clay aquitard where COCs accumulate (Figure 5.4). At DBS 14.64 m to 14.95 m, the Fe concentration is increasing (Figure 5.2) and is coupled with an increasing ORP from -108 mV to +234 mV. With S concentrations orders of magnitude lower than those of Fe, possible mineral coatings may include Fe(II)/(III) minerals,

magnetite and green rust ($\text{Fe}^{2+}_4.5\text{Mg}_{1.5}\text{Fe}^{3+}_2(\text{OH})_{18}\cdot 4(\text{H}_2\text{O})$), and Fe (III) oxyhydroxide minerals (e.g., goethite ($\alpha\text{-FeOOH}$), hematite (Fe_2O_3), and lepidocrocite ($\gamma\text{-FeOOH}$)). *Acidovorax* was an abundant OTU in this zone and is a known degrader of chlorobenzenes (Monferrán et al., 2005) and PAHs (Eriksson et al., 2003; Mergaert et al., 1993). In the deeper part of the zone (DBS: 14.95 m to 15.25 m), Fe concentrations and ORP (+234 mV to -45 mV) decreased, indicating precipitation of Fe(II) minerals such as magnetite and siderite (given the lower S concentrations). TVOC concentrations ranged from below detection limit to 7.6 ppm, indicating a potentially contaminated area with degradation.

Lower Zone at 8.91 m to 20.13 m is located in the D-E Clay phase with reddish and grey color. Unique from other aquitard areas, the PID readings are below the detection limit in this zone. From DBS 18.91 m to 19.52 m, pH ranged from 6 to 8 and ORP increased from -100 mV to +200 mV. S concentrations decreased as well, while Fe concentrations increased. At DBS 19.52 m to 19.83 m, S concentrations increased and Fe concentrations decreased with an ORP suggestive of a reduced and acidic (pH as low as 3.8) environment. Fe sulfide minerals are expected at this depth. At a deeper depth (DBS 19.83 m -20.13 m), Fe concentrations increased at lower S concentrations and an ORP ranging from +200 mV to +380 mV. Reactive Fe minerals may range from Fe(III) minerals (e.g., magnetite, hematite) to the reduced Fe sulfide minerals (e.g., pyrite and mackinawite). The reddish clay is indicative of the presence of Fe. Given the abundance of *Methylobacterium* (degrader of dichloromethane (Muller et al., 2011) and PAHs (Andreoni et al., 2004)) along with sediment pH, sediment ORP, and low TVOC concentrations, (a)biotic degradation may be occurring.

5.3 Summary

The methodology in this study demonstrates a systematic approach for identifying redox transition zones. An 18.3-meter anoxic core was collected where the redox condition of the sediment was preserved during the collection, transportation, sampling, and analytical processes. Screening analyses of a total of 225 (5.08 cm) subsamples provided a continuous biogeochemical profile as a function of depth for sediment ORP, sediment pH, Fe and S concentrations, TVOC concentration in the headspace, and abundant bacterial genera. Over the core's length, gradients were observed in sediment pH, sediment ORP, and Fe and S concentrations. The Fe and S gradients correlated with the presence of Fe and S reducing bacteria. For example, S concentrations peaked in the Upper Zone and Zone 1 where *Desulfosporosinus* was abundant, suggesting precipitation of iron sulfide minerals. In Zone 2, Fe concentrations decreased where *Geobacter* was abundant, resulting in potentially Fe reduction, dissolution, and precipitation of minerals with increased solubility compared to the Fe(III) minerals. Using complementary geochemical and microbial data, five redox transition zones were delineated. Reduced iron sulfide mineral coatings are expected in the Upper Zone, Zone 1, and the Lower Zone where both elevated concentrations and gradients were observed for Fe and S. In Zone 2, given abundant bacteria and Fe gradients, Fe(II) and Fe(II)/(III) minerals are expected to be the dominant coatings. Finally, Zone 3 revealed a significant gradient in Fe concentration along with a reduced ORP, reflecting a reduced environment. Interestingly, Zones 1, 2, and 3 developed at the aquifer-aquitard interface, while the Upper Zone is an aquifer with clay lenses and the Lower Zone is an aquitard with a silty sand layer. The results suggest that these interfaces potentially play an important role in the development of redox transition zones, where there is an intersection of mineral coatings, contaminants, and groundwater inputs.

CHAPTER 6

ASSESSING REACTIVE IRON MINERAL COATINGS IN REDOX TRANSITION ZONES WITH SEQUENTIAL EXTRACTION

Analytical results from a six-step sequential extraction process have been used to isolate and qualify the reactive Fe mineral phases in four RTZs; a vertical profile of the distribution of reactive Fe mineral coatings as a function of depth is evaluated. The sample resolution of 5.06 cm sample interval was applied and correlated with other analyses including the abundant bacteria (discussed in the Chapter 5). This study helps to resolve the forms of reactive Fe mineral coatings, their concentrations needed for studying abiotic attenuation, and correlations with bacteria in the RTZs where natural attenuation is expected to be significant.

6.1 Distribution of Reactive Fe Mineral Coatings in Redox Transition Zones

From the six-step SE process, reactive Fe mineral coatings in sediments from the four RTZs were extracted, including ion exchangeable Fe^{2+} , Fe carbonate siderite, amorphous iron minerals (i.e., mackinawite, ferrihydrite, and 40-67% of greigite), Fe (oxyhydr)oxide (i.e., goethite, lepidocrocite, and hematite), Fe(II/III) magnetite, and crystalline Fe sulfide pyrite (Figures 6.1 and 6.2). In the Upper Zone (Figure 6.1) (DBS: 3.96 to 4.52 m), ion exchangeable Fe^{2+} ranged from 97 to 345 mg/kg throughout the depth. From 3.96 to 4.12 m DBS, the shallowest depth of the Upper Zone, siderite increased from 1,065 to 1,466 mg/kg. Amorphous Fe mineral coatings, including mackinawite and greigite, increased from 518 to 2,421 mg/kg while pyrite decreased from 4,636 to 1,055 mg/kg at the same depth. The dominant reduced form of Fe sulfide transitioned from the thermodynamically stable crystalline pyrite to metastable mackinawite. At this shallower depth, Fe (oxyhydr)oxide declined from 5,512 to 1,782

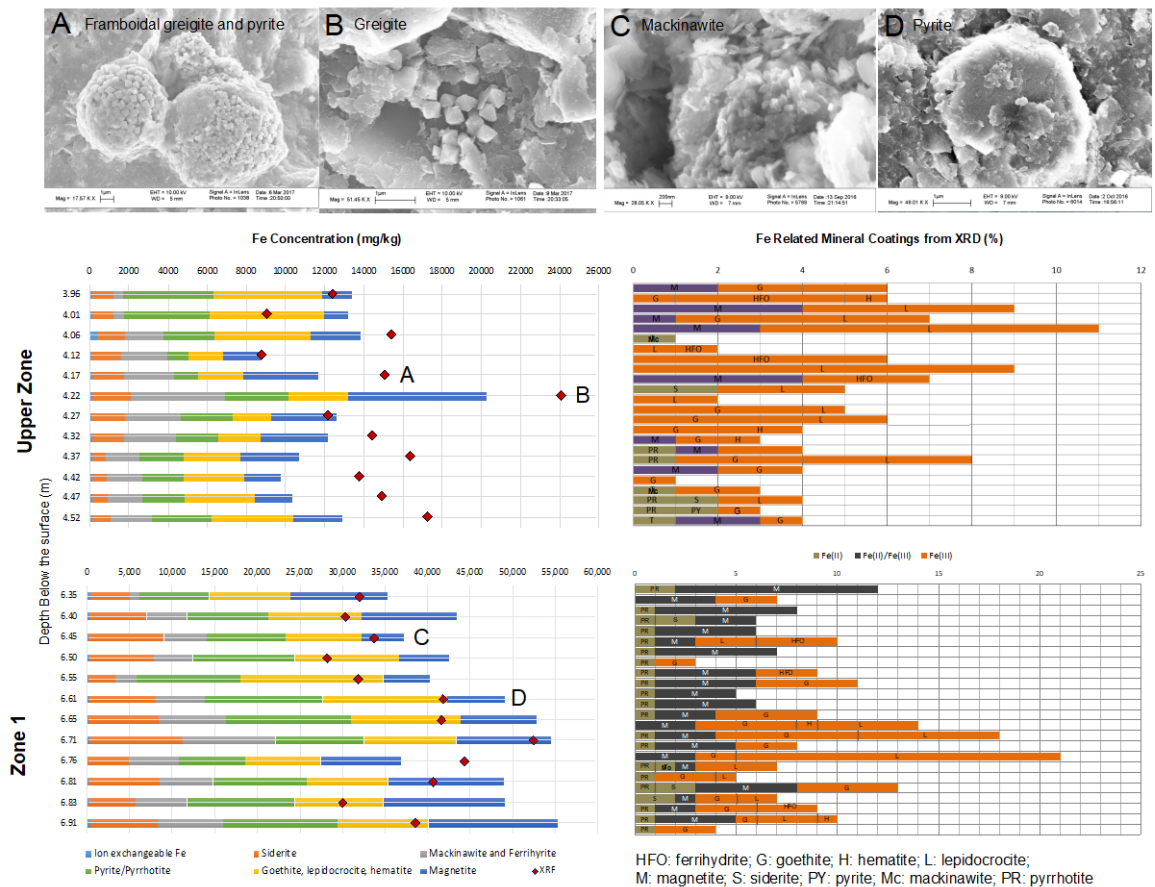


Figure 6.1 Fe concentrations (mg/kg) from the six-step SE (left) compared with XRD-defined Fe mineral coatings* (right) in Upper Zone (3.96 to 4.57 m DBS) and Zone 1 (6.40 to 6.96 m DBS). Fe mineral coatings characterized by FESEM/EDX* from these two RTZs (top) include: (A) framboidal greigite and pyrite, (B) greigite, (C) mackinawite, and (D) pyrite.

Source: FESEM/EDX images and XRD results of Fe mineral coatings in RTZs are reported by Hua, H., Yin, X., Dyer, J.A., Landis, R., Axe, L., 2020. Characterizing reactive iron mineral coatings in redox transition zones. *ACS Earth and Space Chemistry*. 4(12), 2337–2346.

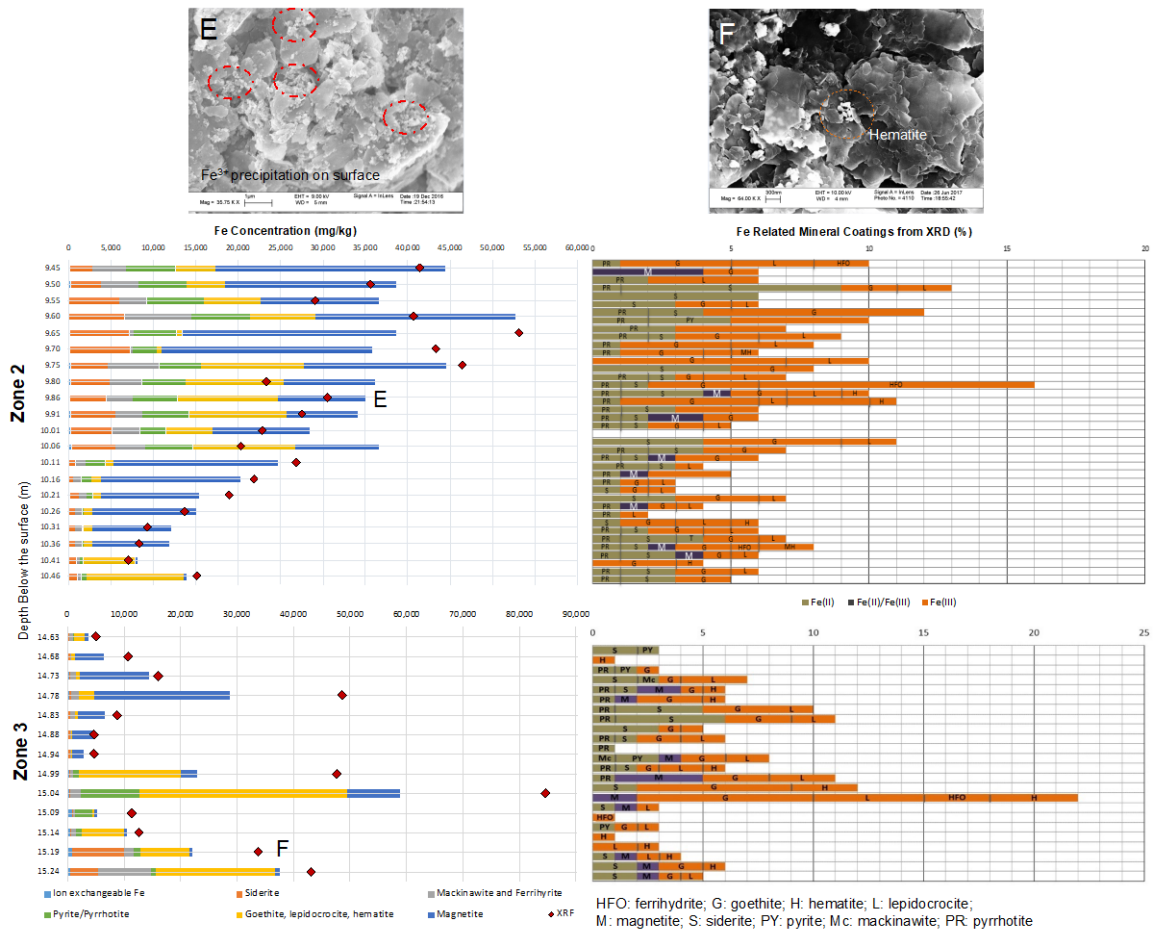


Figure 6.2 Fe concentrations (mg/kg) from SE in Zone 2 (9.45 to 10.46 m DBS) and Zone 3 (14.63 to 15.24 m DBS) are presented at left, along with characterized Fe mineral coatings (XRD)* at right. Fe(III) mineral coatings* including (E) goethite (needle shape), ferrihydrite (irregular spherical shape), and lepidocrocite (scale or tablet shape) and (F) hematite were identified by FESEM/DEX (top).

Source: XRD and FESEM/EDX results are reported by Hua, H., Yin, X., Fennell, D., Dyer, J.A., Landis, R., Morgan, S.A., Axe, L., 2021. Roles of reactive iron mineral coatings in natural attenuation in redox transition zones preserved from a site with historical contamination. *Journal of Hazardous Materials*. 420: 126600.

mg/kg with magnetite ranging from 1,584 to 1,958 mg/kg. The decrease in Fe(III) minerals accompanied with an increase in Fe(II) mineral coatings demonstrates a more reduced environment at a deeper depths within this transition zone. Midway into the Upper Zone (DBS: 4.12 to 4.22 m), total Fe concentrations increased by one order of magnitude to 20,223 mg/kg and this trend is consistent with XRF results. At this depth, an increase in Fe(II) and Fe(II/III) mineral coatings indicated a reduced environment. Amorphous Fe minerals, including metastable mackinawite and greigite, are higher in concentration than pyrite. Framboidal greigite and pyrite have been observed by FESEM/EDX analyses at the same depth (Figure 6.1) (Hua et al., 2020). Additionally, Fe(II/III) magnetite was observed as a dominant mineral with concentrations increasing from 1,958 to 7,037 mg/kg; this mineral coating was also found with XRD.(Hua et al., 2020) At greater depth in the Upper Zone (DBS from 4.22 to 4.52 m), concentrations of reactive iron mineral coatings decreased; The percentage of extracted Fe(II) minerals (siderite, amorphous mackinawite, greigite, and pyrite) to total extracted Fe (Figure 6.3) ranged from 45% to 55%. These Fe(II) minerals were also found with XRD.(Hua et al., 2020) Overall, the dominant reactive Fe mineral coatings in the Upper Zone include amorphous and crystalline Fe sulfides along with Fe(II/III) magnetite. He et al.(2015) summarized a trend for abiotic degradation of chlorinated solvents with reactive iron minerals: mackinawite > zero-valent Fe > pyrite > sorbed Fe²⁺ > green rust = magnetite. Given the abundance of amorphous Fe sulfide mineral coatings, this RTZ is expected to play an important role in the abiotic degradation of contaminants.

In Zone 1 (DBS: 6.35 to 6.91 m), both reduced and oxidized Fe mineral coatings were extracted throughout the zone. However, the total concentration of Fe via SE is from 10 to 45% higher than the concentration measured with XRF (Figure 6.1). This result may be attributed to the rinse between each extraction step and the uncertainty

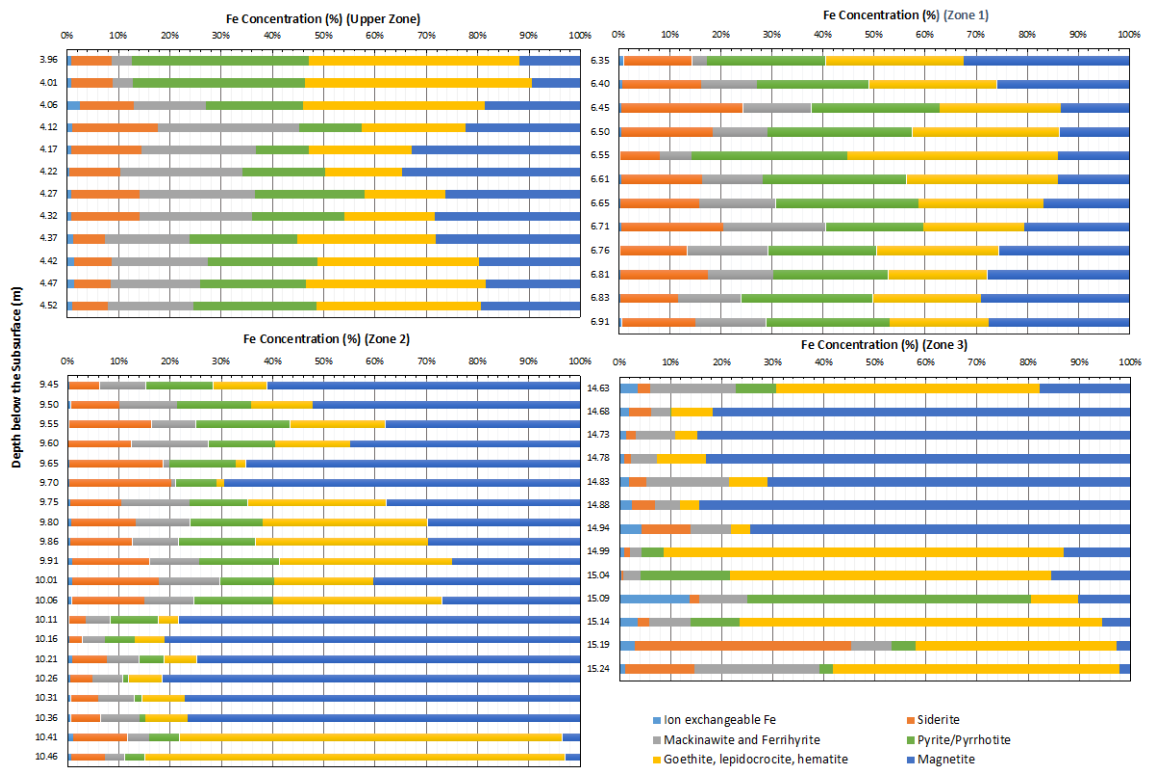


Figure 6.3 Distribution of Fe minerals in total extracted Fe (%) in sediment from the four redox transition zones.

associated with extractions, which is reported to range from 10 to 30% (Rodgers et al., 2015). Ion exchangeable Fe^{2+} was found at concentrations less than 377 mg/kg, while siderite ranged from 3,135 to 10,860 mg/kg without a clear trend. Pyrite, on the other hand, accounted for 20 to 30% (8,224 to 14,797 mg/kg) of the total concentration of Fe mineral coatings. Compared to the other three RTZs, the highest concentration of pyrite was observed in Zone 1. Reduced Fe mineral forms, siderite and pyrite, indicate a reduced environment in this RTZ. Amorphous minerals present included mackinawite and greigite (Posfai et al., 1998; Zhang et al., 2021a) and increased from 1,040 to 10,980 mg/kg as a function of depth. Although ferric mineral coatings ranged from 9,582 to 16,697 mg/kg in the sediment, the fraction of ferric minerals to the total extracted Fe decreased from 20% to 30% between 6.55 and 6.91 m DBS (Figure 6.3). Additionally, contributions from magnetite increased from 15 to 28% at this same depth. Reduced Fe minerals mackinawite and greigite increased with increasing depth along with Fe(II/III) magnetite, whereas the concentrations of Fe(III) (oxyhydr)oxide minerals decreased; this trend reveals a more reduced environment at greater depth in Zone 1. Consistent with SE, pyrite and magnetite were detected by XRD throughout most of this zone (Hua et al., 2020). Dominant reactive Fe mineral coatings in Zone 1 include magnetite and pyrite with the latter clearly attributed to the presence of sulfate-reducing bacteria *Desulfosporosinus* genera (Figure 5.4) as discussed below in Section 6.2.

In Zone 2 (Figure 6.2), between 9.45 and 10.46 m DBS, total Fe concentrations decreased dramatically compared to the Upper Zone and Zone 1; the total extracted is consistent with XRF results. At the shallower depth (9.45 to 9.70 m DBS), siderite increased from 2,612 to 7,105 mg/kg as a function of depth, suggesting a reduced condition. Fe sulfide mineral coatings (amorphous and crystalline) declined from 28 to 8% (Figure 6.3) with pyrite contributions making up approximately 10%. Amorphous

Fe sulfide mineral coatings initially increased at shallower depths in this zone (9.45 to 9.60 m DBS), but then sharply declined to 317 mg/kg from 9.60 to 9.75 m DBS. Fe sulfide mineral coatings were detected by XRD analyses as well (Hua et al., 2020). The Fe(III) (oxyhydr)oxide minerals (15%) and Fe(II/III) mineral coatings (50%) dominated (Figure 4) at shallower depth (9.45 to 9.60 m DBS). From 9.60 to 9.75 m DBS, the proportion of Fe(III) (oxyhydr)oxide dropped to 2% given the more reduced environment where Fe(II/III) contributions increased to 69%. Approximately midway into Zone 2 (DBS: 9.75 – 10.06 m), total Fe concentrations in the sediments decreased; Fe mineral coating contributions are consistent (Figure 6.2). Deeper in Zone 2 (DBS: 10.06 – 10.36 m), total Fe concentrations declined from 36,611 to 11,911 mg/kg, and given that Fe(III) (oxyhydr)oxide contributions dropped by two orders of magnitude, a highly reduced environment is observed. However, Fe(II) minerals were detected at relatively low concentrations and the dominant Fe mineral coating is Fe(II/III) magnetite. Overall, Zone 2 is reduced and magnetite is the dominant reactive Fe mineral coating throughout the RTZ.

The variability in Fe species in Zone 3 between 14.63 and 15.24 m DBS was dramatic (Figure 6.2). Ion exchangeable Fe^{2+} ranged from 119 to 724 mg/kg (Figure 6.1), making up 0.2 to 14% of the total extracted Fe concentration, respectively (Figure 6.3). Generally, ion exchangeable contributions are found to be less than 2% of total Fe concentrations in sediment (Emmerson et al., 2000; Flyhammar, 1998). Zone 3 is located at the interface of the D-Aquifer and D-E Clay, where clay lenses weakly adsorb Fe^{2+} . Total Fe concentrations increased at shallower depths (DBS: 14.63 – 14.78 m) and then declined from 14.78 to 14.94 m (DBS); Fe(III) (oxyhydr)oxide decreased from 1,885 to 102 mg/kg, suggesting potentially a more reduced environment with increasing depth given that Fe (II/III) mineral magnetite also increased from 651 to 23,905 mg/kg

(Figure 6.2) and then sharply decreased by an order of magnitude. Two trends were revealed: magnetite and siderite contributions increased from 28 to 85% and 1 to 10% of total Fe, respectively. Midway through Zone 3 (DBS: 14.94 – 15.04 m), Fe(III) (oxyhydr)oxide increased two orders of magnitude from 102 to 36,900 mg/kg where siderite (<3%), magnetite (<3%), and Fe(III) (oxyhydr)oxide (<20%) were found with XRD (Hua et al., 2020). This increase attributed to Fe(III) is consistent with total Fe concentrations using XRF analyses over this 0.1 m sample interval. The proportion of siderite, amorphous Fe mineral coatings, and magnetite fell to less than 15%, while pyrite increased from below detection limit to approximately 20% of the total mineral coatings. The presence of sulfate-reducing bacteria at this depth helps to explain its presence (Figure 5.4). At greater depth in Zone 3 (DBS: 15.04 – 15.24 m) where the dominant Fe mineral coatings shifted to siderite and magnetite, Fe(III) (oxyhydr)oxide minerals decreased, which is consistent with XRD analyses (Hua et al., 2020). Pyrite decreased as well by over an order of magnitude where increasing contributions of amorphous Fe mineral coatings and siderite were observed. Overall, reduced Fe mineral coatings dominated deeper in Zone 3, which is consistent with a reduced environment.

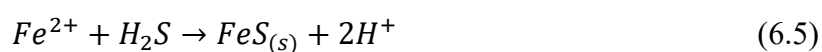
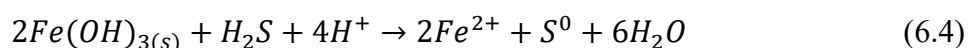
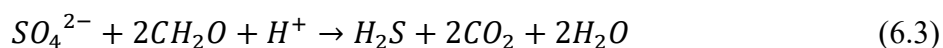
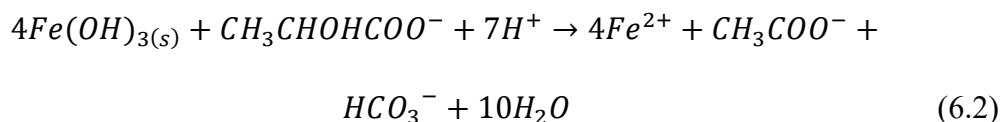
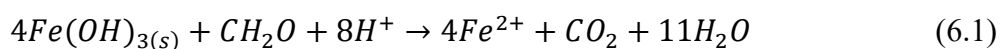
6.2 Potential Fe Cycling with Abundant Bacteria

In our previous study (Yin et al., 2021), 16S rRNA gene sequencing revealed five abundant Operational Taxonomic Units (OTUs), which matched up to the genera *Stenotrophomonas*, *Desulfosporosinus*, *Geobacter*, *Acidovorax*, and *Methylobacterium* (Figure 5.4). These bacteria are important in Fe cycling in the four RTZs. *Stenotrophomonas*, a facultative anaerobic bacteria, reduces Fe(III) to Fe(II) (Ivanov et al., 2005). Biogenic Fe(II) has been found with *S. maltophilia* BK in broad ranges, for example, in sludges of water treatment plant, (Ivanov et al., 2005) on roots of bean plant grown in alkaline soil (Valencia-Cantero et al., 2007), in sediments in acid mine

drainage (Gao et al., 2019), and on the surface of magnetite nanoparticles used to treat ciprofloxacin (Yang et al., 2017). In our core sediments, *Stenotrophomonas* was the most abundant genera in the shallower Upper Zone. As a facultative bacteria, *Stenotrophomonas* has a greater tolerance to O₂ (possibly from the surface) compared to other anaerobic bacteria. In the Upper Zone where Fe(III) (oxyhydr)oxides decreased with depth, *Stenotrophomonas* bacteria contributes to Fe(III) reduction.

The sulfate-reducing bacteria *Desulfosporosinus* is found under anaerobic conditions and is responsible for precipitation of amorphous Fe sulfide mackinawite, pyrite, and greigite (Bertel et al., 2012a). In sediments with elevated Fe and S concentrations, such as in Zone 1 and portions of the Upper Zone and Zone 3, sulfate and Fe(III) (oxyhydr)oxides are two abundant and important terminal electron accepters. The reduction of Fe(III) (oxyhydr)oxides follows two pathways: one is enzymatic reduction by Fe(III)-reducing bacteria (i.e., *Geobacter*, *Stenotrophomonas*) (Equations 6.1 and 6.2) (Dos Santos Afonso and Stumm, 1992; Zachara et al., 2002), and another is the redox reaction with biogenic H₂S generated by sulfate-reducing bacteria (Equations 6.3 and 6.4) (Bao et al., 2018; Ikkert et al., 2013; Poulton et al., 2004). Fe-reducing bacteria can reduce Fe(III) (oxyhydr)oxides and promote mineral dissolution (Jones et al., 2006). On the other hand, these Fe²⁺ sulfide minerals precipitate directly in the presence of *Desulfosporosinus* sp. strain *GBSRB4.2* to form metastable mackinawite (Equation 6.5) initially, which then undergoes transformation to greigite at neutral pH (Bertel et al., 2012a). In zero-valent-Fe-based permeable reactive barriers, mackinawite and green rust were dominant minerals where *Desulfosporosinus* was abundant (Kumar et al., 2016). Moreover, reduction of Fe(III) (oxyhydr)oxides (Equations 1 to 4) is an H⁺-consuming reaction. The pH in Zone 1, from the previous

screening results (Yin et al., 2021), increased from 6 to 7.5 (Figure 5.4), suggesting this biogeochemical cycling process can be attributed to this shift:



Geobacter, an anaerobic iron-reducing bacteria, commonly exists in sediment systems. Biogenic Fe(II) produced by *Geobacter* is found to play an important role in contaminant degradation: aromatics (i.e., benzene (Zhang et al., 2014), nitrobenzene (Lu et al., 2021)), heavy metals (i.e., Hg-methylation (Kerin et al., 2006)), and radioactive waste (e.g., reduced U(VI) to U(IV) (Wilkins et al., 2006)). As the most abundant bacteria in Zone 2, magnetite was the dominant mineral throughout the RTZ. These results are consistent with the transformation of lepidocrocite and ferrihydrite to magnetite in the presence of *Geobacter* under anaerobic conditions (Mejia et al., 2016).

Acidovorax is a nitrate-reducing bacteria and has been reported in Fe(II) enzymatic reactions where, for example, mackinawite was oxidized to Fe(III) (oxyhydr)oxides (Lu et al., 2020), and green rust formed in Fe(II) oxidation with *Acidovorax sp.* strain BoFeN1 (Klueglein and Kappler, 2013; Pantke et al., 2012). In our sediment core, *Acidovorax* was observed in the Upper Zone and was abundant elsewhere in the core outside of the RTZs. *Methylobacterium* is another bacteria found in the core that commonly utilizes methane as the energy source. A unique *Methylobacterium*-like thermo-acidophilic bacteria was isolated in Yellowstone National Park and worked in oxidizing Fe in an Fe-rich environment (Johnson et al.,

2003). However, the relationship between *Methylobacterium* and Fe minerals is unclear due to limited studies.

6.3 Summary

The speciation and concentration of reactive Fe mineral coatings in four RTZs of a sediment core were evaluated with a modified six-step SE process. In the shallowest RTZ, the Upper Zone, a sandy aquifer with clay lenses, amorphous and crystalline Fe sulfide mineral coatings exceeded 40% of the total Fe present. Dominant iron sulfide minerals included amorphous mackinawite and greigite along with thermodynamically stable pyrite, consistent with a reduced environment. In the presence of sulfate-reducing bacteria, Zone 1 displayed the highest concentrations of Fe and, specifically, crystalline Fe sulfide pyrite when compared to the other three RTZs studied. The abundance of Fe sulfide mineral coatings in the Upper Zone and Zone 1 is expected to support abiotic attenuation of chlorinated solvents present at the site. In Zone 2, where mineral coatings include pyrite, siderite, magnetite, and Fe (oxyhydr)oxides, the Fe(III) (oxyhydr)oxides transformed to the reduced-Fe mineral coatings, magnetite and siderite, in the presence of the Fe-reducing bacteria *Geobacter*. In Zone 2, magnetite was the dominant Fe mineral coating. In Zone 3, the transformation between Fe(III) and Fe(II/III) is significant, indicating a reduced environment. Reactive iron mineral coatings in RTZs supports evidence of (a)biotic processes in natural attenuation.

CHAPTER 7

KINETICS STUDIES OF 1,4-DICHLOROBENZENE, TETRACHLOROETHYLENE, AND TRICHLOROETHYLENE WITH NATURAL REACTIVE IRON MINERALS FROM REDOX TRANSITION ZONES

In this section, reaction kinetics for the degradation of 1,4-DCB, PCE, and TCE are evaluated in bench studies with reactive iron minerals in sediments from redox transition zones. It is the first study to the best of our knowledge that focuses on evaluating the abiotic dechlorination processes of chlorinated ethene and benzene in the presence of natural Fe(II) mineral nano-coatings. This study helps in resolving the contributions of different forms of reactive Fe mineral coatings in abiotic attenuation.

7.1 COC Degradation with RTZ Sediments

7.1.1 Reductive 1,4-DCB Dechlorination

1,4-DCB is one of the most frequently detected COC from the area around the core. The experiment was conducted with one blank group, two standard mineral groups (control), and four sediments groups from RTZs under anaerobic conditions with simulated groundwater. In the blank group (Figure 7.1A), the concentration of 1,4-DCB was constant, indicating no loss due to volatilization or adsorption on the glass vial over 97 hours. There was no reduction of 1,4-DCB in the standards pyrite and siderite, suggesting dechlorination processes could not be observed during the period of the study (Figure 7.1A).

In the four sediment groups, approximately 20% reduction of 1,4-DCB was measured over 140 h with the presence of CB and BZ adsorbed in the sediment (Figure 7.2). These two byproducts are reported in other abiotic/biotic studies under anaerobic conditions as well (Lawrence, 2006; Liang et al., 2011) (Figure 7.3). Two chlorides on

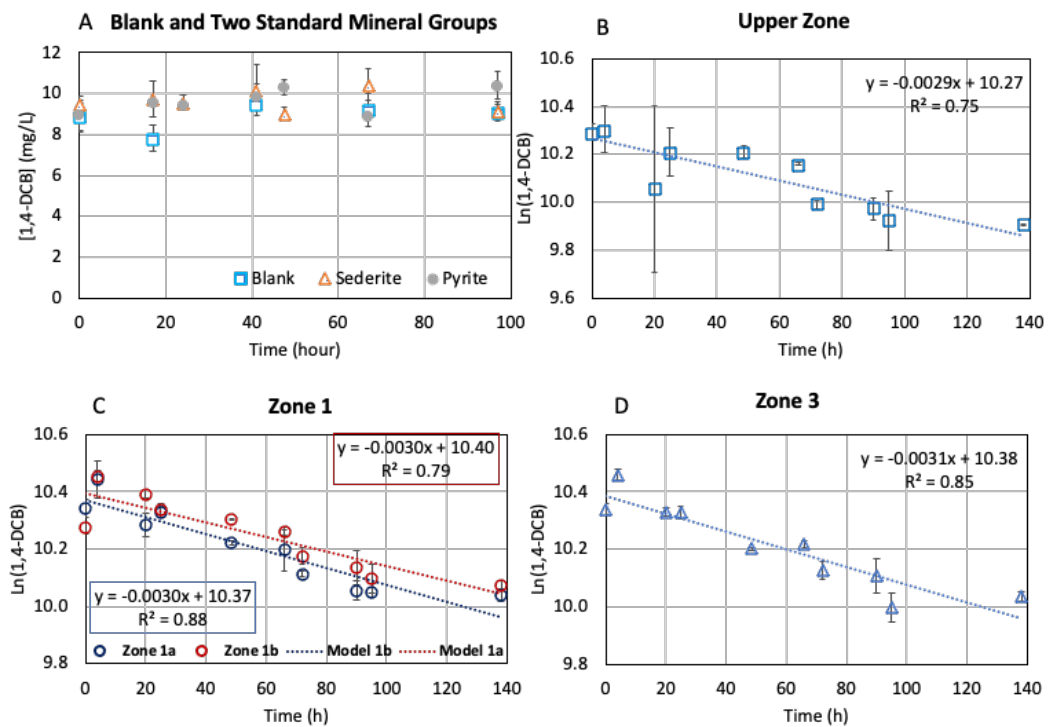


Figure 7.1 Reductive dechlorination of 1,4-DCB studies. (A) The concentration of 1,4-DCB (mg/L) versus time in blank, standard pyrite, and standard siderite were consistent over 97 h. Natural logarithm values of 1,4-DCB concentration versus time of Upper Zone, Zone 1 and Zone 3 were plotted in (B), (C), and (D), respectively. The natural logarithm value of 1,4-DCB and time is linear with a good fit.

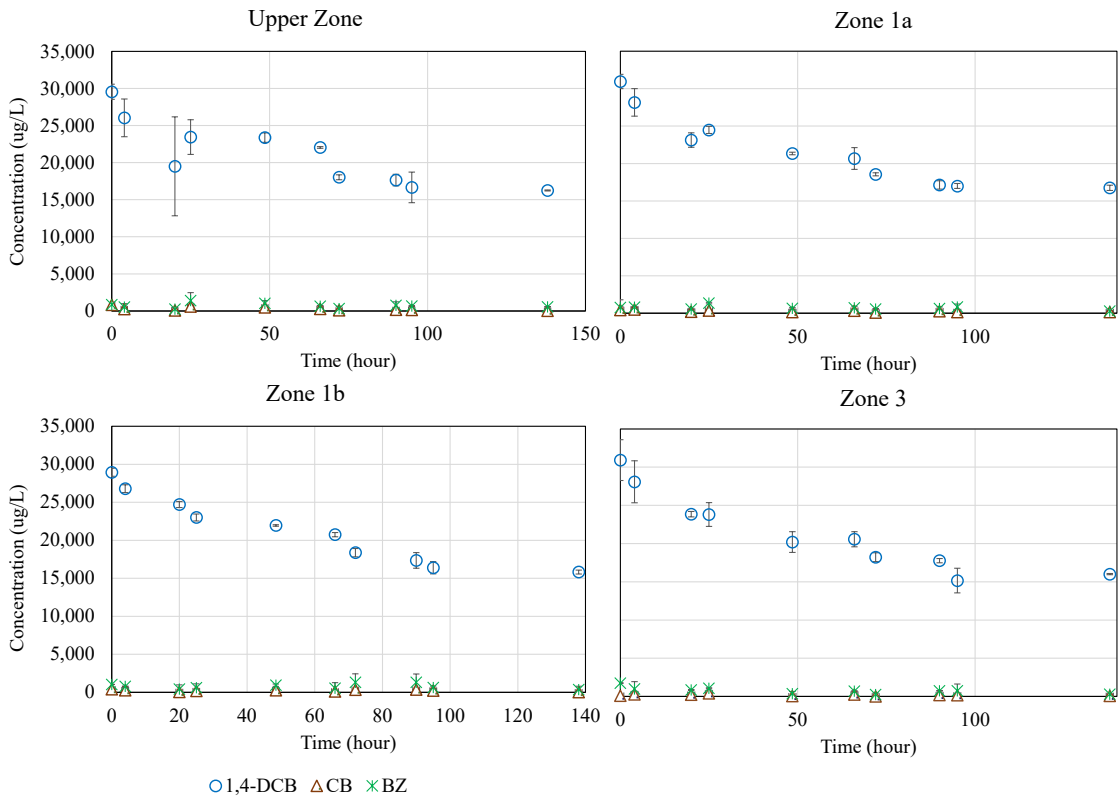


Figure 7.2 Concentration of 1,4-DCB, CB, and BZ in four sediment groups versus time (h).

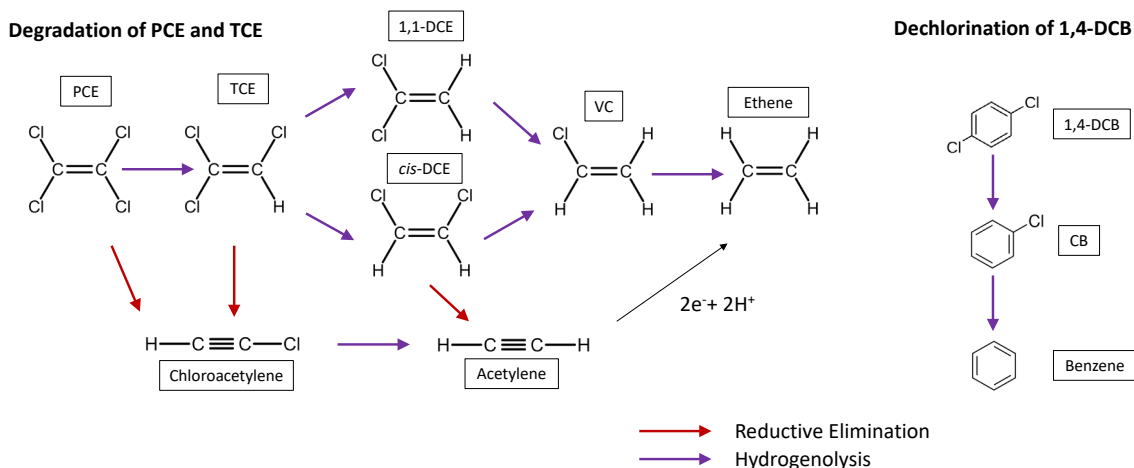


Figure 7.3 Potential reductive dehalogenation for 1,4-DCB (right) and chlorinated ethenes (left) with reactive iron mineral coatings was summarized.^{1,2} These abiotic processes included reductive elimination and hydrogenolysis.

Source: 1. Degradation pathway and byproducts for chlorinated ethenes are summarized from He, Y.; Wilson, J.; Su, C.; Wilkin, R., *Review of Abiotic Degradation of Chlorinated Solvents by Reactive Iron Minerals in Aquifers. Groundwater Monitoring & Remediation* 2015, 35, (3), 57-75.

2. Dechlorination mechanisms for 1,4-DCB are cited from Liang, X.; Howlett, M. R.; Nelson, J. L.; Grant, G.; Dworatzek, S.; Lacrampe-Couloume, G.; Zinder, S. H.; Edwards, E. A.; Sherwood Lollar, B., *Pathway-Dependent Isotope Fractionation during Aerobic and Anaerobic Degradation of Monochlorobenzene and 1,2,4-Trichlorobenzene. Environmental Science & Technology* 2011, 45, (19), 8321-8327.

the benzene ring were sequentially replaced with hydrogen through hydrogenolysis. Because there was no addition of nutrients or carbon to the system, microbial activities are expected to be negligible with the abiotic dechlorination process being dominant. However, accumulation of CB and BZ were not observed as a function of time in aqueous and sediment, which is a challenge in the mass recovery. One possible reason is the low concentrations of byproducts. During the experiment, it is difficult to measure low concentrations of CB and BZ in the aqueous phase given adsorption to the sediment. In the last step for VOC extraction from sediment, loss may be due to opening the cap to remove water and add methanol. Another reason for the poor VOC recovery is that methanol cannot entirely extract the COC from sediments with clay lenses (DiStefano et al., 2016). Although the loss of byproduct is difficult for resolving mass recovery, the presence of CB and BZ in the system is strong evidence for abiotic dechlorination of 1,4-DCB.

The pseudo-first order model (Figure 7.1B, 7.1C, and 7.1D) reveals good fits for the sediment groups. Following Eq. (4.1), the pseudo-first order reaction rate constants (k_1') for the four sediments groups are in the same order of magnitude, ranging from $(2.54 \pm 0.46) \times 10^{-3}$ to $(3.10 \pm 0.45) \times 10^{-3} \text{ h}^{-1}$; the greatest reaction rate constant was observed in the Zone 3 sediment (Table 7.1). The time to achieve 90% dehalogenation of 1,4-DCB in the RTZ sediments ranged from 31 to 37 days.

7.1.2 Potential Mechanism for 1,4-DCB Dechlorination

In control groups, during the time period of the studies, pyrite and siderite did not reduce 1,4-DCB. Reducing chlorinated benzene in contact with crystalline Fe minerals, such as crystalline ZVI (Plagentz et al., 2006) and microscale iron particles ($<10 \mu\text{m}$, $0.9 \text{ m}^2 \text{ g}^{-1}$) (Xu and Zhang, 2000), has been found to be negligible as well over the

Table 7.1 Observed Pseudo-First-Order Reaction Rate Constants of 1,4-DCB, PCE, and TCE with Sediment Samples Collected from Four Redox Transition Zones.

	Groups	k' (h^{-1})	R^2	50% Degradation (h)	90% Degradation (d)
1,4- DCB	Upper Zone	$(2.92 \pm 0.60) \times 10^{-3}$	0.75	237	32
	Zone 1a	$(2.97 \pm 0.39) \times 10^{-3}$	0.88	233	32
	Zone 1b	$(2.54 \pm 0.46) \times 10^{-3}$	0.79	272	37
	Zone 3	$(3.10 \pm 0.45) \times 10^{-3}$	0.85	223	31
PCE	Upper Zone	$(3.66 \pm 0.26) \times 10^{-3}$	0.97	189	26
	Zone 1a	$(4.00 \pm 0.74) \times 10^{-3}$	0.85	174	24
	Zone 1b	$(2.72 \pm 0.35) \times 10^{-3}$	0.92	254	35
	Zone 3	$(2.68 \pm 0.59) \times 10^{-3}$	0.80	258	35
TCE	Upper Zone	$(2.45 \pm 0.41) \times 10^{-3}$	0.88	283	39
	Zone 1a	$(3.63 \pm 0.18) \times 10^{-3}$	0.98	191	26
	Zone 1b	$(2.89 \pm 0.45) \times 10^{-3}$	0.89	240	33
	Zone 3	$(2.67 \pm 0.28) \times 10^{-3}$	0.95	260	36

period of the study. In our work, we hypothesize that Fe(II) nano-mineral coatings in the sediment have significant activity. Although abiotic reductive dechlorination of 1,4-DCB has not been investigated with iron sulfide minerals, dechlorination of long-chain chlorinated benzenes has been studied (Elliott et al., 2009; Liu et al., 2003; Nie et al., 2013; Xu and Zhang, 2000). Fe bimetallic system attracted attention in chlorinated solvents degradation that utilized the galvanic cell to enhance the dechlorination processes (Quiton et al., 2021). Coupling Fe with less reactive metals (e.g., Pb, Ag, and Cu) catalyzed the efficiency of Fe oxidation, which enhanced the process of dechlorination (Cao et al., 2011; Wan et al., 2010; Xu and Zhang, 2000). Xu and Zhang (2000) studied the dechlorination of γ -HCH by ZVI/Ag particles where 1,4-DCB was one of the byproducts. They reported the concentration of γ -HCH was reduced to below the detection after four days. Increasing the Ag concentration on the Fe surface promoted Fe oxidation and extended dechlorination (Xu and Zhang, 2000). Similarly, micro-size Fe particles with metallic Pb was found to dechlorinate γ -HCH following pseudo-first-order kinetics with the greatest rate constant of 0.0321 min^{-1} at 85°C (Nie et al., 2013). Interestingly, when Fe is coupled with more active metals, such as Al, the metal with higher hydrogen over-potential serves as the electron source, was reported to prevent precipitation of Fe corrosion products (e.g., magnetite and hematite (Fe_2O_3)) (Nidheesh et al., 2018). These ZVI/Al bimetallic systems have not been studied with chlorinated benzenes; however, these systems have been reported to exhibit high reactivity in the degradation of CCl_4 (Chen et al., 2008), dichlorodiphenyltrichloroethane (DDT) (Ulucan-Altuntas and Debik, 2020), and TCE (Xu et al., 2018). In another study, Liu et al. (2003) reported synthesized amorphous Fe sulfide mackinawite contributed to γ -HCH dechlorination following a pseudo-first order model. At a circumneutral pH, the half-life for γ -HCH dechlorination was

approximately 55 days. Nanoscale ZVI (nZVI) (Elliott et al., 2009) was observed to be responsible for the γ -HCH degradation under anaerobic conditions without maintaining a constant pH. The reaction was best fit with a pseudo-first order decay and a rate constant of 0.138 h^{-1} ($[\text{nZVI}] = 0.39 \text{ g L}^{-1}$), where the pH increased from 6.31 to 9.07 in 30 hours. As a result, Fe minerals with large surface areas and coupled with other metals on the mineral surface may improve dechlorination.

In our analysis (Yin et al., 2021), the composition of the sediment was screened with XRF; metals included Cu (below detection limit to 30 mg kg^{-1}) and Al (between 1,928 to $40,380 \text{ mg kg}^{-1}$) in the RTZ sediment; however, not in their metallic form. The abundant Al minerals in the sediment may occur with the Fe minerals and serve as potential electron donors for Fe^{3+} to Fe^{2+} cycling in the groundwater. Based on the Fe(II) coating mineralogy and morphology (Hua et al., 2020), the nano-coatings present as framboidal greigite and pyrite (Figure 1) revealed spherical framboids of greigite, cubic structures of mackinawite, flaky aggregates of mackinawite, and subpentagonal pyrrhotite. These distinct Fe(II) mineral morphologies were abundant in the Upper Zone and Zone 1 sediments. Given the nature of sediment and its inherent variability and heterogeneity, we would expect differences in the pseudo-first-order rate constants between our study others such as the nZVI study of Elliot et al. (2009) Importantly, the Fe(II) mineral nano-coatings from the RTZs sediment contributed to 1,4-DCB dechlorination through abiotic reductive processes.

7.1.3 Reductive PCE and TCE Dechlorination

Under anaerobic conditions, experiments on PCE and TCE degradation were conducted with a blank, control, and four RTZ sediments. The recovery in the TCE and PCE studies was greater than 85% in the blank group, indicating no observable loss over the

course of the study (Figures 7.4 and 7.5). For PCE, degradation was observed in both control groups as well as the four sediment groups and followed pseudo-first order reaction kinetics (Figures 7.4 and 7.6). The reaction rate constants (k_1') for PCE degradation with the pure minerals (control groups) are consistent with the constants found with the RTZ sediments given the errors. 90% removal of PCE ranged from 26 to 35 days (Table 7.1). The reaction rate constants observed in our studies are greater than constants reported earlier for Fe-rich sediment systems (Appendix E). In the Fe(II)-clay mineral (smectite) system (Entwistle et al., 2019; Nzungu et al., 2001), PCE degradation was poorly fit pseudo-first-order reaction. 17% PCE degradation was observed after 100 days with Fe(II) amended- smectite clay mineral (Entwistle et al., 2019). PCE was transformed to acetylene, butane, ethene, and/or propane in an Fe-rich clay sediment under anaerobic conditions (Schaefer et al., 2017); the greatest reaction rate revealed 90% degradation at 55°C requiring theoretically over 400 years. On the other hand, the reaction rate constants in our study are consistent with work with an Fe-rich microbial system (Chen et al., 2021; Ma and Wu, 2008). PCE degradation in a ZVI-microbial system followed pseudo-first order kinetics with 90 % removal achieved at 12 days (Ma and Wu, 2008). Magnetic nanoparticles enriched with bacteria degraded PCE with rate constants ranging from $(2.38 \pm 0.29) \times 10^{-3}$ to $(1.34 \pm 0.05) \times 10^{-2} \text{ h}^{-1}$ where 90% removal requires 7 to 40 days (Chen et al., 2021). However, compared to our work, PCE degradation has been reported to be more rapid with other pure mineral systems as well as with bacteria. For example, green rust (with bone char) rapidly removed 99% PCE over 48 h (reaction rate: $0.22 \pm 0.02 \text{ h}^{-1}$) (Ai et al., 2019). Suarez and Rifai (1999) reviewed 138 studies on PCE biodegradation and found the median decay coefficient rate was 0.04 h^{-1} (90% removal in 3 days).

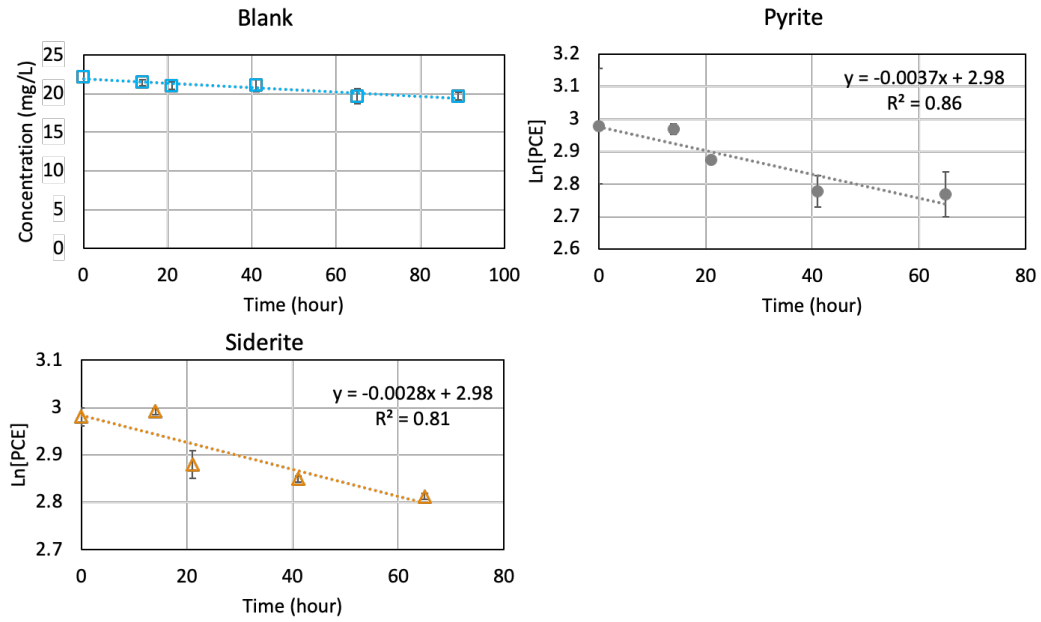


Figure 7.4 Reductive dechlorination of PCE in blank and control groups. No reduction of PCE was observed in the blank group as a function of time (h). The degradation of PCE in standard pyrite and siderite groups followed pseudo-first-order reaction.

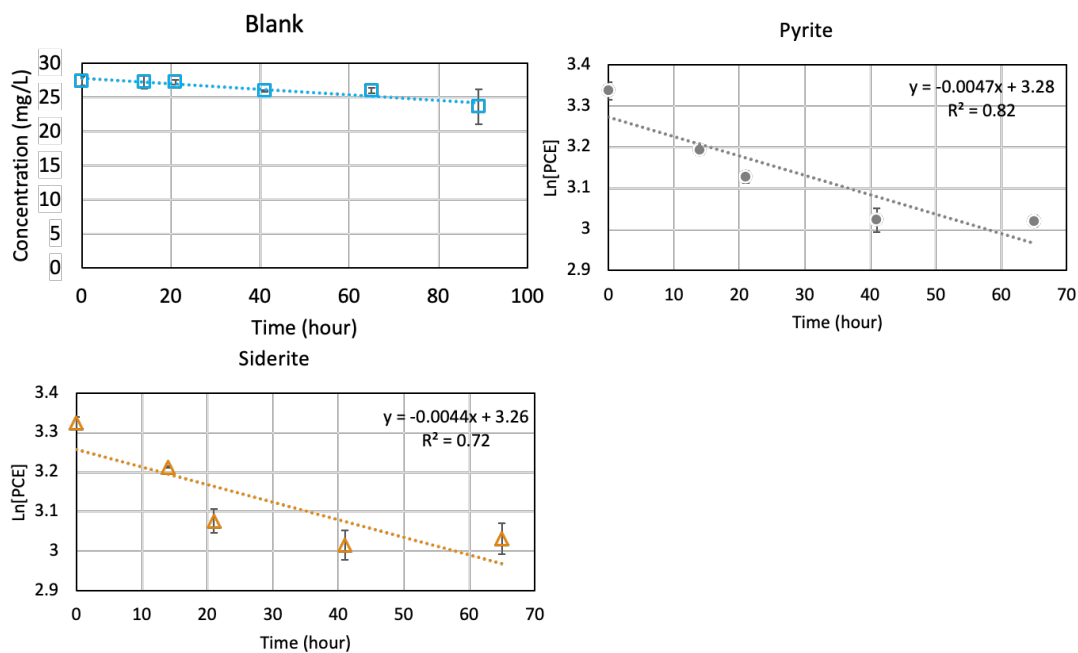


Figure 7.5 Reductive dechlorination of TCE in blank and control groups. No reduction of PCE was observed in the blank group as a function of time (h). The degradation of TCE in standard pyrite and siderite groups followed pseudo-first-order reaction.

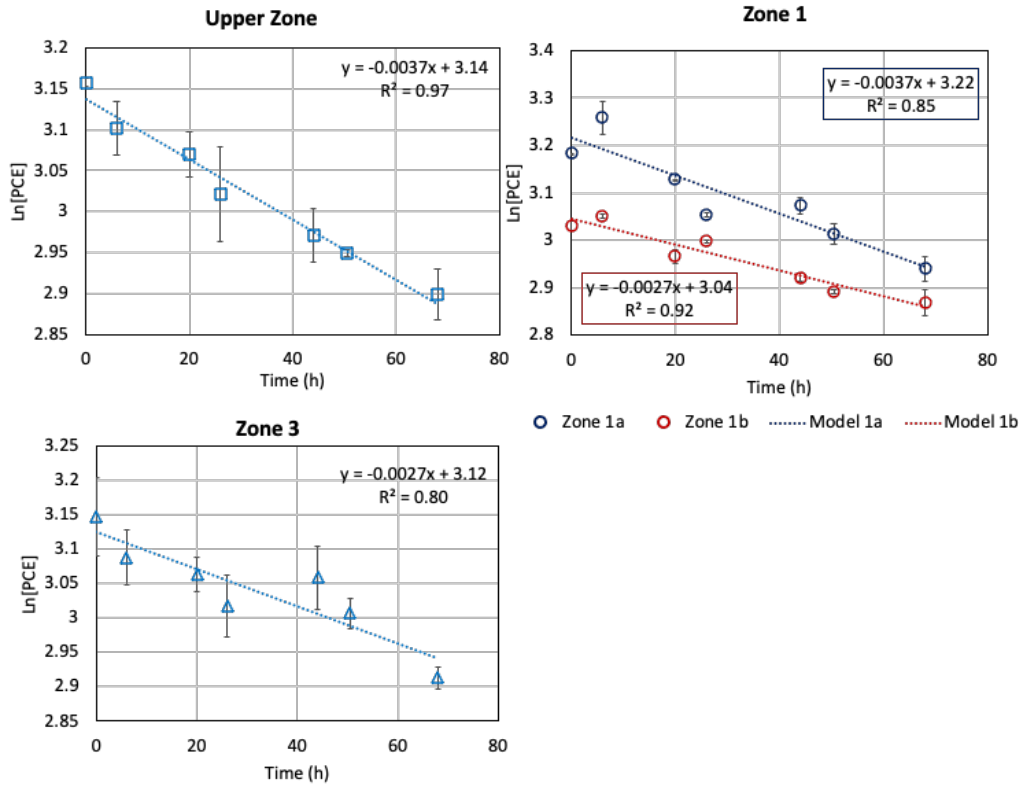


Figure 7.6 Natural logarithm values of PCE concentration versus time (h) of Upper Zone, Zone 1 and Zone 3 sediments were plotted. Regression results show the degradation fit pseudo-first-order reaction.

In the TCE study, a pseudo-first-order model for both control and RTZ sediments resulted in good fits (Figures 7.5 and 7.7). The rate constants for the four sediment groups studied were the same order of magnitude: resulting in 90% degradation over 39 days. RTZ sediments revealed efficient TCE degradation rates compared to other studies with sediments (Schaefer et al., 2017; Schaefer et al., 2015) (Appendix F). For example, Schaefer et al. (2017) reported TCE degradation at $18.8 \pm 0.04 \times 10^{-8} \text{ h}^{-1}$ (20°C) (90% degradation requiring more than 1,000 years) with anaerobic sediment in the presence of Fe clay minerals. In rock matrix with Fe(II) sulfide minerals (Schaefer et al., 2013), TCE was reduced to acetylene, ethene, and/or ethane with the reaction rate constants ranging from 3.0×10^{-6} to $1.5 \times 10^{-4} \text{ h}^{-1}$ (90% degradation requiring 2 to 90 years). In a clayey soil system with nano-ZVI (Katsenovich and Miralles-Wilhelm, 2009), TCE degradation was observed to require 10 to 46 days to achieve 90% degradation. However, TCE degradation was observed at a greater rate in a pure mineral system, where Weerasooriya and Dharmasena (2001) found TCE transformation to acetylene (90% removal time is 2 days; pH at 8.9) with pyrite ($2 \text{ m}^2 \text{ L}^{-1}$). Similarly, pyrite reduced TCE to acetylene, cis-DCE, 1,1-DCE at pH 7.2 with a 90% removal in 15 days (He et al., 2010).

Byproducts were not detected at measurable concentrations in the sample headspace, which is most likely due to the low concentrations present in the gas phase (Appendix G). During the experiment, it is difficult to measure low concentrations of the byproducts given adsorption to the sediment. In the last step for VOC extraction from sediment, loss may be due to opening the cap for removing water and adding methanol. Furthermore, methanol cannot entirely extract VOC from the clay matrix (DiStefano et al., 2016). To overcome these limitations, possible experiment modifications may include

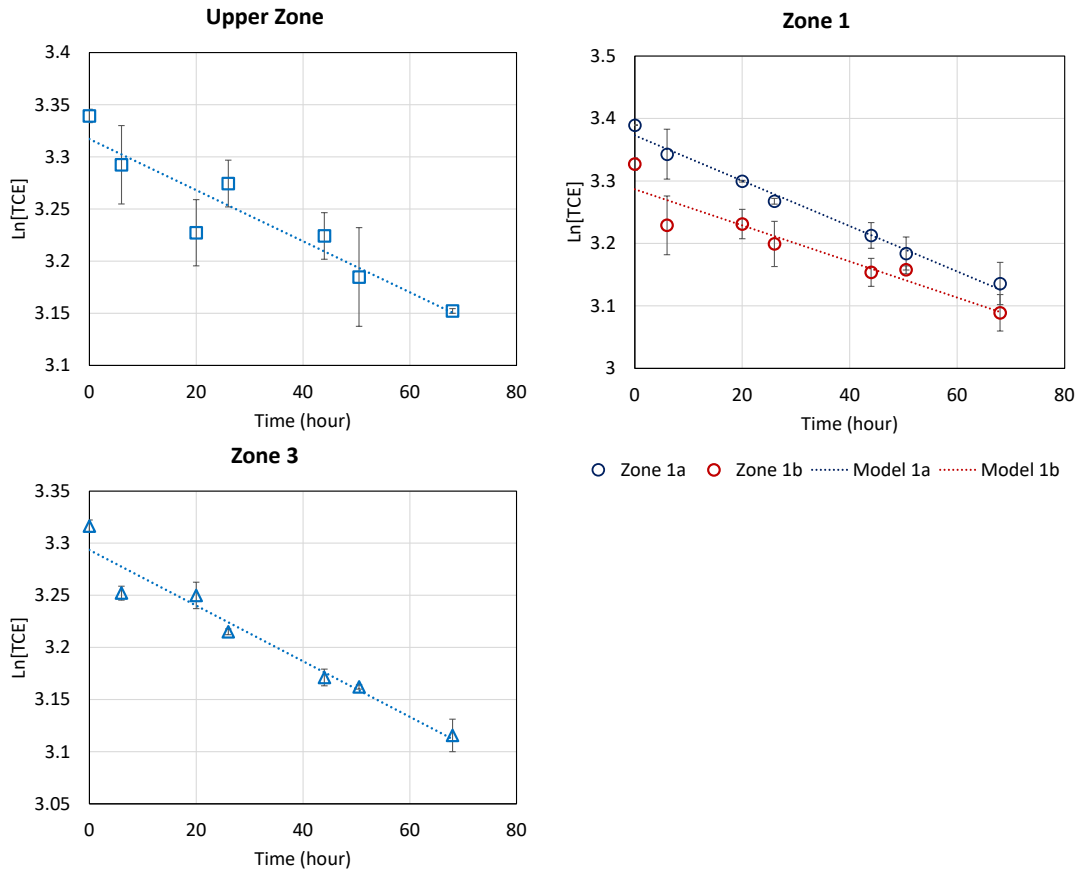


Figure 7.7 Natural logarithm values of TCE concentration versus time (h) of four sediments from RTZs, were plotted and fit the pseudo-first-order model.

increasing the initial concentration significantly and extending the reaction time to capture byproducts in the headspace.

Degradation of PCE and TCE follows four potential pathways: reductive elimination, hydrogenolysis, dehydrohalogenation, and hydrolysis (He et al., 2015). For chlorinated ethenes, degradation through abiotic reductive processes have been proposed to follow two pathways (Figure 7.3): 1) reductive elimination (De Wildeman and Verstraete, 2003), and 2) hydrogenolysis (Holliger et al., 2003). In PCE and TCE degradation, reductive β -elimination was attributed as the primary pathway with Fe(II) minerals where acetylene as the dominant byproduct (Choi et al., 2010; Lee and Batchelor, 2002a; Liang et al., 2007b) and ethene was the final product formed by acetylene hydrogenation (Liang et al., 2007b; Liang et al., 2009). Hydrogenolysis pathway generally is found in biotic processes for PCE and TCE dechlorination. In some studies (Butler and Hayes, 2001; Jeong et al., 2007; Lee and Batchelor, 2002a; Liang et al., 2007b), the detection of cis-DCE and 1,1-DCE, indicates that hydrogenolysis is a minor pathway.

7.2 Reaction Rate Constant of Dominant Fe(II) Mineral Nano-Coatings

The dominant Fe(II) mineral coatings, mackinawite, pyrite, siderite, and magnetite, were detected in the RTZ sediments. Second-order reaction rate constants (normalized by mass) were calculated using Eq. (4.3) (Tables 7.2). Generally, the rate constants of iron-mediated reactions were reported based on the mineral surface area (He et al., 2015). However, given the complexity of sediment and the nano-coatings that form, surface area measurements could not be determined (Kocur et al., 2020; Schaefer et al., 2021). Fe sulfides (mackinawite, pyrite), siderite, magnetite from the RTZ sediments, were responsible for

Table 7.2 Calculated Second-Order Reaction Rate Constants (Based on Mass) of 1,4-DCB, PCE, and TCE Studies

Groups		Second order reaction rate constant (L/(g·h))			
		Mackinawite	Pyrite	Siderite	Magnetite
1,4-DCB	Sediment	$(1.24 \pm 0.47) \times 10^{-3}$	$(1.73 \pm 0.16) \times 10^{-3}$	$(1.89 \pm 0.46) \times 10^{-4}$	$(1.79 \pm 0.70) \times 10^{-4}$
	Pure Mineral	-	$(1.43 \pm 0.34) \times 10^{-3}$	$(6.00 \pm 1.65) \times 10^{-4}$	-
PCE	Sediment	$(3.28 \pm 4.08) \times 10^{-4}$	$(6.20 \pm 2.03) \times 10^{-4}$	$(1.25 \pm 0.86) \times 10^{-4}$	$(1.10 \pm 0.21) \times 10^{-3}$
	Pure Mineral	-	$(1.83 \pm 0.49) \times 10^{-3}$	$(0.93 \pm 0.35) \times 10^{-3}$	-
TCE	Sediment	$(4.97 \pm 39.3) \times 10^{-5}$	$(1.19 \pm 0.21) \times 10^{-3}$	$(1.41 \pm 0.51) \times 10^{-4}$	$(4.32 \pm 1.39) \times 10^{-4}$

COCs degradation (Table 7.2). Rate constants for amorphous mackinawite and pyrite were of the same order of magnitude as that for magnetite; these constants were an order of magnitude greater than siderite's. Fe(II) sulfide minerals are the dominant electron donors in the dechlorination processes, suggesting Fe(II) and sulfide contribute to COC transformation. Mackinawite (FeS), a metastable Fe sulfide mineral, has been found to be effective in PCE and TCE degradation under anoxic conditions. In the abiotic process, acetylene is the primary product through β -elimination. TCE was detected in PCE degradation with mackinawite via hydrogenolysis. Because of the large surface area, amorphous mackinawite transformed chlorinated ethenes much faster than other crystalline Fe(II) forms (e.g., pyrite, magnetite). Synthesized nanocrystalline mackinawite has been reported to exhibit $103 \text{ m}^2 \text{ g}^{-1}$ based on transmission electron microscopy analysis (Jeong et al., 2008). Specific surface area of pyrite ranges from 0.03 to $1.1 \text{ m}^2 \text{ g}^{-1}$ using the Brunauer, Emmett, Teller (BET) method (Beckingham et al., 2016). Although there is no universally accepted method for estimating the average mineral reactive surface area, the specific surface area of mackinawite is distinctly greater than pyrite based on particle size and morphology. Reductive dechlorination rate constants for PCE were reported as $2.74 \times 10^{-2} \text{ L m}^{-2} \text{ d}^{-1}$ with mackinawite and $1.97 \times 10^{-5} \text{ L m}^{-2} \text{ d}^{-1}$ with pyrite (Lee and Batchelor, 2002a). In our study, mackinawite and pyrite were no different given the error, $(3.28 \pm 4.08) \times 10^{-4} \text{ L g}^{-1} \text{ h}^{-1}$ and $(6.20 \pm 2.03) \times 10^{-4} \text{ L g}^{-1} \text{ h}^{-1}$, respectively. Framboidal pyrite is a nanocrystalline structure with a large mineral surface area. Xing et al. (2021) reported synthesized framboidal pyrite ranged from 1.83 to $2.54 \text{ m}^2 \text{ g}^{-1}$ using FESEM analysis. This area was greater than the micrometer size pyrite surfaces. However, the uncertainty of the

BET method increases when measuring minerals with a large surface area (Wolfe et al., 2007). The specific surface area of framboidal pyrite may therefore be underestimated.

Pyrite is the most thermodynamically stable Fe sulfide mineral (Rickard and Luther, 2007). As a significant electron donor and acceptor in the biogeochemical system, pyrite is involved in redox cycling for abiotic and biotic processes. In the subsurface, pyrite formation can occur abiotically with mackinawite and H₂S, resulting in H₂ (Rickard and Luther, 1997). Under sulfate-reducing conditions, pyrite was generated by microbial reduction with, for example, *Desulfosporosinus* (Bertel et al., 2012a). Pyrite degraded chlorinated ethenes via reduction elimination and hydrogenolysis (He et al., 2015). The main product in degradation of PCE, TCE, c-DCE, and VC was acetylene via β -elimination (Lee and Batchelor, 2002a). Contaminants are expected to adsorb at the reactive sites of pyrite supporting reductive dechlorination. The adsorption processes enhance attenuation. On the other hand, pyrite has been found to undergo Fenton reactions with O₂ under oxic conditions forming a potent oxidant hydroxyl radical. The hydroxyl radical oxidizes TCE and 1,4-DCB in the pyrite-O₂ system (Pham and Chihiro, 2019). Pyrite plays a prominent role in chlorinated ethenes degradation through redox pathways as well. As a result, the highly reactive Fe(II) sulfides such as pyrite are important in attenuation of chlorinated solvents.

Fe minerals with less reactivity, siderite and magnetite, are part of the Fe cycling in contaminated systems. Fe(II) carbonate siderite may be one of the dominant Fe(II) minerals when sulfides in an iron-reducing environment are not present (Yin et al., 2021). The reaction rate constants for siderite in RTZ sediment degraded PCE and TCE were $(1.25 \pm 0.86) \times 10^{-4}$ L g⁻¹ h⁻¹ and $(1.41 \pm 0.51) \times 10^{-4}$ L g⁻¹ h⁻¹, respectively. Reductive TCE

degradation was reported with siderite ore at $1.2 \pm 0.32 \times 10^{-7} \text{ L g}^{-1} \text{ h}^{-1}$ with acetylene as the byproduct (Schaefer et al., 2021). Magnetite is ubiquitous in the subsurface and degrades the chlorinated ethenes where 1,1-DCE and cis-DCE may be transformed to acetylene with VC generation (Ferrey et al., 2004). Lee and Batchelor (2002a) found that magnetite degraded PCE with a reaction rate constant of $0.84 \times 10^{-6} \text{ L m}^{-2} \text{ d}^{-1}$, resulting in a half-life of 608 days. They also found that the magnetite surface area is 2.1 times greater than pyrite. The high sorption capacity depleted contaminant mobility and contributed to attenuation.

7.3 Summary

This study contributes to our understanding of abiotic degradation processes with reactive Fe mineral coatings. Specifically, we reported on results from applying RTZ sediments in the dehalogenation of 1,4-DCB, PCE, and TCE. Degradation of chlorinated benzene is a challenge through abiotic reduction due to its stable benzene ring. In our study, dechlorination of 1,4-DCB was observed with reactive Fe(II) mineral nano-coatings, including amorphous mackinawite and framboidal pyrite (observed by XRD and FESEM in the previous work (Hua et al., 2020)). Chlorobenzene and benzene were detected in the system as byproducts, which is consistent with isotope work (Liang et al., 2011). The strong reductive capacity of reactive Fe mineral coatings may be due to 1) nanoscale particles providing large surface areas, and 2) mineral impurities that may support catalysis and the 1,4-DCB transformation reaction. The four reactive Fe mineral coatings were found support abiotic degradation for 1,4-DCB, PCE, and TCE dechlorination. The trend for mineral coating reactivity followed: nanocrystal Fe(II) sulfide mineral coatings > magnetite > siderite.

CHAPTER 8

CONCLUSIONS AND FUTURE WORK

This research reports on methodology and results from identifying redox transition zones in a subsurface systems where reactive Fe minerals participate in biogeochemical cycling. The methodology in this study demonstrates a systematic approach for identifying these redox transition zones. An 18.3-meter anoxic core was collected where the redox condition of the sediment was preserved during the collection, transportation, sampling, and analytical processes. Screening analyses of a total of 225 (5.08 cm) subsamples provided a continuous biogeochemical profile as a function of depth for sediment ORP, sediment pH, Fe and S concentrations, TVOC concentration in the headspace, and abundant bacterial genera. Over the core's length, gradients were observed in sediment pH, sediment ORP, and Fe and S concentrations. The Fe and S gradients correlated with the presence of Fe and S reducing bacteria, such as *Desulfosporosinus* and *Geobacter*. Using complementary geochemical and microbial data, five redox transition zones were delineated. This study contributes to establishing a protocol for systematically characterizing sediment core samples where the redox condition has been preserved. The profiles of parameters analyzed provide evidence of redox gradients and the potential impact on iron mineral coating transformations where transition zones are identified. Using this approach, redox transition zones were delineated. Subsequent analyses can then be carried on surface coating speciation and mineralogy (Han et al., 2020). This study also provides insight into potential cycling of Fe and S.

To better understand the reactive Fe mineral distribution in RTZ sediment, a semi-quantitative analysis was conducted with a six-step sequential extraction. Based on the concentration of different forms of Fe mineral coating, potential Fe cycling with abundant bacteria become clearer and more significant. In the presence of sulfate-reducing bacteria, Zone 1 displayed the highest concentrations of Fe and, specifically, crystalline Fe sulfide pyrite when compared to the other three RTZs studied. The abundance of Fe sulfide mineral coatings in the Upper Zone and Zone 1 is expected to support abiotic attenuation of chlorinated solvents present at the site. In Zone 2, where mineral coatings include pyrite, siderite, magnetite, and Fe (oxyhydr)oxides, the Fe(III) (oxyhydr)oxides transformed to the reduced-Fe mineral coatings, magnetite and siderite, in the presence of the Fe-reducing bacteria *Geobacter*. In Zone 2, magnetite was the dominant Fe mineral coating.

SE is a traditional method for quantitative analysis of minerals in sediment; however, it has drawbacks that cannot be ignored. In extractions, it is difficult to distinguish mineral coatings with similar phases. Specifically, poorly crystalline Fe minerals that include mackinawite, greigite, and Fe(III) ferrihydrite are targeted with the same extraction (1 M NaAc pH 4.5). Additionally, while Fe mineral forms can be characterized and quantified, it is a challenge to profile mineral coatings in the sediment at a high resolution. The technique is also plagued with an uncertainty of 10 to 30% (Rodgers et al., 2015). Time studies were conducted to address the particle-size effect in the sediment core, which included silt, sand, and clay; the SE process was modified accordingly. Therefore, to identify and characterize RTZs for a site with contamination, SE is highly useful in resolving and quantifying Fe speciation and is an important complementary tool for the

higher resolution profiling that can be accomplished with other tools such as XRD and FESEM/EDX.

Batch studies were conducted to assess the contribution of these reactive Fe mineral coatings to attenuation of chlorinated solvents. Specifically, we reported on results from applying RTZ sediments in the dehalogenation of 1,4-DCB, PCE, and TCE. Degradation of chlorinated benzene is a challenge through abiotic reduction due to its stable benzene ring. In our study, dechlorination of 1,4-DCB was observed with reactive Fe(II) mineral nano-coatings, including amorphous mackinawite and framboidal pyrite (observed by XRD and FESEM in the previous work (Hua et al., 2020)). Chlorobenzene and benzene were detected in the system as byproducts and consistent with isotope work (Liang et al., 2011). The strong reductive capacity of reactive Fe mineral coating may be due to 1) nanoscale particles providing large surface areas and 2) mineral impurities that may support catalysis and the 1,4-DCB transformation reaction. The four reactive Fe mineral coatings were found to describe the abiotic degradation process for 1,4-DCB, PCE, and TCE dechlorination. The trend for mineral coating reactivity followed: nanocrystal Fe(II) sulfide mineral coatings > magnetite > siderite. In this study, we applied reaction kinetic models for the COC investigated with the RTZ sediment. Reductive dechlorination of 1,4-DCB, one of the dominant COCs at the site, has been observed through abiotic processes; this finding highlights the significant potential of reactive Fe mineral coatings in RTZs, contributing to natural attenuation.

In this research, RTZs were initially determined to correlate with geochemical and microbial analysis where attenuation is expected. Several minerals contribute to COC degradation, demonstrating the importance of reactive Fe mineral coatings and RTZs.

Important in this process is identifying these RTZs, evaluating Fe mineral contribution, and applying these models in MNA. Future work associated with this research may include studies focused on application of the data and modeling in natural attenuation processes. Furthermore, using machine learning tools to resolve potential processes and indicators of predicting RTZs would be highly beneficial to the remediation industry. In the complex RTZs system, abiotic and/or biotic pathways are important in contaminant attenuation. Column studies with hydrological data and spiking of COCs can simulate site conditions over a long-term period, which can help us to study contaminant fate and transport in RTZ systems. Furthermore, degradation pathways with isotope analysis would be helpful in resolving COC transformation in RTZs.

APPENDIX A
OVERVIEW OF GEOLOGY LOG

The summaries of soil logs depict observations from logging cores D14-SCS-1 to D14-SCS-25 totaling 27 cores, which were drilled to a depth of approximately 20 m below to surface. The logging procedure is summarized in the following:

1. Each 5 cm subsamples was collected each time with observations, a photograph, oxygen and photoionization detector recorded.
2. Soil from the core is collected in a glove box and screened for the presence of volatile organic compounds (VOCs) using a MiniRAE 3000 Photoionization Detector (PID). The PID has a detection range from 0.1-15,000 ppm. The unit of calibration is 10 to 2000 ppm with an error $\pm 3\%$ and an isobutylene standard gas.
3. Sample depth was skipped when no recovery was observed in the cores samples. Other sample's depth will be recorded continually.

Layer	O ₂ (ppm)	PID reading (ppm)	Color	General Matrix	Depth (ft.)		
B Aquifer	110	not detected	Light brown	Saturated to moist soil Coarse sand with few gravels and cobbles	10'10"		
	180		Dark brown				
	350						
	3		Light brown with reddish brown				
No Recovery					18'		
B-C Clay	17	First 2" has PID readings	Brown and orange brown	Less moisture Mainly clay with medium sand	19'6"		
	10	First 2" has PID readings	Black grey coated rocks	Silty clay with fine sand and cobbles			
C Aquifer		14	0.3	Black grey and yellowish brown	Coarse sand and gravels with silty mud	26'	
	not detected		Coarse sand with gravels and cobbles				
	No Recovery						27'8"
	1	not detected	Brown and yellowish brown	Coarse sand with gravels and cobbles			
14							
					30'		

Layer	O ₂ (ppm)	PID Reading (ppm)	Color	General Matrix	Depth (ft.)
C Aquifer	3	First 6" have PID reading	Dark yellowish brown	Dry soil Fine to coarse sand and few gravels	30'10"
		Not detected		Loose saturated soil Fine to coarse sand	
D Aquifer	190	0.2	Dominant light yellowish brown ; light orange and greenish grey	11" groundwater and 1" soil	38' 38'6" 43'2" 45' 46' 47'8" 48'2"
	14	Not detected		Loose moist to saturated soil Fine to medium sand	
	No Recovery				
	8	Not detected	Dominant light yellowish brown ; light orange and greenish grey lenses	Loose moist to saturated soil Fine to medium sand	
	100				
	130				
	170	0.2	Moderate to greyish yellow and white grey	sticky dense clay and very loose medium sand mix	
	5	0.3		Dry soil, very dense clay and very loose sand	
	No Recovery				
	200	2.4	Reddish brown	5" groundwater and 6" medium sand	
D-E Clay	100	0.3	Yellowish brown and reddish brown	Very dense clay and loose sand	

Layer	O ₂ (ppm)	PID reading (ppm)	Color	General Matrix	Depth (ft.)
D-E Clay			and white grey		50'
4' No Recovery					
D Aquifer	19.6	3.1		groundwater	56'2"
D-E Clay	60	0.2	Orange brown and white grey	Dry loose soil Medium sand with clay	
No Recovery					58'
D-E Clay	30	0.4	Dominant white grey with light to reddish brown lenses	Saturated dense to soft clay with few sand	59'8"
		1.1		Saturated soil Dense sticky clay and very few loose sand	63'
	88	0.3	Reddish brown and white grey	Dry and dense clay	64'2"
100	66'				

APPENDIX B

ROTATION SPEED AND REYNOLDS NUMBER

Gardner and Tatterson (1992) studied the relationship between rotation speed and mixing.

The Reynolds number (Re) is calculated as follows (Driessen et al., 2020):

$$Re = \frac{\rho \omega d^2}{\mu} \quad (B.1)$$

where ρ is solution density (kg/m^3), ω is angular velocity (s^{-1}), d is the maximum inner diameter of tube (m), μ is dynamic fluid viscosity ($\text{Pa}\cdot\text{s}$). Assuming at 20°C , the dynamic fluid viscosity for the sample solution is $1.002 \times 10^{-3} \text{ Pa}\cdot\text{s}$ (Kestin et al., 1978) and the density for the solution is $1 \times 10^3 \text{ kg/m}^3$. The maximum inner diameter of tube is 0.027m . The shaker can be set at a stable rotation speed (such as 100, 200, or 300 revolutions per minute), converted to angular velocity in radium per second (Equation B.2).

$$\text{angular velocity (s}^{-1}\text{)} = \text{rotation speed (rpm)} \times \frac{1}{60} \times 2\pi \quad (B.2)$$

For rotation speed 100 rpm, the angular velocity is:

$$n = 100 \times \frac{1}{60} \times 2\pi = 10.47 \text{ s}^{-1} \quad (B.3)$$

And the density, kinematic viscosity, and maximum inner diameter of tube are:

$$\rho = 1 \times 10^3 \text{ kg/m}^3 \quad (B.4)$$

$$d = 27\text{mm} = 0.027\text{m} \quad (B.5)$$

$$\mu = 1.002 \times 10^{-3} \text{ Pa}\cdot\text{s} \quad (B.6)$$

As a result, the Reynolds number for 100 rpm is:

$$Re = \frac{\rho n d^2}{\mu} = \frac{1 \times 10^3 \text{ kg/m}^3 \times 1.67 \text{ s}^{-1} \times (0.027\text{m})^2}{8.9 \times 10^{-4} \text{ Pa}\cdot\text{s}} = 7630 \quad (B.7)$$

The Reynolds numbers were considered for the shakers full range of speeds (Table B1).

Table B.1 The Relationship between Rotation Speed and Reynolds Number

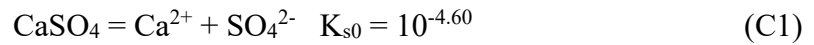
Rotation speed (rpm)	100	200	300	400	500
Angular velocity (s^{-1})	10.47	20.93	31.4	41.87	52.33
Re	7,630	15,260	22,890	30,520	38,151

If the Reynolds number is between 500 to 1000, mixing is dominated by large toroidal vortices. With the increasing of Reynolds number, the mixing transforms from toroidal vortex mixing to transitional mixing. Typically, $Re > 10,000$ is required for fully turbulent conditions, and a transition region between laminar and turbulent flow occurs over the range $10 < Re < 10,000$ (Green and Perry, 2008). In this study, the sample will continuously shake at 400 rpm under turbulent flow conditions.

APPENDIX C

PRECIPITATION OF GYPSUM

The solubility equilibrium of gypsum:



Compared the actual ion activity product (IAP) with K_{s0} , the state of saturation is defined as following:

$\text{IAP} > K_{s0}$ (oversaturated)

$\text{IAP} = K_{s0}$ (saturated)

$\text{IAP} < K_{s0}$ (undersaturated)

Calcium and sulfate concentration were collected from groundwater data. The calculation results are presented in Table C1. According to the results, saturation of gypsum was expected at DBS:10.07-10.22 (m), 11.44-11.59 (m), and 13.58-13.73(m).

Table C.1 Saturated CaSO₄ Calculation

DBS (m)	Sulfate (M)	Calcium(M)	IAP	IAP-K _{s0}	Saturated condition
1.84-1.99	8.13E-05	0.001583	1.29E-07	-2.49E-05	undersaturated
3.21-3.36	1.88E-05	0.00156	2.93E-08	-2.50E-05	undersaturated
5.35-5.50	0.003458	0.004225	1.46E-05	-1.04E-05	undersaturated
6.41-6.57	0.005	0.001753	8.76E-06	-1.62E-05	undersaturated
7.17-7.33	0.001792	0.001923	3.44E-06	-2.16E-05	undersaturated
8.24-8.39	0.00176	0.001613	2.84E-06	-2.22E-05	undersaturated
9.00-9.16	0.001521	0.001435	2.18E-06	-2.28E-05	undersaturated
10.07-10.22	0.006656	0.0053	3.53E-05	1.03E-05	oversaturated
11.44-11.59	0.006688	0.00525	3.51E-05	1.01E-05	oversaturated
12.51-12.66	0.004948	0.003725	1.84E-05	-6.57E-06	undersaturated
13.58-13.73	0.005885	0.00435	2.56E-05	6.02E-07	oversaturated
14.64-14.79	0.005146	0.001975	1.02E-05	-1.48E-05	undersaturated
18.30-18.45	0.001083	0.000458	4.96E-07	-2.45E-05	undersaturated

APPENDIX D

ABUNDANT OPERATIONAL TAXONOMIC UNIT IN ANOXIC CORE

Each 5.08 cm subsample was examined macroscopically and 0.2 g of material was retrieved (Iker et al., 2013) from each subsample so that visibly differing material within the subsample was represented. This material was then mixed and processed for DNA isolation using a PowerSoil™ (Qiagen) kit with five one-minute agitation cycles using a MiniBead beater 96 (Biospec Products). DNA from each 5.08 cm subsample was used for microbial community analysis by amplification of the 16S rRNA gene V4 region using primers described previously (Raju et al., 2018), sequencing DNA from each subsample to a read depth of greater than 50,000 reads. Sequences were then error corrected, and subject to de novo operational taxonomic unit (OTU) clustering, relative abundance of each OTU was determined in each sample, and genus level taxonomic assignment of the OTUs generated using the Mothur analysis pipeline (Kozich et al., 2013).

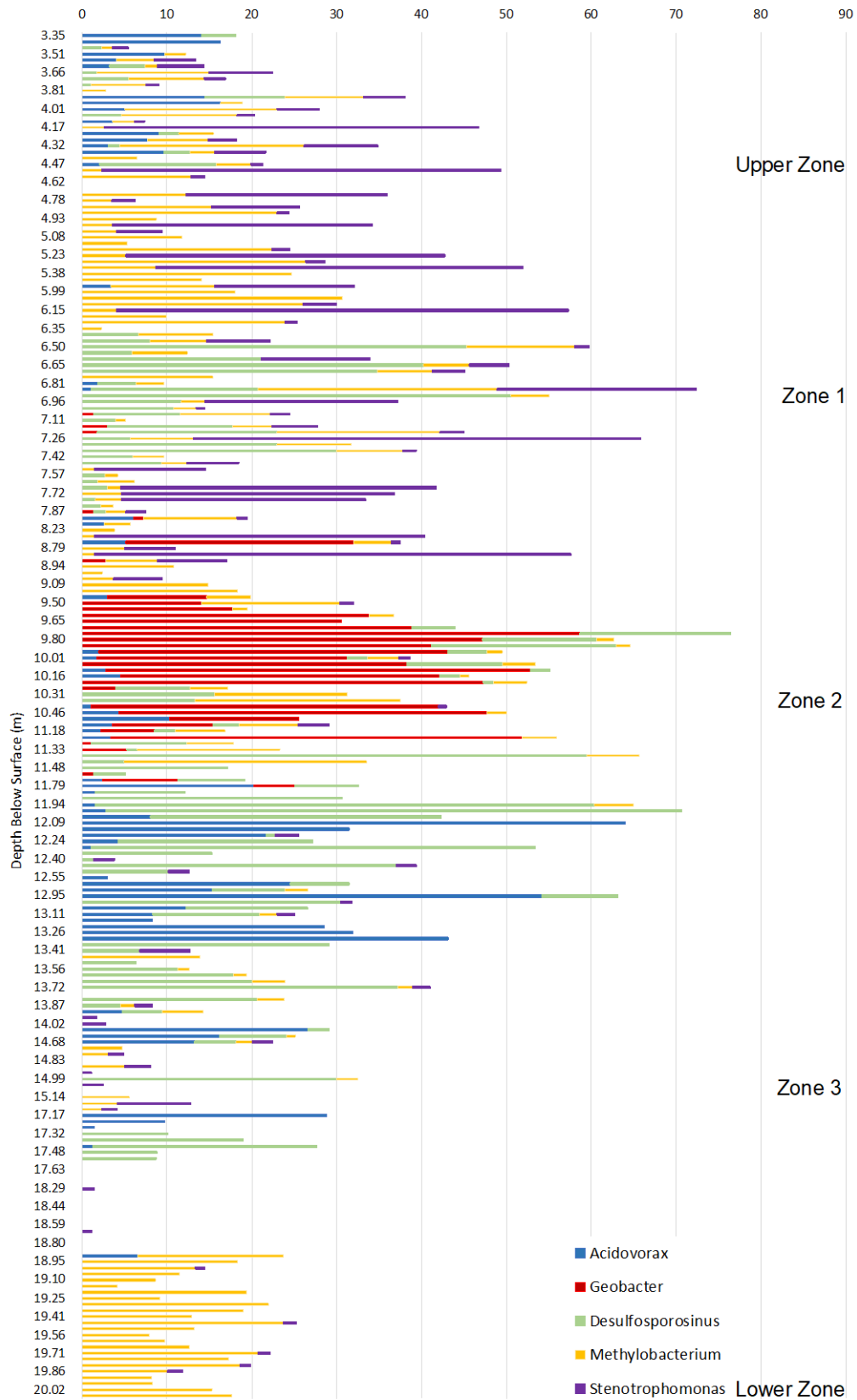


Figure D.1 The abundant operational taxonomic unit (OTUs) matched to the genera *Stenotrophomonas*, *Desulfosporosinus*, *Geobacter*, *Acidovorax*, and *Methylobacterium*. The proportions of abundant bacteria (%) are revealed as a function of depth below surface (m) and highlighted the area of five redox transition zones.

APPENDIX E

RATE CONSTANTS OF REDUCTIVE PCE DECHLORINATION BY FE MINERALS RELATED SYSTEMS

Rate constants of reductive PCE degradation in current study and other Fe related system was list in the following table.

Electron Source	Condition	Reaction Rate	90% Removal Time	Reference
Green rust with bone char	pH 8; 3.2 g/L GR mixed with 0.15 g/L bone char	$0.22 \pm 0.02 \text{ h}^{-1}$	20 h	(Ai et al., 2019)
Fe(II) amendment clay minerals	-	-	17% degradation over 100 days	(Entwistle et al., 2019)
Dithionite-treated clay minerals (ferruginous smectite)	-	Poorly fit the pseudo-first order reaction	-	(Nzengung et al., 2001)
Anaerobic sediment with Fe clay minerals	-	$134 \pm 7.8 \times 10^{-7} \text{ day}^{-1}$, 55°C; $10 \pm 1.8 \times 10^{-7} \text{ day}^{-1}$, 35°C; $8.3 \pm 0.82 \times 10^{-7} \text{ day}^{-1}$, 20°C;	470 y	(Schaefer et al., 2017)
ZVI with microbial community	-	0.187 day^{-1} ($7.8 \times 10^{-3} \text{ h}^{-1}$)	12 d	(Ma and Wu, 2008)
Enriched perchloroethene dechlorinator via magnetic nanoparticles	-	$0.057 \pm 0.007 \text{ day}^{-1}$ to $0.322 \pm 0.013 \text{ day}^{-1}$	7 to 40 d	(Chen et al., 2021)
RTZ sediments with reactive Fe mineral coatings	pH 9	$(2.68 \pm 0.59) \times 10^{-3}$ to $(4.00 \pm 0.74) \times 10^{-3} \text{ h}^{-1}$	24 to 35 d	Current study

APPENDIX F

RATE CONSTANTS OF REDUCTIVE TCE DECHLORINATION BY FE MINERALS RELATED SYSTEMS

Rate constants of reductive PCE degradation in current study and other Fe related system was list in the following table.

Electron Source	Condition	Reaction Rate	90% Removal Time	Reference
Anaerobic sediment with Fe clay minerals	-	$45 \pm 0.10 \times 10^{-7}$ day ⁻¹ , 20°C;	1402 y	(Schaefer et al., 2017)
Rock matrix with pyrite	-	3.0×10^{-6} to 1.5×10^{-4} h ⁻¹	2 to 88 y	(Schaefer et al., 2013)
Nano-ZVI in clayey soil	-	0.05-0.24 day ⁻¹	10 to 46 d	(Katsenovich and Miralles-Wilhelm, 2009)
Pyrite (impure)	pH 8, 2 m ² /L	pH 4.3, 0.182/day, pH 5.3, 0.182/day, pH 6.4, 0.293/day, pH 7.4, 0.552/day, pH 8.2, 0.866/day, pH 8.9, 1.21/day	2 to 12 d	(Weerasooriya and Dharmasena, 2001)
Mackinawite	pH 8.3, 10 g/L FeS, 0.1 M tris buffer	$(5.09 \pm 0.24) \times 10^{-2}$ day ⁻¹	45 d	(Jeong and Hayes, 2007)
Pyrite (not freeze dried)	pH 7.2, 18 g/L FeS	$(1.52 \pm 0.10) \times 10^{-1}$ day ⁻¹	15 d	(He et al., 2010)
Pyrite	pH 8, 84 g/L 2340 m ² /L	1.60 ± 0.02 day ⁻¹	2 d	(Lee and Batchelor, 2002a)
RTZ sediments with reactive Fe mineral coatings	pH 9	$(2.45 \pm 0.41) \times 10^{-3}$ to $(3.63 \pm 0.18) \times 10^{-3}$ h ⁻¹	26 to 39 d	Current study

APPENDIX G

THE CALCUALTED CONCENTRATIONS OF ACETYLENE IN THE TETRACHLOROETHYLENE AND TRICHLOROETHYLENE STUDIES

Reduction elimination is the primary abiotic pathway for chlorinated ethenes, with acetylene as the major byproduct. However, to demonstrate why this byproduct was not detected in the studies conducted, the assumption used in both the tetrachloroethylene (PCE) and trichloroethylene (TCE) experiments is that acetylene is the only byproduct in each 40 mL reactor. The concentrations of acetylene (in gas, liquid, and solid phases) from PCE and TCE studies reveal that over the time intervals, the acetylene concentration produced based on the decrease of the target COC would have been (Tables G.1 and G.2) less than 0.8 mg L^{-1} which is below the (GC-MS) detection limit.

Table G.1 The Concentrations of Observed Tetrachloroethylene (PCE) and Calculated Acetylene in the Gas, Liquid, and Solid Phases of the 40 mL Reactor with Upper Zone Sediment

Time (h)		0	6	20	26	44	50.5	68
Observed TCE (mg/L)	Gas	8.52	7.22	6.96	6.60	6.23	6.07	5.73
	Liquid	15.00	12.70	12.26	11.63	10.96	10.70	10.10
	Solid	0.00	1.56	1.56	1.56	1.56	1.56	1.56
	Total	23.52	21.48	20.78	19.79	18.75	18.33	17.39
Calculated Acetylene (mg/L)	Gas		0.37	0.44	0.54	0.64	0.69	0.78
	Liquid		0.21	0.25	0.31	0.37	0.39	0.44
	Solid		0.00	0.00	0.00	0.00	0.00	0.00
	Total		0.32	0.44	0.59	0.76	0.83	0.98

Table G.2 The Concentrations of Observed Trichloroethylene (TCE) and Calculated Acetylene in the Gas, Liquid, and Solid Phases of the 40 mL Reactor with Upper Zone Sediment

Time (h)		0	6	20	26	44	50.5	68
Observed TCE (mg/L)	Gas	10.21	8.64	8.02	8.46	7.99	7.65	7.36
	Liquid	17.98	15.21	14.12	14.89	14.07	13.46	12.95
	Solid		2.05	2.05	2.05	2.05	2.05	2.05
	Total	28.20	25.90	24.19	25.41	24.11	23.16	22.36
Calculated Acetylene (mg/L)	Gas		0.32	0.44	0.35	0.45	0.52	0.57
	Liquid		0.56	0.78	0.62	0.79	0.91	1.01
	Solid		0.41	0.41	0.41	0.41	0.41	0.41
	Total		0.46	0.80	0.56	0.82	1.01	1.17

APPENDIX H

THE DATA OF SCREENING ANALYSES BY A SUITE OF COMPLEMENTARY TOOLS

Four geochemical analyses were conducted to screen the 18 m anoxic core. The analyses included sediment pH, sediment oxidation/reduction potential (ORP), element concentrations of sediment, and total volatile organic compounds in the sediment headspace. The data of these analyses as a function of depth below the surface and elevation (m) were list in Table 1 and 2.

Table H.1 The Concentrations of Dominant Elements (mg kg⁻¹) in the Sediment Determined by X-Ray Fluorescence Spectrometer as a Function of Depth (m)

DBS (m)	Elevation (m)	Fe	Si	Al	Ti	S	P
3.35	-1.83	27,428	111,882	11,489	8,304	584	7,151
3.40	-1.88	24,478	116,517	11,592	6,431	491	8,216
3.45	-1.93	26,774	97,454	13,852	5,352	656	5,070
3.51	-1.98	24,826	93,265	15,231	4,549	2,430	5,801
3.56	-2.03	30,988	80,602	12,006	3,431	528	5,419
3.61	-2.08	22,214	100,262	13,196	4,378	3,832	5,125
3.66	-2.13	20,725	121,798	16,805	3,632	2,830	5,225
3.71	-2.18	24,059	131,083	20,983	4,551	2,585	5,406
3.76	-2.24	20,411	116,869	15,623	4,076	3,962	5,097
3.81	-2.29	18,253	110,258	13,763	3,687	2,395	5,248
3.91	-2.39	19,722	129,662	17,979	4,164	3,150	5,194
3.96	-2.44	16,828	108,026	14,009	3,409	994	5,146
4.01	-2.49	17,380	104,521	12,075	3,270	2,790	5,142
4.06	-2.54	17,925	108,928	14,195	2,870	2,809	5,195
4.11	-2.59	13,831	75,916	9,348	2,383	2,046	5,100
4.17	-2.64	17,675	103,725	11,639	3,380	6,933	5,012
4.22	-2.69	22,709	86,958	16,869	2,831	894	5,113
4.27	-2.74	17,912	68,987	11,431	2,598	906	4,829
4.32	-2.79	16,849	62,310	10,341	2,277	2,083	4,852
4.37	-2.84	17,788	69,202	10,912	2,856	2,136	4,704
4.42	-2.90	19,191	68,133	13,225	2,266	815	5,102
4.47	-2.95	20,309	75,296	14,536	2,544	2,107	4,939
4.52	-3.00	16,666	63,842	10,176	1,862	3,837	4,757
4.57	-3.05	19,433	57,120	11,169	2,326	4,630	4,832
4.62	-3.10	18,733	56,796	10,537	2,209	2,801	4,868
4.67	-3.15	22,947	57,820	11,803	2,577	679	4,785
4.72	-3.20	25,054	61,147	13,321	2,672	766	5,039
4.78	-3.25	28,034	63,475	12,823	2,925	965	4,881
4.83	-3.30	28,975	78,780	15,148	3,192	685	5,202
4.88	-3.35	31,836	76,918	16,244	2,455	558	5,125
4.93	-3.40	34,395	73,021	13,259	2,230	461	4,903
4.98	-3.45	36,175	54,994	11,866	1,859	525	4,891
5.03	-3.51	39,182	61,373	13,725	2,234	635	4,946
5.08	-3.56	46,295	70,311	12,676	1,912	690	5,263
5.13	-3.61	42,472	66,906	14,628	2,150	753	5,171
5.18	-3.66	29,268	72,364	12,610	2,199	576	5,290
5.23	-3.71	27,699	57,634	10,653	1,892	529	4,650
5.28	-3.76	48,167	78,368	13,733	2,510	489	4,674
5.33	-3.81	23,056	79,290	11,389	4,039	459	5,658

DBS (m)	Elevation (m)	Fe	Si	Al	Ti	S	P
5.38	-3.86	36,752	90,391	13,145	3,112	435	4,759
5.44	-3.91	26,975	52,728	8,925	2,412	487	4,628
5.49	-3.96	24,527	63,907	10,268	2,324	514	4,811
5.99	-4.47	36,491	108,786	15,987	4,293	513	5,415
6.05	-4.52	22,788	68,790	9,656	4,574	459	6,050
6.10	-4.57	24,565	77,643	12,182	4,755	506	5,973
6.15	-4.62	22,645	78,774	13,382	4,691	532	5,907
6.20	-4.67	23,082	75,701	12,472	4,682	516	5,837
6.25	-4.72	24,281	71,884	11,972	4,670	495	5,500
6.35	-4.83	25,014	100,827	17,256	4,532	490	4,374
6.40	-4.88	25,559	78,477	10,720	3,341	2,628	4,072
6.45	-4.93	33,704	93,884	15,116	4,031	3,143	4,806
6.50	-4.98	34,976	90,478	13,410	3,539	3,555	4,953
6.55	-5.03	32,726	92,792	14,342	3,699	3,601	5,059
6.60	-5.08	33,723	92,246	16,953	4,261	3,174	4,688
6.65	-5.13	38,702	75,503	13,986	3,738	4,482	4,661
6.71	-5.18	43,680	77,295	14,804	3,704	4,937	4,863
6.76	-5.23	53,959	62,781	11,774	2,888	5,906	4,874
6.81	-5.28	52,428	47,737	7,344	2,681	4,018	4,449
6.86	-5.33	45,300	83,716	14,355	3,389	3,583	4,305
6.91	-5.38	29,421	91,890	9,239	3,048	983	5,455
6.96	-5.44	34,515	85,963	13,382	3,969	671	7,539
7.01	-5.49	50,793	61,453	9,808	3,427	983	4,828
7.06	-5.54	49,317	70,628	9,840	3,134	963	5,215
7.11	-5.59	45,688	66,292	10,356	2,381	2,254	5,328
7.16	-5.64	65,623	69,391	12,713	2,709	3,892	4,776
7.21	-5.69	48,867	86,936	10,428	3,896	754	7,527
7.26	-5.74	44,061	97,861	11,033	5,345	709	10,963
7.32	-5.79	47,644	55,379	8,995	4,800	2,550	5,021
7.37	-5.84	52,344	52,126	8,748	4,493	7,670	4,921
7.42	-5.89	37,092	88,579	10,865	3,002	10,627	5,560
7.47	-5.94	44,470	73,244	9,536	3,174	9,393	6,489
7.52	-5.99	43,640	90,861	11,168	4,062	5,187	5,891
7.57	-6.05	44,169	78,437	9,100	3,124	3,958	5,531
7.62	-6.10	27,734	79,357	6,677	1,716	10,856	5,177
7.67	-6.15	37,627	69,680	6,787	1,778	14,834	5,169
7.72	-6.20	39,940	53,943	7,348	2,022	14,340	5,351
7.77	-6.25	28,380	50,004	6,072	1,409	18,927	5,056
7.82	-6.30	43,770	59,456	7,479	1,882	16,578	5,940
7.87	-6.35	42,782	60,861	8,423	2,414	14,192	5,533
7.92	-6.40	40,374	55,921	8,924	2,993	12,611	5,330
8.48	-6.96	50,467	37,987	5,829	2,473	807	5,264

DBS (m)	Elevation (m)	Fe	Si	Al	Ti	S	P
8.23	-6.71	50,197	37,716	6,017	2,210	963	5,246
8.28	-6.76	41,465	43,317	6,404	1,956	1,231	5,488
8.74	-7.21	54,282	51,152	8,513	1,704	650	6,025
8.79	-7.26	63,720	31,685	5,682	1,266	479	5,179
8.84	-7.32	52,051	38,314	5,320	1,533	635	5,674
8.89	-7.37	38,340	57,591	5,592	1,258	608	6,098
8.94	-7.42	33,215	64,795	6,063	1,550	573	5,894
8.99	-7.47	28,294	53,571	5,330	1,745	524	5,291
9.04	-7.52	36,521	45,147	7,843	2,113	499	5,016
9.09	-7.57	37,627	46,612	7,576	1,837	528	5,196
9.14	-7.62	38,203	36,697	6,629	1,620	543	5,170
9.45	-7.92	32,791	70,515	4,628	1,340	524	5,991
9.50	-7.98	30,378	76,372	3,738	1,124	528	6,100
9.55	-8.03	37,788	60,023	3,377	1,000	528	6,397
9.60	-8.08	45,567	40,454	2,427	1,097	570	5,772
9.65	-8.13	53,959	37,065	2,644	1,090	589	6,241
9.70	-8.18	40,502	47,172	2,855	679	545	5,882
9.75	-8.23	41,123	48,815	3,433	712	562	5,704
9.80	-8.28	24,236	62,475	2,697	765	535	5,278
9.86	-8.33	29,204	50,241	3,087	957	577	5,638
9.91	-8.38	28,889	44,195	2,874	1,553	617	5,498
10.01	-8.48	22,416	90,852	2,986	936	463	5,529
10.06	-8.53	18,688	82,668	2,216	749	539	5,364
10.11	-8.59	18,087	69,066	2,450	783	559	5,080
10.16	-8.64	21,406	51,019	2,228	1,134	645	5,167
10.21	-8.69	22,515	67,252	2,084	705	603	5,497
10.26	-8.74	13,709	72,461	3,192	973	603	4,878
10.31	-8.79	8,781	82,842	4,422	974	653	4,884
10.36	-8.84	8,837	61,388	3,090	1,027	767	4,910
10.41	-8.89	9,027	71,654	3,677	839	662	4,728
10.46	-8.94	11,830	53,627	2,733	1,031	696	4,646
11.02	-9.50	54,997	45,013	7,727	1,769	606	5,194
11.13	-9.60	3,712	67,423	4,300	1,261	639	4,642
11.18	-9.65	3,127	72,360	5,227	1,751	617	4,673
11.23	-9.70	3,354	80,362	3,601	1,918	687	4,795
11.28	-9.75	3,106	109,454	5,598	1,696	663	5,007
11.33	-9.80	3,772	105,458	5,994	1,523	647	5,401
11.38	-9.86	3,204	120,028	5,771	1,761	746	6,700
11.43	-9.91	2,282	138,990	6,612	1,342	563	5,041
11.48	-9.96	950	152,329	3,848	1,288	513	4,453
11.53	-10.01	2,003	157,628	2,498	2,126	842	8,871
11.58	-10.06	1,633	145,307	2,208	2,001	642	5,547

DBS (m)	Elevation (m)	Fe	Si	Al	Ti	S	P
11.79	-10.26	3,768	80,835	2,378	4,697	1,268	11,786
11.84	-10.31	3,203	108,010	2,390	2,215	889	4,757
11.89	-10.36	3,000	110,371	2,138	2,054	687	4,873
11.94	-10.41	2,926	129,628	2,199	1,811	686	4,806
11.99	-10.46	2,607	116,569	1,793	1,674	629	4,551
12.04	-10.52	3,050	115,919	2,357	2,607	777	6,571
12.09	-10.57	2,228	155,198	2,167	1,514	550	4,914
12.14	-10.62	2,913	130,214	2,433	2,114	590	4,912
12.19	-10.67	2,449	133,184	1,926	2,406	834	8,113
12.24	-10.72	2,491	117,074	1,865	1,861	574	4,595
12.29	-10.77	2,761	132,904	1,818	2,380	967	8,917
12.34	-10.82	2,738	131,038	1,980	1,970	587	4,688
12.40	-10.87	3,170	120,682	2,561	2,284	666	4,765
12.45	-10.92	3,536	125,694	2,577	2,007	1,178	4,980
12.50	-10.97	3,646	91,920	2,307	2,574	698	4,654
12.55	-11.02	2,881	187,892	4,552	3,093	1,062	9,319
12.60	-11.07	3,172	131,231	2,816	1,974	606	4,681
12.90	-11.38	3,165	85,824	2,176	3,971	890	7,416
12.95	-11.43	3,187	126,305	2,194	2,007	663	5,077
13.00	-11.48	3,372	127,309	2,135	1,890	576	4,484
13.06	-11.53	4,101	142,836	2,034	1,913	676	5,907
13.11	-11.58	5,824	127,335	2,852	1,740	528	4,806
13.16	-11.63	3,468	105,186	2,320	1,658	618	4,677
13.21	-11.68	3,483	155,555	3,466	2,401	484	5,168
13.26	-11.73	3,371	133,421	3,500	2,341	497	3,846
13.31	-11.79	3,241	148,864	3,033	2,762	596	5,708
13.36	-11.84	3,781	142,959	3,285	2,324	686	5,891
13.41	-11.89	4,241	132,545	4,191	2,238	561	4,216
13.46	-11.94	7,462	146,351	18,820	5,089	511	4,285
13.51	-11.99	2,990	122,437	6,835	2,708	554	3,781
13.56	-12.04	3,020	152,349	6,161	2,416	590	4,292
13.61	-12.09	3,516	145,592	8,788	3,293	663	4,086
13.67	-12.14	7,308	137,893	13,787	4,220	633	5,090
13.72	-12.19	7,023	118,674	13,118	5,500	663	7,181
13.77	-12.24	5,396	168,776	12,375	4,693	482	4,871
13.82	-12.29	5,088	172,261	9,180	3,827	543	4,399
13.87	-12.34	2,481	180,037	4,239	3,216	9	10,839
13.92	-12.40	1,790	169,635	2,354	1,755	599	5,242
13.97	-12.45	1,584	161,405	2,233	1,486	554	4,302
14.02	-12.50	4,429	145,031	2,364	1,292	5,989	5,989
14.58	-13.06	7,172	99,825	3,442	2,765	666	4,868
14.63	-13.11	6,359	95,453	2,768	2,795	574	4,028

DBS (m)	Elevation (m)	Fe	Si	Al	Ti	S	P
14.68	-13.16	6,612	101,871	2,675	3,325	572	4,610
14.73	-13.21	20,978	151,694	20,370	5,170	578	5,138
14.78	-13.26	39,998	134,416	23,313	5,671	439	4,762
14.83	-13.31	8,563	162,725	4,274	1,761	515	4,418
14.88	-13.36	4,946	170,973	3,071	3,027	473	4,018
14.94	-13.41	3,651	162,897	1,929	993	516	4,093
14.99	-13.46	30,129	117,687	4,170	1,047	579	4,603
15.04	-13.51	93,106	93,764	7,933	2,865	452	5,042
15.09	-13.56	61,504	115,779	29,922	7,309	703	3,762
15.14	-13.61	16,228	122,876	29,998	7,473	464	2,974
15.19	-13.67	24,604	123,526	30,229	6,922	465	2,961
15.24	-13.72	36,230	125,973	31,866	6,489	559	3,600
17.17	-15.65	6,726	176,732	2,897	2,623	518	4,244
17.22	-15.70	6,273	183,250	2,459	1,965	488	4,474
17.27	-15.75	6,452	161,783	2,071	2,121	468	3,931
17.32	-15.80	6,729	128,969	2,187	2,112	542	3,833
17.37	-15.85	5,871	134,055	2,251	1,500	544	3,956
17.42	-15.90	6,215	116,960	2,090	1,739	533	3,508
17.48	-15.95	7,336	109,891	2,675	2,018	575	3,811
17.53	-16.00	6,861	119,821	2,522	1,640	522	3,915
17.58	-16.05	11,778	119,093	18,148	5,751	743	5,713
17.63	-16.10	8,384	128,782	9,524	3,590	519	3,930
17.68	-16.15	7,300	89,872	9,627	6,803	1,236	14,308
18.24	-16.71	5,018	169,496	16,096	5,822	1,214	15,000
18.29	-16.76	4,243	152,162	15,435	5,649	1,222	15,517
18.34	-16.81	4,247	139,180	14,100	5,240	1,458	18,629
18.39	-16.87	3,600	129,587	14,521	5,847	1,414	16,012
18.44	-16.92	2,474	110,847	6,776	6,031	1,243	13,121
18.49	-16.97	2,826	119,074	9,194	6,376	1,335	14,591
18.54	-17.02	3,919	124,384	17,439	6,653	1,446	13,257
18.59	-17.07	2,824	126,963	7,871	5,216	1,333	14,784
18.64	-17.12	3,613	146,771	12,822	5,072	1,396	15,267
18.75	-17.22	4,370	151,729	14,410	5,618	936	11,228
18.80	-17.27	4,023	129,248	16,203	4,337	441	10,693
18.85	-17.32	4,144	96,130	14,209	3,016	637	4,225
18.90	-17.37	6,812	104,651	16,917	3,355	592	5,798
18.95	-17.42	13,797	152,971	21,682	5,568	635	6,085
19.00	-17.48	31,558	143,600	24,961	6,502	511	3,440
19.05	-17.53	42,189	151,995	26,184	7,373	515	3,830
19.10	-17.58	40,003	150,764	29,578	7,554	499	3,998
19.15	-17.63	24,636	132,893	25,038	6,863	430	3,686
19.20	-17.68	28,239	135,803	22,825	7,305	445	3,429

DBS (m)	Elevation (m)	Fe	Si	Al	Ti	S	P
19.25	-17.73	25,091	149,600	26,343	7,151	414	3,649
19.30	-17.78	17,923	147,902	25,421	6,971	412	3,258
19.35	-17.83	19,133	142,262	25,575	6,782	392	3,129
19.41	-17.88	12,892	143,834	26,642	6,923	431	3,605
19.46	-17.93	12,763	145,212	24,303	6,491	428	3,143
19.51	-17.98	23,814	134,034	25,053	6,312	520	3,396
19.56	-18.03	6,995	189,698	13,399	6,919	1,034	10,416
19.61	-18.08	3,664	198,253	16,951	5,259	1,316	11,869
19.66	-18.14	21,811	154,817	24,486	6,505	735	4,577
19.71	-18.19	28,372	139,363	32,781	5,444	625	3,393
19.76	-18.24	12,088	144,966	30,807	5,345	907	3,447
19.81	-18.29	19,772	136,650	30,035	5,286	477	3,091
19.86	-18.34	18,470	159,685	39,657	5,478	471	3,254
19.91	-18.39	23,477	141,189	29,682	5,612	389	3,223
19.96	-18.44	32,687	140,352	30,004	5,417	405	3,686
20.02	-18.49	32,577	149,168	33,778	5,650	395	3,529
20.07	-18.54	29,774	166,766	40,381	5,525	356	2,890
20.12	-18.59	34,460	135,571	28,465	5,239	384	3,658

Table H.2 The Data from Sediment pH, Sediment Oxidation/Reduction Potential (mV), and Total Volatile Organic Compounds (Reported as Chlorobenzene) in the Each Subsample Headspace (ppm) as a Function of Depth (m)

DBS(m)	Elevation (m)	pH	ORP (mV)	Chlorobenzene (ppm)
3.35	-1.83	7.03	313.5	0
3.40	-1.88	7.55	86.4	0
3.45	-1.93	7.04	306.6	0
3.51	-1.98	6.48	195.4	0
3.56	-2.03	6.16	540.0	0
3.61	-2.08	6.39	625.4	0
3.66	-2.13	6.24	597.4	0
3.71	-2.18	5.99	651.0	0
3.76	-2.24	6.16	613.4	0
3.81	-2.29	6.13	613.5	0
3.91	-2.39	6.99	445.0	0
3.96	-2.44	6.38	426.9	0
4.01	-2.49	6.75	414.7	0
4.06	-2.54	6.94	281.6	0
4.11	-2.59	6.96	287.1	0
4.17	-2.64	7.38	519.5	0
4.22	-2.69	6.84	126.8	0
4.27	-2.74	6.72	337.8	0
4.32	-2.79	6.82	146.9	0
4.37	-2.84	6.86	528.5	0
4.42	-2.90	6.85	331.3	0
4.47	-2.95	7.14	76.1	0
4.52	-3.00	7.05	538.6	0
4.57	-3.05	6.9	92.0	0
4.62	-3.10	6.49	344.5	0.2
4.67	-3.15	6.43	517.2	0
4.72	-3.20	6.9	112.5	0
4.78	-3.25	7.21	34.8	0
4.83	-3.30	6.18	261.0	0.1
4.88	-3.35	6.87	65.5	0.1
4.93	-3.40	6.6	224.8	0.3
4.98	-3.45	6.81	238.8	0.2
5.03	-3.51	6.6	201.1	0
5.08	-3.56	6.58	186.3	0.1
5.13	-3.61	6.71	210.3	0
5.18	-3.66	6.83	187.6	0.1
5.23	-3.71	6.84	494.1	2
5.28	-3.76	6.63	486.1	1.7

DBS(m)	Elevation (m)	pH	ORP (mV)	Chlorobenzene (ppm)
5.33	-3.81		255.8	1.1
5.38	-3.86	6.58	574.9	0.6
5.44	-3.91	6.67	569.3	0
5.49	-3.96	6.83	513.0	0
5.99	-4.47	6.38	472.1	1
6.05	-4.52	6.07	477.4	1.2
6.10	-4.57	6.2	521.6	3.3
6.15	-4.62	6.05	416.2	1.8
6.20	-4.67	6.35	447.3	1.6
6.25	-4.72	6.2	355.4	2.2
6.35	-4.83	6.64	96.6	1.1
6.40	-4.88	6.34	85.4	0
6.45	-4.93	6.62	75.4	2.7
6.50	-4.98	6.56	-28.3	0.3
6.55	-5.03	6.66	-14.7	1.1
6.60	-5.08	6.52	136.0	0.3
6.65	-5.13	7.26	-0.4	3.3
6.71	-5.18	7.13	3.9	2.1
6.76	-5.23	7.45	-63.5	0.5
6.81	-5.28	6.83	-7.9	0.1
6.86	-5.33	7.07	32.4	0.1
6.91	-5.38	6.67	84.8	0.1
6.96	-5.44	7.08	35.3	0
7.01	-5.49	6.83	44.4	0
7.06	-5.54	6.73	62.8	0
7.11	-5.59	6.87	36.0	0.3
7.16	-5.64	6.80	82.0	0
7.21	-5.69	6.09	146.0	0.3
7.26	-5.74	5.90	163.6	0.1
7.32	-5.79	6.06	107.8	0
7.37	-5.84	6.29	108.5	0.3
7.42	-5.89	5.63	102.5	0.1
7.47	-5.94	6.36	60.8	0.2
7.52	-5.99	6.79	9.3	0.2
7.57	-6.05	6.66	265.6	0.4
7.62	-6.10	6.34	330.1	1.3
7.67	-6.15	5.68	252.6	1.2
7.72	-6.20	6.75	211.1	1.3
7.77	-6.25	6.55	13.5	0.5
7.82	-6.30	6.98	-6.3	1
7.87	-6.35	6.89	2.4	1.2
7.92	-6.40	6.50	83.5	1.3

DBS(m)	Elevation (m)	pH	ORP (mV)	Chlorobenzene (ppm)
8.48	-6.96	6.55	21.2	1.3
8.23	-6.71	6.93	-20.7	0.3
8.28	-6.76	6.07	29.2	0
8.74	-7.21	7.04	-45.2	1.7
8.79	-7.26	5.68	-0.8	0.2
8.84	-7.32	6.73	-46.4	0.7
8.89	-7.37	5.72	47.8	0.8
8.94	-7.42	5.88	78.6	0.2
8.99	-7.47	6.75	-10.2	0.6
9.04	-7.52	6.89	-21.5	0.3
9.09	-7.57	6.78	-6.9	0.1
9.14	-7.62	6.75	-84.0	0.3
9.45	-7.92	6.16	43.3	0.3
9.50	-7.98	7.14	-44.6	0.2
9.55	-8.03	7.15	-78.2	0.4
9.60	-8.08	6.66	-31.9	1.5
9.65	-8.13	7.14	-58.3	0.2
9.70	-8.18	6.73	-25.2	0.8
9.75	-8.23	7.13	-50.6	2.2
9.80	-8.28	7.15	-42.8	0.7
9.86	-8.33	7.13	-50.9	3
9.91	-8.38	7.02	-65.3	2.5
10.01	-8.48	5.98	85.1	0.3
10.06	-8.53	6.77	-54.3	1.2
10.11	-8.59	6.98	-77.9	0.5
10.16	-8.64	6.87	-23.6	1.1
10.21	-8.69	7.20	-75.7	0.9
10.26	-8.74	6.78	-46.9	4.6
10.31	-8.79	6.89	-42.2	0.3
10.36	-8.84	7.27	-74.2	0.5
10.41	-8.89	6.31	80.3	0.7
10.46	-8.94	6.48	-74.4	0.8
11.02	-9.50	7.16	-141.4	0.4
11.13	-9.60	7.31	-129.0	5.2
11.18	-9.65	6.94	-102.2	1.8
11.23	-9.70	6.96	-73.2	0.5
11.28	-9.75	5.91	202.7	4.4
11.33	-9.80	5.80	269.1	0.8
11.38	-9.86	6.69	179.5	1.9
11.43	-9.91	5.57	106.6	0.4
11.48	-9.96	6.13	76.3	1.3
11.53	-10.01	6.32	196.0	1

DBS(m)	Elevation (m)	pH	ORP (mV)	Chlorobenzene (ppm)
11.58	-10.06	7.38	-11.6	0.1
11.79	-10.26	7.74	-99.5	0.9
11.84	-10.31	7.49	-87.5	0.2
11.89	-10.36	7.89	-101.7	0.7
11.94	-10.41	8.03	-55.3	0.7
11.99	-10.46	7.89	-55.4	0.5
12.04	-10.52	7.04	55.3	1.4
12.09	-10.57	7.22	31.0	0
12.14	-10.62	7.28	36.9	0.1
12.19	-10.67	7.28	23.6	0.1
12.24	-10.72	7.15	19.4	0.3
12.29	-10.77	7.23	-68.8	0.7
12.34	-10.82	7.33	-125.5	1.2
12.40	-10.87	7.39	-61.3	0.5
12.45	-10.92	7.52	-73.1	0.4
12.50	-10.97	7.50	18.4	0.4
12.55	-11.02	7.45	-123.0	0.4
12.60	-11.07	6.79	-90.6	0.4
12.90	-11.38	7.53	-27.3	6.4
12.95	-11.43	7.01	165.0	2.2
13.00	-11.48	6.55	176.4	0.9
13.06	-11.53	7.07	-70.5	0.9
13.11	-11.58	6.47	79.0	0.2
13.16	-11.63	6.40	212.0	0
13.21	-11.68	5.55	203.0	0.7
13.26	-11.73	7.67	-5.8	0
13.31	-11.79	7.47	39.1	1.2
13.36	-11.84	6.91	66.0	0.7
13.41	-11.89	6.66	-7.6	0.5
13.46	-11.94	5.10	123.7	2.4
13.51	-11.99	5.26	114.7	0.7
13.56	-12.04	5.20	186.2	0.6
13.61	-12.09	5.70	119.5	1.1
13.67	-12.14	4.83	196.7	1.3
13.72	-12.19	4.88	132.5	0.5
13.77	-12.24	4.38	205.7	0.2
13.82	-12.29	4.96	148.6	0.3
13.87	-12.34	6.08	69.0	0.2
13.92	-12.40	6.17	25.6	0.7
13.97	-12.45	6.34	35.8	0.2
14.02	-12.50	5.49	106.8	0.4
14.58	-13.06	7.94	-115.8	9.6

DBS(m)	Elevation (m)	pH	ORP (mV)	Chlorobenzene (ppm)
14.63	-13.11	7.49	-108.6	1.5
14.68	-13.16	7.43	-92.5	0.4
14.73	-13.21	4.87	51.0	0.2
14.78	-13.26	6.23	-15.9	0.2
14.83	-13.31	5.52	115.3	1.4
14.88	-13.36	5.87	141.1	1
14.94	-13.41	6.47	110.2	1.8
14.99	-13.46	6.35	76.9	1.7
15.04	-13.51	4.86	233.8	2.4
15.09	-13.56	5.65	176.3	7.6
15.14	-13.61	4.91	215.4	1.1
15.19	-13.67	6.8	51.7	0.9
15.24	-13.72	5.78	9.4	0.2
17.17	-15.65	7.05	60.8	0
17.22	-15.70	6.61	83.5	0
17.27	-15.75	6.83	91.4	0.1
17.32	-15.80	6.45	47.5	0.3
17.37	-15.85	6.26	56.0	0.7
17.42	-15.90	6.3	29.0	1.7
17.48	-15.95	6.31	315.9	1.4
17.53	-16.00	6.92	-50.2	0.6
17.58	-16.05	6.9	-37.8	2.4
17.63	-16.10	4.67	154.8	0.3
17.68	-16.15	6.22	146.4	0.6
18.24	-16.71	6.33	158.6	0.1
18.29	-16.76	4.94	209.9	0.4
18.34	-16.81	4.91	233.4	0.2
18.39	-16.87		343.4	0.2
18.44	-16.92	4.39	346.4	1.1
18.49	-16.97	4.51	316.9	0.1
18.54	-17.02	5.93	144.2	0
18.59	-17.07	4.1	134.9	0.1
18.64	-17.12	4.3	322.9	0
18.75	-17.22	6.58	217.8	0
18.80	-17.27	4.45	230.9	0.1
18.85	-17.32	4.6	234.1	0
18.90	-17.37	4.54	214.3	0.2
18.95	-17.42	6.62	-69.2	0.1
19.00	-17.48	5.18	59.6	0
19.05	-17.53	5.23	68.4	0
19.10	-17.58	5.73	31.0	0.4
19.15	-17.63	5.92	-33.0	0

DBS(m)	Elevation (m)	pH	ORP (mV)	Chlorobenzene (ppm)
19.20	-17.68	5.74	-8.6	0
19.25	-17.73	4.04	162.9	0
19.30	-17.78	5.27	139.4	0
19.35	-17.83	3.74	191.1	0
19.41	-17.88	5.92	71.5	0
19.46	-17.93	6.51	-4.9	0
19.51	-17.98	5.29	29.3	0
19.56	-18.03	4.24	148.4	0
19.61	-18.08	4.46	152.8	0
19.66	-18.14	4.31	157.7	0.2
19.71	-18.19	5.38	135.4	0
19.76	-18.24	3.79	340.2	0
19.81	-18.29	5.82	279.1	0
19.86	-18.34	5.83	260.6	0.3
19.91	-18.39	6.26	214.9	0
19.96	-18.44	6.49	179.6	0.2
20.02	-18.49	6.2	179.4	0.2
20.07	-18.54	6.68	151.3	0.2
20.12	-18.59	6.9	166.4	0.2

APPENDIX I
SEQUENTIAL EXTRACTION DATA OF SEDIMENT SAMPLES FROM
REDOX TRANSITION ZONES

A six-step sequential extraction was conducted for accessing the reactive Fe minerals (from bulk to mineral coating) in the sediment sample collected from four redox transition zones. The concentrations of different Fe speciation in Upper Zone (Table I.1), Zone 1 (Table I.2), Zone 2 (Table I.3) and Zone 3 (Table I.4) were listed in the following tables.

Table I.1 The Concentration of Different Fe Minerals in Upper Zone determined with A Six-Step Sequential Extraction

DBS (m)	Sample Number	Ion exchangeable Fe	Siderite	Amorphous Fe	Goethite, lepidocrocite, hematite	Magnetite	Pyrite/Pyrrhotite	Total Fe	XRF	
		Fe(II) (ug/g)	Fe(II) (ug/g)	Fe(II) and Fe(III) (ug/g)	Fe(III) (ug/g)	Fe(II/III) (ug/g)	Fe(II) (ug/g)	Fe (ug/g)	ppm	ratio
13.00	2-3a	102	1,059	455	5,070	1,372	4,365	12,423	11,086	1.12
		103	1,039	496	5,600	1,555	4,360	13,153	11,086	1.19
	2-3b	102	1,092	580	5,750	1,763	4,850	14,137	13,906	1.02
		104	1,070	542	5,630	1,647	4,970	13,963	13,906	1.00
	average	103	1,065	518	5,513	1,584	4,636	13,419	12,496	1.08
13.17	2-4a	109	1,090	507	6,570	1,310	4,445	14,031	9,333	1.50
		107	1,071	549	5,640	1,365	4,730	13,462	9,333	1.44
	2-4b	107	1,047	511	5,490	1,174	4,240	12,569	8,881	1.42
		107	1,065	520	5,620	1,174	4,375	12,861	8,881	1.45
	average	107	1,068	522	5,830	1,256	4,448	13,231	9,107	1.45
13.33	2-5a	73	1,461	1,500	7,970	2,370	3,061	16,435	14,430	1.14
		74	1,438	1,485	8,110	2,640	2,671	16,418	14,430	1.14
	2-5b	1,152	1,461	2,431	1,767	2,523	2,540	11,874	16,582	0.72
		81	1,419	2,403	1,764	2,798	2,215	10,680	16,582	0.64
	average	345	1,445	1,955	4,903	2,583	2,622	13,852	15,506	0.91
13.50	2-6a	81	1,445	2,414	1,778	1,158	1,120	7,995	7,458	1.07
		81	1,495	2,466	1,798	1,405	1,233	8,478	7,458	1.14
	2-6b	86	1,456	2,402	1,779	2,528	834	9,085	10,221	0.89
		84	1,468	2,404	1,776	2,743	1,035	9,509	10,221	0.93
	average	83	1,466	2,422	1,783	1,958	1,055	8,767	8,839	1.01
13.67	2-7a	149	1,663	2,662	2,419	5,123	1,886	13,901	14,700	0.95
		90	1,510	2,662	2,264	3,038	654	10,217	14,700	0.70
	2-7a	93	1,587	2,530	2,314	3,518	961	11,002	15,592	0.71
		94	1,594	2,564	2,331	3,688	1,253	11,524	15,592	0.74
	average	106	1,589	2,605	2,332	3,841	1,189	11,661	15,146	0.77

Table I.1 The Concentration of Different Fe Minerals in Upper Zone determined with A Six-Step Sequential Extraction (Continued)

DBS (m)	Sample Number	Ion exchangeable Fe	Siderite	Amorphous Fe	Goethite, lepidocrocite, hematite	Magnetite	Pyrite/Pyrrhotite	Total Fe	XRF	
		Fe(II) (ug/g)	Fe(II) (ug/g)	Fe(II) and Fe(III) (ug/g)	Fe(III) (ug/g)	Fe(II/III) (ug/g)	Fe(II) (ug/g)	Fe (ug/g)	ppm	ratio
13.83	2-8a	88	1,694	2,916	2,553	5,335	2,285	14,870	18,431	0.81
		86	1,781	3,064	2,638	5,813	2,896	16,277	18,431	0.88
	2-8b	114	2,558	6,306	3,301	7,793	5,455	25,527	30,049	0.85
		115	2,008	6,855	3,533	9,210	2,499	24,220	30,049	0.81
	average	101	2,010	4,785	3,006	7,038	3,283	20,223	24,240	0.84
14.00	2-9a	91	1,676	2,930	1,993	2,113	3,040	11,842	11,943	0.99
		94	1,820	3,060	2,052	3,650	3,058	13,734	11,943	1.15
	2-9b	92	1,616	2,636	1,913	3,695	2,097	12,049	12,581	0.96
		95	1,650	2,678	1,929	3,820	2,483	12,654	12,581	1.01
	average	93	1,691	2,826	1,972	3,319	2,669	12,570	12,262	1.03
14.17	2-10a	95	1,603	2,617	2,160	3,220	2,141	11,836	12,438	0.95
		97	1,578	2,545	2,110	2,795	1,491	10,616	12,438	0.85
	2-10b	102	1,640	2,709	2,154	3,478	2,447	12,529	16,638	0.75
		95	1,689	2,730	2,170	4,280	2,621	13,585	16,638	0.82
	average	97	1,628	2,650	2,149	3,443	2,175	12,142	14,538	0.84
14.33	2-11a	138	682	1,792	3,013	4,220	2,506	12,351	19,050	0.65
		139	651	1,765	3,002	4,248	2,498	12,302	19,050	0.65
	2-11b	139	666	1,831	3,007	1,895	2,119	9,657	13,942	0.69
		138	621	1,701	2,583	1,697	1,801	8,541	13,942	0.61
	average	139	655	1,772	2,901	3,015	2,231	10,713	16,496	0.65
14.50	3-1a	138	810	2,014	3,568	2,197	2,457	11,183	13,021	0.86
		137	688	1,775	2,928	1,910	1,904	9,341	13,021	0.72
	3-1b	137	744	1,839	3,139	1,951	2,359	10,169	14,630	0.70
		135	623	1,663	2,674	1,637	1,699	8,430	14,630	0.58
	average	137	716	1,823	3,077	1,924	2,105	9,781	13,826	0.71

Table I.1 The Concentration of Different Fe Minerals in Upper Zone determined with A Six-Step Sequential Extraction (Continued)

DBS (m)	Sample Number	Ion exchangeable Fe	Siderite	Amorphous Fe	Goethite, lepidocrocite, hematite	Magnetite	Pyrite/Pyrrhotite	Total Fe	XRF	
		Fe(II) (ug/g)	Fe(II) (ug/g)	Fe(II) and Fe(III) (ug/g)	Fe(III) (ug/g)	Fe(II/III) (ug/g)	Fe(II) (ug/g)	Fe (ug/g)	ppm	ratio
14.67	3-2a	136	828	1,945	3,589	2,084	2,564	11,146	15,915	0.70
		136	701	1,738	2,863	1,816	1,949	9,202	15,915	0.58
	3-2b	137	698	1,791	4,839	1,839	1,949	11,253	14,122	0.80
		136	723	1,755	3,189	1,870	2,063	9,735	14,122	0.69
	average	136	737	1,807	3,620	1,902	2,131	10,334	15,018	0.69
14.83	3-3a	139	873	2,237	5,337	2,717	3,383	14,686	16,684	0.88
		140	908	2,152	4,104	2,568	2,928	12,800	16,684	0.77
	3-3b	135	869	2,073	3,569	2,268	2,860	11,773	18,046	0.65
		133	910	2,086	3,507	2,423	3,184	12,243	18,046	0.68
	average	137	890	2,137	4,129	2,494	3,089	12,875	17,365	0.74
15.00	3-4a	133	754	1,776	2,645	1,959	2,537	9,804	18,511	0.53
		130	779	1,803	2,976	2,252	2,681	10,621	18,511	0.57
	3-4b	133	815	1,864	2,933	2,267	2,991	11,003	18,261	0.60
		132	797	1,783	2,613	2,115	2,422	9,862	18,261	0.54
	average	132	786	1,807	2,792	2,148	2,658	10,322	18,386	0.56

Table I.2 The Concentration of Different Fe Minerals in Zone 1 determined with A Six-Step Sequential Extraction

DBS (m)	Sample Number	Ion exchangeable Fe	Siderite	Amorphous Fe	Goethite, lepidocrocite, hematite	Magnetite	Pyrite/Pyrrhotite	Total Fe	XRF	
		Fe(II) (ug/g)	Fe(II) (ug/g)	Fe(II) and Fe(III) (ug/g)	Fe(III) (ug/g)	Fe(II/III) (ug/g)	Fe(II) (ug/g)	Fe (ug/g)	ppm	ratio
6.35	6-3a	392	5,770	1,412	8,780	13,616	10,106	40,076	35,910	1.12
		391	4,920	1,189	10,020	11,074	8,654	36,248	35,910	1.01
	6-3b	350	3,970	606	9,210	11,232	6,922	32,290	28,410	1.14
		355	4,270	954	10,320	9,914	7,214	33,027	28,410	1.16
	average	372	4,733	1,040	9,583	11,459	8,224	35,410	32,160	1.10
6.40	6-4a	330	6,100	1,855	10,260	10,860	10,242	39,647	29,196	1.36
		345	5,590	1,862	10,640	13,000	11,318	42,755	29,196	1.46
	6-4b	325	7,060	7,250	11,340	10,580	8,738	45,293	31,649	1.43
		339	8,070	8,180	11,510	10,585	7,792	46,476	31,649	1.47
	average	335	6,705	4,787	10,938	11,256	9,523	43,543	30,423	1.43
6.45	6-5a	220	9,000	4,800	9,070	4,290	9,070	36,450	32,548	1.12
		234	8,250	3,400	15,260	4,880	11,820	43,844	32,548	1.35
	6-5b	192	8,860	5,200	5,580	5,930	7,600	33,362	35,139	0.95
		227	9,340	6,500	5,430	4,850	8,850	35,197	35,139	1.00
	average	218	8,863	4,975	8,835	4,988	9,335	37,213	33,843	1.10
6.50	6-6a	232	6,440	3,100	14,800	5,150	13,640	43,362	24,876	1.74
		276	7,080	2,600	17,580	5,650	14,500	47,686	24,876	1.92
	6-6b	273	8,200	6,500	7,640	6,070	9,870	38,553	31,645	1.22
		286	8,710	6,000	8,910	6,410	10,140	40,456	31,645	1.28
	average	267	7,608	4,550	12,233	5,820	12,038	42,514	28,260	1.54
6.55	6-7a	121	2,840	2,521	12,350	5,190	9,010	32,032	33,239	0.96
		139	2,680	1,188	16,810	5,600	12,400	38,817	33,239	1.17
	6-7a	145	2,780	1,824	14,730	5,810	10,630	35,919	30,675	1.17
		170	4,240	4,431	22,900	5,910	17,240	54,891	30,675	1.79
	average	144	3,135	2,491	16,698	5,628	12,320	40,415	31,957	1.27

Table I.2 The Concentration of Different Fe Minerals in Zone 1 determined with A Six-Step Sequential Extraction (Continued)

DBS (m)	Sample Number	Ion exchangeable Fe	Siderite	Amorphous Fe	Goethite, lepidocrocite, hematite	Magnetite	Pyrite/Pyrrhotite	Total Fe	XRF	
		Fe(II) (ug/g)	Fe(II) (ug/g)	Fe(II) and Fe(III) (ug/g)	Fe(III) (ug/g)	Fe(II/III) (ug/g)	Fe(II) (ug/g)	Fe (ug/g)	ppm	ratio
6.61	6-8a	279	7,090	5,001	15,030	6,690	15,340	49,430	40,969	1.21
		291	7,140	6,540	13,540	7,220	14,270	49,001	40,969	1.20
	6-8b	268	8,690	5,196	14,520	6,740	13,180	48,594	43,116	1.13
		297	8,300	6,410	15,340	6,690	12,670	49,707	43,116	1.15
	average	284	7,805	5,787	14,608	6,835	13,865	49,183	42,043	1.17
6.65	6-9a	232	8,590	9,360	9,900	8,510	13,860	50,452	44,218	1.14
		225	8,220	8,010	9,520	9,030	14,460	49,465	44,218	1.12
	6-9b	196	8,070	7,160	16,080	10,130	13,970	55,606	39,393	1.41
		222	7,720	7,110	16,100	7,820	16,900	55,872	39,393	1.42
	average	219	8,150	7,910	12,900	8,873	14,798	52,849	41,806	1.27
6.71	6-10a	295	9,260	10,700	10,140	8,880	9,520	48,795	51,208	0.95
		306	16,150	11,750	11,210	11,490	10,370	61,276	51,208	1.20
	6-10b	359	8,860	10,420	11,050	13,630	11,120	55,439	54,343	1.02
		391	9,170	11,050	10,720	10,870	10,610	52,811	54,343	0.97
	average	338	10,860	10,980	10,780	11,218	10,405	54,580	52,775	1.04
6.76	6-11a	104	4,680	5,850	9,080	7,850	9,490	37,054	43,749	0.85
		117	3,560	4,740	8,130	6,240	5,760	28,547	43,749	0.65
	6-11b	134	5,810	7,040	9,710	13,580	8,950	45,224	45,311	1.00
		140	5,350	5,680	8,390	9,970	7,160	36,690	45,311	0.81
	average	124	4,850	5,828	8,828	9,410	7,840	36,879	44,530	0.83
6.81	7-1a	170	7,910	6,820	9,160	10,290	9,580	43,930	43,918	1.00
		168	8,250	5,150	9,240	14,270	10,340	47,418	43,918	1.08
	7-1b	177	9,630	6,350	10,070	13,920	12,590	52,737	37,799	1.40
		194	7,770	6,780	9,590	16,030	11,670	52,034	37,799	1.38
	average	177	8,390	6,275	9,515	13,628	11,045	49,030	40,858	1.21

Table I.2 The Concentration of Different Fe Minerals in Zone 1 determined with A Six-Step Sequential Extraction (Continued)

DBS (m)	Sample Number	Ion exchangeable Fe	Siderite	Amorphous Fe	Goethite, lepidocrocite, hematite	Magnetite	Pyrite/Pyrrhotite	Total Fe	XRF	
		Fe(II) (ug/g)	Fe(II) (ug/g)	Fe(II) and Fe(III) (ug/g)	Fe(III) (ug/g)	Fe(II/III) (ug/g)	Fe(II) (ug/g)	Fe (ug/g)	ppm	ratio
6.83	7-2a	120	4,590	5,270	9,830	12,930	13,000	45,740	26,970	1.70
		207	5,330	5,970	10,600	15,630	12,310	50,047	26,970	1.86
	7-2b	246	6,050	5,780	10,570	13,690	12,810	49,146	33,225	1.48
		261	6,150	7,170	10,650	14,850	12,650	51,731	33,225	1.56
	average	209	5,530	6,048	10,413	14,275	12,693	49,166	30,098	1.65
6.91	7-3a	333	6,980	6,920	10,460	14,710	12,610	52,013	38,386	1.35
		384	7,630	7,130	10,640	17,380	13,570	56,734	38,386	1.48
	7-3b	378	8,270	8,010	10,790	14,700	13,500	55,648	39,089	1.42
		416	8,910	8,640	11,010	14,080	13,820	56,876	39,089	1.46
	average	378	7,948	7,675	10,725	15,218	13,375	55,318	38,738	1.43

Table I.3 The Concentration of Different Fe Minerals in Zone 2 determined with A Six-Step Sequential Extraction

DBS (m)	Sample Number	Ion exchangeable Fe	Siderite	Amorphous Fe	Goethite, lepidocrocite, hematite	Magnetite	Pyrite/Pyrrhotite	Total Fe	XRF	
		Fe(II) (ug/g)	Fe(II) (ug/g)	Fe(II) and Fe(III) (ug/g)	Fe(III) (ug/g)	Fe(II/III) (ug/g)	Fe(II) (ug/g)	Fe (ug/g)	ppm	ratio
31.00	11-2a	199	2,560	4,090	4,760	38,700	6,060	56,369	47,964	1.18
		184	2,480	3,710	4,490	20,070	5,550	36,484	47,964	0.76
	11-2b	193	2,700	4,110	4,710	22,950	6,100	40,763	34,983	1.17
		206	2,710	4,080	4,790	26,990	5,700	44,476	34,983	1.27
	average	196	2,613	3,998	4,688	27,178	5,853	44,523	41,473	1.09
31.17	11-3a	237	3,380	4,020	4,460	16,720	5,460	34,277	33,889	1.01
		250	3,740	4,570	4,600	19,380	5,600	38,140	33,889	1.13
	11-3b	253	3,980	4,760	4,690	23,530	5,730	42,943	37,385	1.15
		282	3,540	4,090	4,770	20,820	5,570	39,072	37,385	1.05
	average	256	3,660	4,360	4,630	20,113	5,590	38,608	35,637	1.08
31.33	11-4a	108	5,800	3,120	6,730	14,800	6,760	37,318	20,390	1.83
		108	5,890	3,185	6,870	14,910	6,610	37,573	20,390	1.84
	11-4b	112	5,870	3,175	6,730	12,900	6,660	35,447	37,788	0.94
		112	6,030	3,220	6,760	13,060	6,880	36,062	37,788	0.95
	average	110	5,898	3,175	6,773	13,918	6,728	36,600	29,089	1.39
31.50	11-5a	116	5,990	6,830	7,060	22,360	6,810	49,166	38,416	1.28
		118	6,190	6,880	7,260	24,210	7,030	51,688	38,416	1.35
	11-5b	125	7,320	10,960	9,530	24,000	6,950	58,885	43,021	1.37
		119	6,340	7,040	7,100	23,940	6,810	51,349	43,021	1.19
	average	119	6,460	7,928	7,738	23,628	6,900	52,772	40,718	1.30
31.67	11-6a	146	7,090	620	490	28,510	3,950	40,806	52,847	0.77
		146	7,170	530	730	25,960	6,660	41,196	52,847	0.78
	11-6a	142	6,970	390	800	23,960	5,820	38,082	53,506	0.71
		141	7,060	420	960	22,440	3,550	34,571	53,506	0.65
	average	144	7,073	490	745	25,218	4,995	38,664	53,176	0.73

Table I.3 The Concentration of Different Fe Minerals in Zone 2 determined with A Six-Step Sequential Extraction (Continued)

DBS (m)	Sample Number	Ion exchangeable Fe	Siderite	Amorphous Fe	Goethite, lepidocrocite, hematite	Magnetite	Pyrite/Pyrrhotite	Total Fe	XRF	
		Fe(II) (ug/g)	Fe(II) (ug/g)	Fe(II) and Fe(III) (ug/g)	Fe(III) (ug/g)	Fe(II/III) (ug/g)	Fe(II) (ug/g)	Fe (ug/g)	ppm	ratio
31.83	11-7a	144	7,130	360	770	28,760	5,250	42,414	51,026	0.83
		144	7,040	360	580	27,670	4,520	40,314	51,026	0.79
	11-7b	145	7,030	260	470	22,270	1,170	31,345	35,609	0.88
		147	7,220	290	430	20,760	460	29,307	35,609	0.82
	average	145	7,105	318	563	24,865	2,850	35,845	43,318	0.83
32.00	11-8a	244	4,160	5,740	12,050	14,970	4,980	42,144	38,834	1.09
		244	4,220	5,910	11,500	15,730	4,990	42,594	38,834	1.10
	11-8b	289	4,810	6,180	12,680	23,030	5,250	52,239	53,982	0.97
		256	4,500	6,050	12,000	13,670	4,910	41,386	53,982	0.77
	average	258	4,423	5,970	12,058	16,850	5,033	44,591	46,408	0.98
32.17	11-9a	237	4,310	6,030	11,590	9,540	4,990	36,697	23,964	1.53
		285	4,720	3,150	12,050	15,040	5,270	40,515	23,964	1.69
	11-9b	252	4,500	3,055	11,590	9,340	5,090	33,827	22,777	1.49
		271	4,650	3,130	11,320	9,090	5,160	33,621	22,777	1.48
	average	261	4,545	3,841	11,638	10,753	5,128	36,165	23,370	1.55
32.33	11-10a	183	4,200	3,110	11,370	9,310	5,130	33,303	32,418	1.03
		193	4,230	3,165	12,210	12,220	5,210	37,228	32,418	1.15
	11-10b	199	4,180	3,140	11,850	10,080	5,260	34,709	28,726	1.21
		211	4,380	3,245	11,890	9,880	5,440	35,046	28,726	1.22
	average	197	4,248	3,165	11,830	10,373	5,260	35,072	30,572	1.15
32.50	11-11a	310	5,090	3,245	11,470	8,030	5,260	33,405	27,795	1.20
		278	4,840	3,285	10,410	5,830	5,370	30,013	27,795	1.08
	11-11b	326	5,220	3,310	11,780	8,570	5,370	34,576	27,367	1.26
		359	5,500	3,355	12,310	11,730	5,520	38,774	27,367	1.42
	average	318	5,163	3,299	11,493	8,540	5,380	34,192	27,581	1.24

Table I.3 The Concentration of Different Fe Minerals in Zone 2 determined with A Six-Step Sequential Extraction (Continued)

DBS (m)	Sample Number	Ion exchangeable Fe	Siderite	Amorphous Fe	Goethite, lepidocrocite, hematite	Magnetite	Pyrite/Pyrrhotite	Total Fe	XRF	
		Fe(II) (ug/g)	Fe(II) (ug/g)	Fe(II) and Fe(III) (ug/g)	Fe(III) (ug/g)	Fe(II/III) (ug/g)	Fe(II) (ug/g)	Fe (ug/g)	ppm	ratio
32.83	12-2a	264	4,750	3,320	1,077	12,240	389	22,040	24,418	0.90
		274	4,690	3,345	1,094	10,510	419	20,332	24,418	0.83
	12-2b	292	4,910	3,415	9,680	11,150	5,570	35,017	21,402	1.64
		299	4,930	3,475	10,200	12,190	5,680	36,774	21,402	1.72
	average	282	4,820	3,389	5,513	11,523	3,015	28,541	22,910	1.27
33.00	12-3a	308	5,030	3,475	12,250	9,500	5,610	36,173	19,278	1.88
		329	5,140	3,475	11,720	9,350	5,610	35,624	19,278	1.85
	12-3b	343	5,270	3,560	12,020	9,690	5,710	36,593	21,462	1.71
		342	5,300	3,575	12,220	10,870	5,750	38,057	21,462	1.77
	average	331	5,185	3,521	12,053	9,853	5,670	36,612	20,370	1.80
33.17	12-4a	80	446	890	578	19,080	2,440	23,514	18,087	1.30
		71	607	1,097	1,049	13,170	1,571	17,565	18,087	0.97
	12-4b	74	1,091	1,259	1,123	20,700	1,866	26,113	35,726	0.73
		70	1,143	1,445	1,171	24,360	3,401	31,590	35,726	0.88
	average	74	822	1,173	980	19,328	2,320	24,696	26,907	0.97
33.33	12-5a	77	524	866	1,164	16,030	911	19,572	24,119	0.81
		71	530	902	1,111	17,430	1,816	21,860	24,119	0.91
	12-5b	73	525	881	1,082	16,460	1,355	20,376	19,575	1.04
		70	545	886	1,342	16,080	648	19,571	19,575	1.00
	average	73	531	884	1,175	16,500	1,183	20,345	21,847	0.94
33.50	12-6a	171	1,293	1,068	1,013	12,870	1,259	17,674	19,037	0.93
		174	1,344	1,099	1,024	11,760	1,460	16,861	19,037	0.89
	12-6a	115	788	824	936	10,610	150	13,423	18,857	0.71
		123	788	842	973	10,930	148	13,804	18,857	0.73
	average	146	1,053	958	987	11,543	754	15,441	18,947	0.81

Table I.3 The Concentration of Different Fe Minerals in Zone 2 determined with A Six-Step Sequential Extraction (Continued)

DBS (m)	Sample Number	Ion exchangeable Fe	Siderite	Amorphous Fe	Goethite, lepidocrocite, hematite	Magnetite	Pyrite/Pyrrhotite	Total Fe	XRF	
		Fe(II) (ug/g)	Fe(II) (ug/g)	Fe(II) and Fe(III) (ug/g)	Fe(III) (ug/g)	Fe(II/III) (ug/g)	Fe(II) (ug/g)	Fe (ug/g)	ppm	ratio
33.67	12-7a	78	614	883	981	12,120	153	14,829	13,709	1.08
		80	624	894	991	13,570	144	16,303	13,709	1.19
	12-7b	86	687	883	980	12,250	243	15,129	13,709	1.10
		118	674	890	1,022	11,260	152	14,116	13,709	1.03
	average	90	650	888	994	12,300	173	15,094	13,709	1.10
33.83	12-8a	76	622	840	970	8,540	110	11,158	8,781	1.27
		77	647	854	984	9,030	126	11,718	8,781	1.33
	12-8b	80	646	892	1,023	9,960	189	12,790	9,786	1.31
		82	658	876	1,101	9,850	268	12,835	9,786	1.31
	average	79	643	866	1,020	9,345	173	12,125	9,284	1.31
34.00	12-9a	83	689	881	960	8,840	119	11,572	7,794	1.48
		82	688	895	988	8,870	136	11,659	7,794	1.50
	12-9b	81	702	907	991	9,360	138	12,179	8,837	1.38
		83	692	920	993	9,410	139	12,237	8,837	1.38
	average	82	693	901	983	9,120	133	11,912	8,316	1.44
34.17	12-10a	90	854	349	7,070	288	466	9,117	8,642	1.06
		90	863	397	6,900	296	479	9,025	8,642	1.04
	12-10b	92	850	316	5,120	257	476	7,111	5,625	1.26
		95	866	325	5,170	280	493	7,229	5,625	1.29
	average	92	858	347	6,065	280	479	8,121	7,133	1.16
34.33	12-11a	96	894	446	9,120	346	517	11,419	11,952	0.96
		96	900	465	9,570	377	539	11,947	11,952	1.00
	12-11b	101	950	587	12,810	429	571	15,448	18,352	0.84
		99	993	624	14,320	441	565	17,042	18,352	0.93
	average	98	934	531	11,455	398	548	13,964	15,152	0.93

Table I.4 The Concentration of Different Fe Minerals in Zone 3 determined with A Six-Step Sequential Extraction

DBS (m)	Sample Number	Ion exchangeable Fe	Siderite	Amorphous Fe	Goethite, lepidocrocite, hematite	Magnetite	Pyrite/Pyrrhotite	Total Fe	XRF	
		Fe(II) (ug/g)	Fe(II) (ug/g)	Fe(II) and Fe(III) (ug/g)	Fe(III) (ug/g)	Fe(II/III) (ug/g)	Fe(II) (ug/g)	Fe (ug/g)	ppm	ratio
48.00	19-10a	132	89	601	1,639	651	338	3,450	5,539	0.62
		132	93	601	1,849	651	348	3,673	5,539	0.66
	19-10b	132	75	601	2,003	651	332	3,794	4,476	0.85
		132	83	667	2,051	651	131	3,714	4,476	0.83
	average	132	85	618	1,886	651	287	3,658	5,007	0.74
48.17	19-11a	121	283	282	542	5,220	2	6,449	13,872	0.46
		127	303	294	538	6,214	2	7,478	13,872	0.54
	19-11b	128	235	216	489	4,886	2	5,956	7,373	0.81
		124	233	203	477	4,418	2	5,457	7,373	0.74
	average	125	264	249	511	5,185	2	6,335	10,623	0.64
48.33	20-1a	189	294	1,097	650	11,545	2	13,777	16,092	0.86
		197	286	1,103	598	12,800	2	14,986	16,092	0.93
	20-1b	166	266	1,103	624	12,120	2	14,280	15,876	0.90
		166	256	1,098	602	11,945	2	14,069	15,876	0.89
	average	180	276	1,100	618	12,103	2	14,278	15,984	0.89
48.50	20-2a	237	380	1,465	2,776	22,835	2	27,695	52,668	0.53
		239	395	1,509	2,879	25,025	2	30,050	52,668	0.57
	20-2b	246	381	1,429	2,658	22,370	2	27,086	44,394	0.61
		264	388	1,446	2,633	25,390	2	30,124	44,394	0.68
	average	247	386	1,462	2,737	23,905	2	28,739	48,531	0.60
48.67	20-3a	117	225	1,067	511	4,428	2	6,350	9,187	0.69
		124	223	1,066	499	5,156	2	7,069	9,187	0.77
	20-3a	119	217	1,058	466	4,844	2	6,706	8,024	0.84
		122	213	1,051	459	4,074	2	5,921	8,024	0.74
	average	120	219	1,061	484	4,626	2	6,512	8,605	0.76

Table I.4 The Concentration of Different Fe Minerals in Zone 3 determined with A Six-Step Sequential Extraction (Continued)

DBS (m)	Sample Number	Ion exchangeable Fe	Siderite	Amorphous Fe	Goethite, lepidocrocite, hematite	Magnetite	Pyrite/Pyrrhotite	Total Fe	XRF	
		Fe(II) (ug/g)	Fe(II) (ug/g)	Fe(II) and Fe(III) (ug/g)	Fe(III) (ug/g)	Fe(II/III) (ug/g)	Fe(II) (ug/g)	Fe (ug/g)	ppm	ratio
48.83	20-4a	118	217	241	414	4,032	2	5,024	4,703	1.07
		119	213	231	102	4,400	2	5,068	4,703	1.08
	20-4b	119	215	221	102	3,778	2	4,437	4,521	0.98
		118	214	227	102	3,900	2	4,563	4,521	1.01
	average	119	215	230	180	4,028	2	4,773	4,612	1.03
49.00	20-5a	120	248	225	102	2,002	2	2,700	4,178	0.65
		120	231	224	102	2,248	2	2,928	4,178	0.70
	20-5b	119	222	209	102	2,020	2	2,674	5,074	0.53
		116	362	226	102	2,002	2	2,811	5,074	0.55
	average	119	266	221	102	2,068	2	2,778	4,626	0.61
49.17	20-6a	213	274	502	17,550	2,872	1,010	22,422	64,338	0.35
		206	290	588	21,160	3,209	1,010	26,463	64,338	0.41
	20-6b	200	289	437	17,650	3,040	1,010	22,626	30,527	0.74
		200	262	413	15,530	2,972	1,010	20,387	30,527	0.67
	average	205	279	485	17,973	3,023	1,010	22,975	47,432	0.54
49.33	20-7a	200	227	2,029	34,210	6,628	11,020	54,314	78,817	0.69
		200	213	2,049	34,320	10,274	11,850	58,906	78,817	0.75
	20-7b	200	218	1,970	38,120	10,654	9,920	61,082	90,130	0.68
		200	219	1,957	40,950	9,081	8,301	60,708	90,130	0.67
	average	200	219	2,001	36,900	9,159	10,273	58,753	84,473	0.70
49.50	20-8a	704	100	500	358	522	3,482	5,666	12,306	0.46
		722	100	500	281	547	2,748	4,898	12,306	0.40
	20-8b	738	100	500	811	541	2,847	5,537	10,121	0.55
		729	100	500	493	565	2,620	5,008	10,121	0.49
	average	724	100	500	486	544	2,924	5,277	11,214	0.48

Table I.4 The Concentration of Different Fe Minerals in Zone 3 determined with A Six-Step Sequential Extraction (Continued)

DBS (m)	Sample Number	Ion exchangeable Fe	Siderite	Amorphous Fe	Goethite, lepidocrocite, hematite	Magnetite	Pyrite/Pyrrhotite	Total Fe	XRF	
		Fe(II) (ug/g)	Fe(II) (ug/g)	Fe(II) and Fe(III) (ug/g)	Fe(III) (ug/g)	Fe(II/III) (ug/g)	Fe(II) (ug/g)	Fe (ug/g)	ppm	ratio
49.67	20-9a	339	212	500	7,370	589	1,010	10,021	9,059	1.11
		415	218	500	6,434	580	1,010	9,157	9,059	1.01
	20-9b	367	292	1,450	7,662	600	1,010	11,382	16,006	0.71
		342	256	1,002	8,390	580	1,010	11,579	16,006	0.72
	average	366	245	863	7,464	587	1,010	10,535	12,533	0.89
49.83	20-10a	640	8,920	1,526	5,978	553	1,010	18,627	40,494	0.46
		506	11,240	2,714	3,544	500	1,010	19,514	40,494	0.48
	20-10b	807	7,200	1,332	12,620	675	1,010	23,644	26,741	0.88
		781	10,020	1,536	12,710	668	1,034	26,749	26,741	1.00
	average	684	9,345	1,777	8,713	599	1,016	22,134	33,618	0.71
50.00	20-11a	596	5,040	8,630	25,420	927	1,010	41,623	52,526	0.79
		457	4,700	8,955	30,200	1,090	1,024	46,426	52,526	0.88
	20-11b	464	4,660	9,120	15,040	649	1,023	30,956	33,295	0.93
		246	5,860	9,945	13,442	621	1,024	31,138	33,295	0.94
	average	441	5,065	9,163	21,026	822	1,020	37,536	42,911	0.89

APPENDIX J

GAS CHROMATOGRAPH DATA OF 1,4-DICHLOROBENZENE, TETRACHLOROETHYLENE, TRICHLOROETHYLENE CONCENTRATIONS

The concentrations of 1,4-dichlorobenzene, and its byproduct, chlorobenzene, benzene in the sediment slurry sample have been measured with purge and trap gas chromatograph - photoionization detector (P&T GC-PID). The peak area of these compounds was interpreted with external 5-points calibration curve. The peak area, concentration, and residual fraction for 1,4-dichlorobenzene measured by GC-MS is provided in the following Tables J.1 to J.5.

Then concentrations of tetrachloroethylene (PCE), trichlorobenzene (TCE) and its byproducts in the sediment slurry were measured in the headspace of each 40 mL sample container. The peak area, concentration, and natural logarithm values of PCE and TCE measured by gas chromatograph-mass spectrometry (GC-MS) were listed in Tables J.6 to J.15.

Table J.1 Peak Area of 1,4-Dichlorobenzene Measured by P&T GC in the Controlled Groups

		Sample Intervals (hours)						
		0	17	24	41	48	67	97
Blank	a	169,011,301	167,087,693		190,343,081		174,242,613	176,581,181
	b	188,525,004	148,713,828		192,144,431		196,582,169	188,753,327
	Average	178,768,153	157,900,761		191,243,756		185,412,391	182,667,254
Pyrite	a	188,525,004	183,685,189	197,671,359	189,872,228	177,530,577	199,480,627	190,981,816
	b	193,241,900	208,978,182	188,855,575	222,187,424	185,740,504	221,475,207	178,348,176
	Average	190,883,452	196,331,686	193,263,467	206,029,826	181,635,541	210,477,917	184,664,996
Siderite	a	193,241,900	193,791,792	190,539,718	187,602,017	212,750,456	179,717,080	218,735,323
	b	169,011,301	193,433,558	190,539,718	207,869,098	202,749,179	179,750,551	200,146,852
	Average	181,126,601	193,612,675	190,539,718	197,735,558	207,749,818	179,733,816	209,441,088

Table J.2 Concentrations of 1,4-Dichlorobenzene (mg L^{-1}) and the Residual Fraction in the Controlled Groups

		Sample Intervals (hours)						
		0	17	24	41	47.5	67	97
Blank	a	8.40	8.30		9.55		8.66	8.77
	b	9.37	7.39		9.43		9.77	9.38
	Average	8.88	7.85		9.49		9.21	9.07
	Residual fraction	1.00	0.88		1.07		1.04	1.02
Pyrite	a	9.37	9.13	9.82	11.04	8.82	9.91	9.49
	b	9.60	10.38	9.38	9.32	9.23	11.00	8.86
	Average	9.48	9.75	9.60	10.18	9.03	10.46	9.18
	Residual fraction	1.00	1.03	1.01	1.07	0.95	1.10	0.97
Siderite	a	9.60	9.63	9.47	10.33	10.57	8.93	10.87
	b	8.40	9.61	9.47	9.46	10.07	8.93	9.94
	Average	9.00	9.62	9.47	9.89	10.32	8.93	10.41
	Residual fraction	1.00	1.07	1.05	1.10	1.15	0.99	1.16

Table J.3 Peak Area of 1,4-Dichlorobenzene Measured by P&T GC in the Sediment Groups

		Sample Intervals (hours)									
		0	4	20	25	48.5	66	72	90	95	138
Upper Zone	a	226,075,692	190,117,010	189,978,805	170,938,705	179,869,328	172,226,711	143,221,954	134,110,379	119,231,723	127,880,662
	b	237,397,532	218,339,742	116,002,387	196,888,247	186,993,050	173,569,914	139,594,843	142,746,127	142,083,719	127,104,150
	Average	231,736,612	204,228,376	152,990,596	183,913,476	183,431,189	172,898,313	141,408,399	138,428,253	130,657,721	127,492,406
Zone 1a	a	237,582,175	231,169,780	176,153,168	-	168,356,538	170,244,553	146,621,974	137,565,063	131,563,900	133,426,396
	b	248,088,910	210,727,322	186,821,674	189,457,527	166,477,815	154,067,513	144,365,031	131,399,943	135,131,743	129,404,206
	Average	242,835,543	220,948,551	181,487,421	189,457,527	167,417,177	162,156,033	145,493,503	134,482,503	133,347,822	131,415,301
Zone 1b	a	224,076,858	213,030,281	195,908,419	182,983,976	171,618,960	164,182,340	147,185,093	130,359,030	124,028,186	122,618,088
	b	229,912,823	207,240,743	191,579,343	177,908,587	172,730,192	161,180,989	141,027,323	141,864,790	133,070,565	125,567,114
	Average	226,994,841	210,135,512	193,743,881	180,446,282	172,174,576	162,681,665	144,106,208	136,111,910	128,549,376	124,092,601
Zone 3	a	227,701,258	205,008,841	189,007,056	178,090,795	150,840,732	166,781,064	139,766,829	137,747,192	109,925,020	125,095,544
	b	257,353,909	235,474,353	185,014,812	195,297,460	165,898,476	155,848,848	146,160,464	140,929,398	127,840,450	125,952,803
	Average	242,527,584	220,241,597	187,010,934	186,694,128	158,369,604	161,314,956	142,963,647	139,338,295	118,882,735	125,524,174

Table J.4 Concentration of 1,4-Dichlorobenzene (mg L⁻¹) and Residual Fraction of the Sediment Groups

		Sample Intervals (hours)									
		0	4	20	25	48.5	66	72	90	95	138
Upper Zone	a	28.82	24.24	24.22	21.79	22.93	21.96	18.26	17.10	15.20	16.30
	b	30.27	27.84	14.79	25.10	23.84	22.13	17.80	18.20	18.12	16.21
	Average	29.55	26.04	19.51	23.45	23.39	22.04	18.03	17.65	16.66	16.26
	Residual fraction	1.00	0.88	0.66	0.79	0.79	0.75	0.61	0.60	0.56	0.55
Zone 1a	a	30.29	29.47	22.46	24.83	21.47	21.71	18.69	17.54	16.77	17.01
	b	31.63	26.87	23.82	24.16	21.23	19.64	18.41	16.75	17.23	16.50
	Average	30.96	28.17	23.14	24.49	21.35	20.67	18.55	17.15	17.00	16.76
	Residual fraction	1.00	0.91	0.75	0.79	0.69	0.67	0.60	0.55	0.55	0.54
Zone 1b	a	28.57	27.16	24.98	23.33	21.88	20.93	18.77	16.62	15.81	15.63
	b	29.31	26.42	24.43	22.68	22.02	20.55	17.98	18.09	16.97	16.01
	Average	28.94	26.79	24.70	23.01	21.95	20.74	18.37	17.35	16.39	15.82
	Residual fraction	1.00	0.93	0.85	0.79	0.76	0.72	0.63	0.60	0.57	0.55
Zone 3	a	29.03	26.14	24.10	22.71	19.23	21.26	17.82	17.56	14.02	15.95
	b	32.81	30.02	23.59	24.90	21.15	19.87	18.64	17.97	16.30	16.06
	Average	30.92	28.08	23.84	23.80	20.19	20.57	18.23	17.77	15.16	16.00
	Residual fraction	1.00	0.91	0.77	0.77	0.65	0.67	0.59	0.57	0.49	0.52

Table J.5 Concentration of 1,4-Dichlorobenzene in the 138 h Last Collecting Point (Directly Measured in the Aqueous Phase and Extracted from Solid Phase) from the Sediment Groups

		Sediment	Aqueous and Gas	Total
Upper Zone	a	3.91	16.30	20.21
	b	3.65	16.21	19.85
	Average	3.78	16.26	20.03
	Residual fraction	0.13	0.55	0.68
Zone 1a	a	6.22	17.01	23.23
	b	6.01	16.50	22.51
	Average	6.11	16.76	22.87
	Residual fraction	0.20	0.54	0.74
Zone 1b	a	8.35	15.63	23.99
	b	7.41	16.01	23.42
	Average	7.88	15.82	23.70
	Residual fraction	0.27	0.55	0.82
Zone 3	a	6.70	15.95	22.64
	b	6.88	16.06	22.93
	Average	6.79	16.00	22.79
	Residual fraction	0.22	0.52	0.74

Table J.6 Peak Area of Tetrachloroethylene Measured by GC-MS in the Controlled Groups

		Sample Intervals (hours)					
		0	14	21	41	65	89
Blank	a	22,851,176	21,809,766	21,525,820	21,942,490	18,711,272	20,171,489
	b	21,484,406	21,081,331	20,557,794	20,255,354	20,640,685	19,182,220
	Average	22,167,791	21,445,549	21,041,807	21,098,922	19,675,979	19,676,855
Pyrite	a	23,458,960	19,144,885	17,618,081	15,321,154	14,862,497	-
	b	16,447,415	19,782,672	17,817,306	16,866,651	17,058,203	-
	Average	19,953,188	19,463,779	17,717,694	16,093,903	15,960,350	-
Siderite	a	20,068,326	20,049,274	18,335,443	17,174,503	16,541,757	-
	b	19,340,294	19,794,163	17,306,068	17,377,279	16,752,266	-
	Average	19,704,310	19,921,719	17,820,756	17,275,891	16,647,012	-

Table J.7 Concentrations of Tetrachloroethylene (mg L⁻¹) Gas and Liquid Phase (calculated based on Henry's Law) in the Controlled Groups

		Sample Intervals (hours)					
		0	14	21	41	65	89
Blank	a	22.85	21.81	21.53	21.94	18.71	20.17
	b	21.48	21.08	20.56	20.26	20.64	19.18
	Average	22.17	21.45	21.04	21.10	19.68	19.68
Pyrite	a	23.46	19.14	17.62	15.32	14.86	-
	b	16.45	19.78	17.82	16.87	17.06	-
	Average	19.95	19.46	17.72	16.09	15.96	-
Siderite	a	20.07	20.05	18.34	17.17	16.54	-
	b	19.34	19.79	17.31	17.38	16.75	-
	Average	19.70	19.92	17.82	17.28	16.65	-

Table J.8 Peak Area of Tetrachloroethylene Measured by GC-MS in the Sediment Groups

		Sample Intervals (hours)						
		0	6	20	26	44	50.5	68
Upper Zone	a	23,395,043	20,565,168	18,748,452	19,285,678	17,751,128	16,701,571	15,335,278
	b	23,644,858	19,280,147	18,699,184	17,172,559	16,638,534	15,844,405	14,332,971
	Average	23,519,951	19,922,658	18,723,818	18,229,119	17,194,831	16,272,988	14,834,125
Zone 1a	a	24,129,994	19,169,391	18,386,638	17,182,939	17,146,565	16,143,145	16,378,817
	b	24,127,533	21,064,603	19,278,037	18,023,929	17,867,841	17,994,833	17,270,019
	Average	24,128,764	20,116,997	18,832,338	17,603,434	17,507,203	17,068,989	16,824,418
Zone 1b	a	20,918,199	18,723,510	17,367,637	17,775,635	16,073,653	15,604,003	15,778,793
	b	20,534,065	18,892,754	16,812,083	17,645,525	16,399,636	15,779,805	14,789,652
	Average	20,726,132	18,808,132	17,089,860	17,710,580	16,236,645	15,691,904	15,284,223
Zone 3	a	22,010,284	18,000,578	17,796,431	16,481,099	17,266,723	16,713,460	15,046,619
	b	24,653,996	19,740,068	18,868,751	18,307,885	19,239,966	17,601,097	15,625,235
	Average	23,332,140	18,870,323	18,332,591	17,394,492	18,253,345	17,157,279	15,335,927

Table J.9 Concentrations of Tetrachloroethylene (mg L⁻¹) in the Controlled Groups

		Sample Intervals (hours)						
		0	6	20	26	44	50.5	68
Upper Zone	a	23.40	20.57	19.75	19.29	17.75	16.70	15.34
	b	23.64	19.28	18.70	17.17	16.64	16.84	16.33
	Average	23.52	19.92	19.22	18.23	17.19	16.77	15.83
Zone 1a	a	24.13	21.04	18.75	17.18	17.15	16.70	15.34
	b	24.13	22.80	18.70	17.02	17.87	15.84	14.33
	Average	24.13	21.92	18.72	17.10	17.51	16.27	14.83
Zone 1b	a	20.92	18.72	17.37	17.78	16.07	15.60	15.78
	b	20.53	18.89	16.81	17.65	16.40	15.78	14.79
	Average	20.73	18.81	17.09	17.71	16.24	15.69	15.28
Zone 3	a	22.01	18.00	17.80	16.48	17.27	16.71	15.05
	b	24.65	19.74	18.87	18.31	19.24	17.60	15.63
	Average	23.33	18.87	18.33	17.39	18.25	17.16	15.34

Table J.10 Concentration of Tetrachloroethylene in the 68 h Last Collecting Point (Measured in the Gas, Calculated in Liquid and Extracted from Sediment) in the Sediment Groups

		Sediment	Aqueous and Gas	Total
Upper Zone	a	1.41	15.34	16.75
	b	1.70	16.33	18.04
	Average	1.56	15.83	17.39
	Residual fraction	0.07	0.67	0.74
Zone 1a	a	2.68	15.34	18.02
	b	2.11	14.33	16.44
	Average	2.40	14.83	17.23
	Residual fraction	0.10	0.61	0.71
Zone 1b	a	1.77	15.78	17.55
	b	1.58	14.79	16.37
	Average	1.67	15.28	16.96
	Residual fraction	0.08	0.74	0.82
Zone 3	a	2.38	15.05	17.42
	b	1.97	15.63	17.59
	Average	2.17	15.34	17.51
	Residual fraction	0.09	0.66	0.75

Table J.11 Peak Area of Trichloroethylene in the Gas Phase Measured by GC-MS in the Controlled Groups

		Sample Intervals (hours)					
		0	14	21	41	65	89
Blank	a	14,033,280	14,150,884	13,815,170	13,058,593	13,227,793	13,087,564
	b	13,362,849	13,145,796	13,436,264	12,936,474	12,830,277	10,556,030
	Average	13,698,065	13,648,340	13,625,717	12,997,534	13,029,035	11,821,797
Pyrite	a	13,761,375	12,140,098	11,251,838	10,576,172	10,092,048	-
	b	14,362,849	12,199,398	11,577,753	9,980,797	10,104,821	-
	Average	14,062,112	12,169,748	11,414,796	10,278,485	10,098,435	-
Siderite	a	14,110,342	12,399,631	11,168,105	10,586,890	10,785,763	-
	b	13,678,667	12,452,888	10,527,200	9,831,759	9,959,893	-
	Average	13,894,505	12,426,260	10,847,653	10,209,325	10,372,828	-

Table J.12 Concentrations of Trichloroethylene (mg L⁻¹) in Gas and Liquid Phase (calculated based on Henry's Law) of the Controlled Groups

		Sample Intervals (hours)					
		0	14	21	41	65	89
Blank	a	28.07	28.30	27.63	26.12	26.46	26.18
	b	26.73	26.29	26.87	25.87	25.66	21.11
	Average	27.40	27.30	27.25	26.00	26.06	23.64
Pyrite	a	27.52	24.28	22.50	21.15	20.78	-
	b	28.73	24.40	23.16	19.96	20.21	-
	Average	28.12	24.34	22.83	20.56	20.50	-
Siderite	a	28.22	24.80	22.34	21.17	21.57	-
	b	27.36	24.91	21.05	19.66	19.92	-
	Average	27.79	24.85	21.70	20.42	20.75	-

Table J.13 Peak Area of Trichloroethylene Measured by GC-MS in the Sediment Groups

		Sample Intervals (hours)						
		0	6	20	26	44	50.5	68
Upper Zone	a	14,009,453	11,416,330	10,669,359	11,379,818	10,748,388	9,981,314	10,126,082
	b	14,189,083	11,428,023	10,969,878	11,971,576	11,309,413	11,124,894	10,179,453
	Average	14,099,268	11,422,177	10,819,619	11,675,697	11,028,901	10,553,104	10,152,768
Zone 1a	a	14,677,157	10,521,109	11,620,334	10,532,904	10,454,255	9,931,732	9,032,670
	b	14,969,846	11,398,289	11,084,214	11,321,322	9,996,729	9,804,660	9,575,907
	Average	14,823,502	10,959,699	11,352,274	10,927,113	10,225,492	9,868,196	9,304,289
Zone 1b	a	13,653,492	9,477,090	9,887,163	9,753,550	9,349,517	9,386,212	8,367,574
	b	14,208,149	10,048,130	9,683,701	9,034,990	8,358,220	8,416,769	7,855,036
	Average	13,930,821	9,762,610	9,785,432	9,394,270	8,853,869	8,901,491	8,111,305
Zone 3	a	14,700,483	10,954,370	10,676,342	10,431,510	9,959,465	9,331,714	9,044,125
	b	14,860,361	10,780,458	11,002,901	10,363,033	9,767,859	9,781,016	9,396,039
	Average	14,780,422	10,867,414	10,839,622	10,397,272	9,863,662	9,556,365	9,220,082

Table J.14 Concentrations of Trichloroethylene (mg L⁻¹) in Gas and Liquid Phase (calculated based on Henry's Law) of the Sediment Groups

		Sample Intervals (hours)						
		0	6	20	26	44	50.5	68
Upper Zone	a	28.02	22.83	21.34	22.76	21.50	19.96	20.25
	b	28.38	24.86	22.94	23.94	22.62	22.25	20.36
	Average	28.20	23.84	22.14	23.35	22.06	21.11	20.31
Zone 1a	a	29.35	25.04	23.24	21.07	20.91	19.86	18.07
	b	29.94	22.80	22.17	22.64	19.99	19.61	19.15
	Average	29.65	23.92	22.70	21.85	20.45	19.74	18.61
Zone 1b	a	27.31	18.95	19.77	19.51	18.70	18.77	16.74
	b	28.42	20.10	19.37	18.07	16.72	16.83	15.71
	Average	27.86	19.53	19.57	18.79	17.71	17.80	16.22
Zone 3	a	29.40	21.91	21.35	20.86	19.92	19.46	18.09
	b	29.72	21.56	22.01	20.73	19.54	19.56	18.79
	Average	29.56	21.73	21.68	20.79	19.73	19.51	18.44

Table J.15 Concentration of Trichloroethylene in the 68 h Last Collecting Point (Measured in the Gas, Calculated in Liquid and Extracted from Sediment) in the Sediment Groups

		Sediment	Aqueous and Gas	Total
Upper Zone	a	1.98	20.25	22.24
	b	2.12	20.36	22.48
	Average	2.05	20.31	22.36
	Residual fraction	0.07	0.72	0.79
Zone 1a	a	2.91	18.07	20.97
	b	2.82	19.15	21.97
	Average	2.86	18.61	21.47
	Residual fraction	0.10	0.63	0.72
Zone 1b	a	3.68	16.74	20.42
	b	3.25	15.71	18.96
	Average	3.47	16.22	19.69
	Residual fraction	0.12	0.58	0.71
Zone 3	a	2.91	18.09	21.00
	b	2.41	18.79	21.20
	Average	2.66	18.44	21.10
	Residual fraction	0.09	0.62	0.71

REFERENCES

- (ATSDR), A.f.T.S.a.D.R., 1997. toxicological Profile for Tetrachloroethylene (Update), Atlanta, GA.
- Aeppli, M., Kaegi, R., Kretzschmar, R., Voegelin, A., Hofstetter, T.B., Sander, M., 2019. Electrochemical Analysis of Changes in Iron Oxide Reducibility During Abiotic Ferrihydrite Transformation into Goethite and Magnetite. *Environmental Science and Technology*, 53(7): 3568-3578.
- Ai, J., Yin, W., B. Hansen, H.C., 2019. Fast Dechlorination of Chlorinated Ethylenes by Green Rust in the Presence of Bone Char. *Environmental Science and Technology Letters*, 6(3): 191-196.
- Alfán-Guzmán, R., Ertan, H., Manefield, M., Lee, M., 2017. Isolation and Characterization of Dehalobacter Sp. Strain Tecb1 Including Identification of Tcba: A Novel Tetra- and Trichlorobenzene Reductive Dehalogenase. *Front Microbiology*, 8: 558.
- Anderson, R.T., Rooney-Varga, J.N., Gaw, C.V., Lovley, D.R., 1998. Anaerobic Benzene Oxidation in the Fe(III) Reduction Zone of Petroleum-Contaminated Aquifers. *Environmental Science and Technology*, 32(9): 1222-1229.
- Andreoni, V., Cavalca, L., Rao, M., Nocerino, G., Bernasconi, S., Dell'Amico, E., Colombo, M., Gianfreda, L., 2004. Bacterial Communities and Enzyme Activities of Paha Polluted Soils. *Chemosphere*, 57(5): 401-412.
- Atekwana, E.A., Abdel Aal, G.Z., 2015. Iron Biomineralization Controls on Geophysical Signatures of Hydrocarbon Contaminated Sediments. *Journal of Earth Science*, 26(6): 835-843.
- Audí-Miró, C., Cretnik, S., Torrentó, C., Rosell, M., Shouakar-Stash, O., Otero, N., Palau, J., Elsner, M., Soler, A., 2015. C, Cl and H Compound-Specific Isotope Analysis to Assess Natural Versus Fe(0) Barrier-Induced Degradation of Chlorinated Ethenes at a Contaminated Site. *Journal of Hazardous Materials*, 299: 747-754.
- Badea, S.-L., Stegarus, D.-I., Niculescu, V.-C., Enache, S., Soare, A., Ionete, R.-E., Gori, D., Höhener, P., 2021. Dehalogenation of A-Hexachlorocyclohexane by Iron Sulfide Nanoparticles: Study of Reaction Mechanism with Stable Carbon Isotopes and Ph Variations. *Science of The Total Environment*, 801: 149672.
- Bae, S., Kim, D., Lee, W., 2013. Degradation of Diclofenac by Pyrite Catalyzed Fenton Oxidation. *Applied Catalysis B: Environmental*, 134: 93-102.
- Bae, S., Lee, W., 2012. Enhanced Reductive Degradation of Carbon Tetrachloride by Biogenic Vivianite and Fe (II). *Geochimica et Cosmochimica Acta*, 85: 170-186.

- Bao, Y., Guo, C., Lu, G., Yi, X., Wang, H., Dang, Z., 2018. Role of Microbial Activity in Fe(II) Hydroxysulfate Mineral Transformations in an Acid Mine Drainage-Impacted Site from the Dabaoshan Mine. *Science of The Total Environment*, 616-617: 647-657.
- Bargar, J.R., Williams, K.H., Campbell, K.M., Long, P.E., Stubbs, J.E., Suvorova, E.I., Lezama-Pacheco, J.S., Alessi, D.S., Stylo, M., Webb, S.M., 2013. Uranium Redox Transition Pathways in Acetate-Amended Sediments. *Proceedings of the National Academy of Sciences*, 110(12): 4506-4511.
- Bearcock, J., Perkins, W., Dinelli, E., Wade, S., 2006. Fe (II)/Fe (III) 'Green Rust' developed within Ochreous Coal Mine Drainage Sediment in South Wales, UK. De Gruyter.
- Beckingham, L.E., Mitnick, E.H., Steefel, C.I., Zhang, S., Voltolini, M., Swift, A.M., Yang, L., Cole, D.R., Sheets, J.M., Ajo-Franklin, J.B., DePaolo, D.J., Mito, S., Xue, Z., 2016. Evaluation of Mineral Reactive Surface Area Estimates for Prediction of Reactivity of a Multi-Mineral Sediment. *Geochimica et Cosmochimica Acta*, 188: 310-329.
- Bénézech, P., Dandurand, J.L., Harrichoury, J.C., 2009. Solubility Product of Siderite (FeCO₃) as a Function of Temperature (25–250 °C). *Chemical Geology*, 265(1-2): 3-12.
- Berns, E.C., Sanford, R.A., Valocchi, A.J., Strathmann, T.J., Schaefer, C.E., Werth, C.J., 2019. Contributions of Biotic and Abiotic Pathways to Anaerobic Trichloroethene Transformation in Low Permeability Source Zones. *Journal of Contaminant Hydrology*, 224.
- Bertel, D., Peck, J., Quick, T.J., Senko, J.M., 2012a. Iron Transformations Induced by an Acid-Tolerant *Desulfosporosinus* Species. *Applied and Environmental Microbiology*, 78(1): 81-8.
- Bertel, D., Peck, J., Quick, T.J., Senko, J.M., 2012b. Iron Transformations Induced by an Acid-Tolerant *Desulfosporosinus* Species. *Applied and Environmental Microbiology*, 78(1): 81-8.
- Bishop, M.E., Dong, H., Glasser, P., Briggs, B.R., Pentrak, M., Stucki, J.W., 2020. Microbially Mediated Iron Redox Cycling of Subsurface Sediments from Hanford Site, Washington State, USA. *Chemical Geology*, 546: 119643.
- Bondici, V.F., Swerhone, G.D.W., Dynes, J.J., Lawrence, J.R., Wolfaardt, G.M., Warner, J., Korber, D.R., 2016. Biogeochemical Importance of the Bacterial Community in Uranium Waste Deposited at Key Lake, Northern Saskatchewan. *Geomicrobiology Journal*, 33(9): 807-821.

- Brennan, E., Lindsay, W., 1998. Reduction and Oxidation Effect on the Solubility and Transformation of Iron Oxides. *Soil Science Society of America Journal*, 62(4): 930-937.
- Brundrett, M., Yan, W., Velazquez, M.C., Rao, B., Jackson, W.A., 2019. Abiotic Reduction of Chlorate by Fe(II) Minerals: Implications for Occurrence and Transformation of Oxy-Chlorine Species on Earth and Mars. *ACS Earth and Space Chemistry*.
- Bruno, J., Wersin, P., Stumm, W., 1992. On the Influence of Carbonate in Mineral Dissolution: II. The Solubility of FeCO₃ (S) at 25°C and 1 Atm Total Pressure. *Geochimica et Cosmochimica Acta*, 56(3): 1149-1155.
- Burns, F., 2016. Chambers Works Update Microbial Community Profiles.
- Burt, R., Staff, S., 2014. Kellogg Soil Survey Laboratory Methods Manual. Natural Resources Conservation Services., National Soil Survey Center, Lincoln, Nebraska.
- Burton, E.D., Bush, R.T., Johnston, S.G., Sullivan, L.A., Keene, A.F., 2011. Sulfur Biogeochemical Cycling and Novel Fe–S Mineralization Pathways in a Tidally Re-Flooded Wetland. *Geochimica et Cosmochimica Acta*, 75(12): 3434-3451.
- Burton, E.D., Bush, R.T., Sullivan, L.A., Hocking, R.K., Mitchell, D.R., Johnston, S.G., Fitzpatrick, R.W., Raven, M., McClure, S., Jang, L.Y., 2009. Iron-Monosulfide Oxidation in Natural Sediments: Resolving Microbially Mediated S Transformations Using Xanes, Electron Microscopy, and Selective Extractions. *Environ Sci Technol*, 43(9): 3128-34.
- Butler, E.C., Hayes, K.F., 1999a. Kinetics of the Transformation of Trichloroethylene and Tetrachloroethylene by Iron Sulfide. *Environmental Science and Technology*, 33(12): 2021-2027.
- Butler, E.C., Hayes, K.F., 1999b. Kinetics of the Transformation of Trichloroethylene and Tetrachloroethylene by Iron Sulfide. *Environmental Science & Technology*, 33(12): 2021-2027.
- Butler, E.C., Hayes, K.F., 2000. Kinetics of the Transformation of Halogenated Aliphatic Compounds by Iron Sulfide. *Environmental Science and Technology*, 34(3): 422-429.
- Butler, E.C., Hayes, K.F., 2001. Factors Influencing Rates and Products in the Transformation of Trichloroethylene by Iron Sulfide and Iron Metal. *Environmental Science and Technology*, 35(19): 3884-3891.
- Buzas-Stephens, P., Buzas, M.A., Price, J.D., Courtney, C.H., 2018. Benthic Superheroes: Living Foraminifera from Three Bays in the Mission-Aransas National Estuarine Research Reserve, USA. *Estuaries and Coasts*, 41(8): 2368-2377.

- Canfield, D.E., Raiswell, R., Bottrell, S.H., 1992. The Reactivity of Sedimentary Iron Minerals toward Sulfide. *American Journal of Science*, 292(9): 659-683.
- Cao, J., Xu, R., Tang, H., Tang, S., Cao, M., 2011. Synthesis of Monodispersed Cmc-Stabilized Fe–Cu Bimetal Nanoparticles for in Situ Reductive Dechlorination of 1, 2, 4-Trichlorobenzene. *Science of The Total Environment*, 409(11): 2336-2341.
- Carpenter, J., Bi, Y., Hayes, K.F., 2015. Influence of Iron Sulfides on Abiotic Oxidation of Uo₂ by Nitrite and Dissolved Oxygen in Natural Sediments. *Environmental Science and Technology*, 49(2): 1078-1085.
- Chapelle, F.H., Haack, S.K., Adriaens, P., Henry, M.A., Bradley, P.M., 1996. Comparison of E(H) and H₂ Measurements for Delineating Redox Processes in a Contaminated Aquifer. *Environmental Science and Technology*, 30(12): 3565-3569.
- Chen, H., Lai, Y., Lu, H., Liang, J., Lu, J., Fang, Y., 2018. Study on Authigenic Pyrite in Sediments of Gas Hydrate Geo-System in the Shenhu Area, South China Sea. *Haiyang Xuebao*, 40(7): 116-133.
- Chen, K., Liu, Z., Wang, X., Yu, C., Ye, J., Yu, C., Wang, F., Shen, C., 2021. Enhancement of Perchloroethene Dechlorination by a Mixed Dechlorinating Culture Via Magnetic Nanoparticle-Mediated Isolation Method. *Science of The Total Environment*, 786.
- Chen, L.-H., Huang, C.-C., Lien, H.-L., 2008. Bimetallic Iron–Aluminum Particles for Dechlorination of Carbon Tetrachloride. *Chemosphere*, 73(5): 692-697.
- Cherry, J.A., Shaikh, A.U., Tallman, D.E., Nicholson, R.V., 1979. Arsenic Species as an Indicator of Redox Conditions in Groundwater. *Journal of Hydrology*, 43(1-4): 373-392.
- Choi, J., Batchelor, B., Chung, J., 2010. Reductive Dechlorination of Tetrachloroethylene by Green Rusts Modified with Copper. *Water, Air, and Soil Pollution*, 212(1): 407-417.
- Choi, J., Choi, K., Lee, W., 2009. Effects of Transition Metal and Sulfide on the Reductive Dechlorination of Carbon Tetrachloride and 1, 1, 1-Trichloroethane by Fes. *Journal of Hazardous Materials*, 162(2-3): 1151-1158.
- Choi, K., Lee, W., 2009. Reductive Dechlorination of Carbon Tetrachloride in Acidic Soil Manipulated with Iron (Ii) and Bisulfide Ion. *Journal of Hazardous Materials*, 172(2-3): 623-630.
- Claff, S.R., Sullivan, L.A., Burton, E.D., Bush, R.T., 2010. A Sequential Extraction Procedure for Acid Sulfate Soils: Partitioning of Iron. *Geoderma*, 155(3-4): 224-230.

- Cooper, D.C., Morse, J.W., 1998. Extractability of Metal Sulfide Minerals in Acidic Solutions: Application to Environmental Studies of Trace Metal Contamination within Anoxic Sediments. *Environmental Science and Technology*, 32(8): 1076-1078.
- Cornell, R.M., Schwertmann, U., 2003. *The Iron Oxides: Structure, Properties, Reactions, Occurrences, and Uses*, 2. Wiley-vch Weinheim.
- Cornwell, J.C., Morse, J.W., 1987. The Characterization of Iron Sulfide Minerals in Anoxic Marine Sediments. *Marine chemistry*, 22(2-4): 193-206.
- Cowan, E.A., Epperson, E.E., Seramur, K.C., Brachfeld, S.A., Hageman, S.J., 2017. Magnetic Susceptibility as a Proxy for Coal Ash Pollution within Riverbed Sediments in a Watershed with Complex Geology (Southeastern USA). *Environmental Earth Sciences*, 76(19).
- Culpepper, J.D., Scherer, M., Robinson, T.C., Neumann, A., Cwiertny, D., Latta, D.E., 2018. Reduction of Pce and Tce by Magnetite Revisited. *Environmental Science: Processes and Impacts*, 20(10): 1340-1349.
- Czimmerová, M., Vološčuková, O., Marková, K., Ševců, A., Černík, M., Nosek, J., 2020. Combining Nanoscale Zero-Valent Iron with Electrokinetic Treatment for Remediation of Chlorinated Ethenes and Promoting Biodegradation: A Long-Term Field Study. *Water Research*, 175.
- De Wildeman, S., Verstraete, W., 2003. The Quest for Microbial Reductive Dechlorination of C₂ to C₄ Chloroalkanes Is Warranted. *Applied Microbiology and Biotechnology*, 61(2): 94-102.
- Diakonov, I.I., Schott, J., Martin, F., Harrichourry, J.-C., Escalier, J., 1999. Iron(II) Solubility and Speciation in Aqueous Solutions. *Experimental Study and Modelling: Part 1. Hematite Solubility from 60 to 300°C in NaOH–NaCl Solutions and Thermodynamic Properties of Fe(OH)₄–(Aq)*. *Geochimica et Cosmochimica Acta*, 63(15): 2247-2261.
- DiStefano, V.H., McFarlane, J., Anovitz, L.M., Stack, A.G., Gordon, A.D., Littrell, K.C., Chipera, S.J., Hunt, R.D., Lewis, S.A., Hale, R.E., Perfect, E., 2016. Extraction of Organic Compounds from Representative Shales and the Effect on Porosity. *Journal of Natural Gas Science and Engineering*, 35: 646-660.
- Đordjević, S., Ishiyama, D., Ogawa, Y., Stevanović, Z., 2018. Mobility and Natural Attenuation of Metals and Arsenic in Acidic Waters of the Drainage System of Timok River from Bor Copper Mines (Serbia) to Danube River. *Environmental Science and Pollution Research*, 25(25): 25005-25019.
- Dos Santos Afonso, M., Stumm, W., 1992. Reductive Dissolution of Iron (II) (Hydr) Oxides by Hydrogen Sulfide. *Langmuir*, 8(6): 1671-1675.

- Driessen, R., Zhao, F., Hofmann, S., Bouten, C., Sahlgren, C., Stassen, O., 2020. Computational Characterization of the Dish-in-a-Dish, a High Yield Culture Platform for Endothelial Shear Stress Studies on the Orbital Shaker. *Micromachines*, 11(6): 552.
- Du Laing, G., Rinklebe, J., Vandecasteele, B., Meers, E., Tack, F.M., 2009. Trace Metal Behaviour in Estuarine and Riverine Floodplain Soils and Sediments: A Review. *Science of The Total Environment*, 407(13): 3972-3985.
- Dupont, 2006. Operational History (Internal Report).
- Eberle, D., Bastian, D., Ebel, N., Schwarz, R., 2017. Locating Hidden Channels for Placer Gold Exploration in the Cariboo District, British Columbia, Canada: A Case Study. *Journal of Applied Geophysics*, 136: 61-79.
- Edwards, K.J., Bond, P.L., Gihring, T.M., Banfield, J.F., 2000. An Archaeal Iron-Oxidizing Extreme Acidophile Important in Acid Mine Drainage. *Science*, 287(5459): 1796.
- Elliott, D.W., Lien, H.L., Zhang, W.X., 2009. Degradation of Lindane by Zero-Valent Iron Nanoparticles. *Journal of Environmental Engineering*, 135(5): 317-324.
- Elsner, M., Schwarzenbach, R.P., Haderlein, S.B., 2004. Reactivity of Fe(II)-Bearing Minerals toward Reductive Transformation of Organic Contaminants. *Environmental Science and Technology*, 38(3): 799-807.
- Emmerson, R.H., Birkett, J.W., Scrimshaw, M., Lester, J.N., 2000. Solid Phase Partitioning of Metals in Managed Retreat Soils: Field Changes over the First Year of Tidal Inundation. *Science of The Total Environment*, 254(1): 75-92.
- Entwistle, J., Latta, D.E., Scherer, M.M., Neumann, A., 2019. Abiotic Degradation of Chlorinated Solvents by Clay Minerals and Fe(II): Evidence for Reactive Mineral Intermediates. *Environmental Science and Technology*, 53(24): 14308-14318.
- Ergin, M., Karakaş, Z.S., Tekin, E., Eser, B., Sözeri, K., Çopuroğlu, İ., Koç, Ş., Şimşek, B., 2018. Provenance Discrimination among Foreshore, Backshore, and Dune Environments in the Black Sand Beaches Along the Samandağ/Hatay Coasts, Se Turkey (E Mediterranean). *Arabian Journal of Geosciences*, 11(6).
- Eriksson, M., Sodersten, E., Yu, Z., Dalhammar, G., Mohn, W.W., 2003. Degradation of Polycyclic Aromatic Hydrocarbons at Low Temperature under Aerobic and Nitrate-Reducing Conditions in Enrichment Cultures from Northern Soils. *Applied and environmental microbiology*, 69(1): 275-284.
- Faulkner, L.R., Bard, A.J., 2002. *Electrochemical Methods: Fundamentals and Applications*. John Wiley and Sons.

- Ferrey, M.L., Wilkin, R.T., Ford, R.G., Wilson, J.T., 2004. Nonbiological Removal of Cis-Dichloroethylene and 1,1-Dichloroethylene in Aquifer Sediment Containing Magnetite. *Environmental Science and Technology*, 38(6): 1746-1752.
- Finck, N., Bouby, M., Dardenne, K., 2019. Fate of Lu(III) Sorbed on 2-Line Ferrihydrite at Ph 5.7 and Aged for 12 years at Room Temperature. I: Insights from Icp-Oes, Xrd, Esem, Asflfff/Icp-MS, and Exafs Spectroscopy. *Environmental Science and Pollution Research*, 26(6): 5238-5250.
- Flyhammar, P., 1998. Use of Sequential Extraction on Anaerobically Degraded Municipal Solid Waste. *Science of The Total Environment*, 212(2-3): 203-215.
- Ford, R.G., Bertsch, P.M., Farley, K.J., 1997. Changes in Transition and Heavy Metal Partitioning During Hydrous Iron Oxide Aging. *Environmental Science and Technology*, 31(7): 2028-2033.
- Fung, J.M., Weisenstein, B.P., Mack, E.E., Vidumsky, J.E., Ei, T.A., Zinder, S.H., 2009. Reductive Dehalogenation of Dichlorobenzenes and Monochlorobenzene to Benzene in Microcosms. *Environmental Science and Technology*, 43(7): 2302-2307.
- Gander, J.W., Parkin, G.F., Scherer, M.M., 2002. Kinetics of 1, 1, 1-Trichloroethane Transformation by Iron Sulfide and a Methanogenic Consortium. *Environmental Science and Technology*, 36(21): 4540-4546.
- Gao, P., Sun, X., Xiao, E., Xu, Z., Li, B., Sun, W., 2019. Characterization of Iron-Metabolizing Communities in Soils Contaminated by Acid Mine Drainage from an Abandoned Coal Mine in Southwest China. *Environmental Science and Pollution Research*, 26(10): 9585-9598.
- Gao, S., Seo, J.-S., Wang, J., Keum, Y.-S., Li, J., Li, Q.X., 2013. Multiple Degradation Pathways of Phenanthrene by *Stenotrophomonas maltophilia* C6. *International Biodeterioration and Biodegradation*, 79: 98-104.
- Garcia-Cervilla, R., Santos, A., Romero, A., Lorenzo, D., 2022. Abatement of Chlorobenzenes in Aqueous Phase by Persulfate Activated by Alkali Enhanced by Surfactant Addition. *Journal of Environmental Management*, 306: 114475.
- Garcia, A.N., Zhang, Y., Ghoshal, S., He, F., O'Carroll, D.M., 2021. Recent Advances in Sulfidated Zerovalent Iron for Contaminant Transformation. *Environmental Science & Technology*, 55(13): 8464-8483.
- Gardner, J., Tatterson, G., 1992. Characterization of Mixing in Shaker Table Containers. *Biotechnology and Bioengineering*, 39(7): 794-797.

- Geelhoed, J.S., Sorokin, D.Y., Epping, E., Tourova, T.P., Banciu, H.L., Muyzer, G., Stams, A.J., van Loosdrecht, M.C., 2009. Microbial Sulfide Oxidation in the Oxic-Anoxic Transition Zone of Freshwater Sediment: Involvement of Lithoautotrophic *Magnetospirillum* Strain J10. *FEMS Microbiol Ecol*, 70(1): 54-65.
- Goltz, M.N., Park, J.-W., Feng, P.P., Young, H.C., 2005. *Organic Chemicals in Groundwater: Modeling Fate and Transport, Water Pollution*. Springer, pp. 33-63.
- Gorny, J., Billon, G., Noiriél, C., Dumoulin, D., Lesven, L., Madé, B., 2018. Redox Behaviour of Arsenic in the Surface Sediments of the Marque River (Northern France). *Journal of Geochemical Exploration*, 188: 111-122.
- Gorski, C.A., Aeschbacher, M., Soltermann, D., Voegelin, A., Baeyens, B., Marques Fernandes, M., Hofstetter, T.B., Sander, M., 2012a. Redox Properties of Structural Fe in Clay Minerals. 1. Electrochemical Quantification of Electron-Donating and-Accepting Capacities of Smectites. *Environmental Science and Technology*, 46(17): 9360-9368.
- Gorski, C.A., Klupfel, L., Voegelin, A., Sander, M., Hofstetter, T.B., 2012b. Redox Properties of Structural Fe in Clay Minerals. 2. Electrochemical and Spectroscopic Characterization of Electron Transfer Irreversibility in Ferruginous Smectite, Swa-1. *Environmental Science and Technology*, 46(17): 9369-77.
- Gorski, C.A., Klupfel, L., Voegelin, A., Sander, M., Hofstetter, T.B., 2012c. Redox Properties of Structural Fe in Clay Minerals. 2. Electrochemical and Spectroscopic Characterization of Electron Transfer Irreversibility in Ferruginous Smectite, Swa-1. *Environmental Science & Technology*, 46(17): 9369-9377.
- Gorski, C.A., Nurmi, J.T., Tratnyek, P.G., Hofstetter, T.B., Scherer, M.M., 2009. Redox Behavior of Magnetite: Implications for Contaminant Reduction. *Environmental Science and Technology*, 44(1): 55-60.
- Green, D.W., Perry, R.H., 2008. *Perry's Chemical Engineers' Handbook*. McGraw-Hill Education.
- Grenthe, I., Stumm, W., Laaksuharju, M., Nilsson, A.C., Wikberg, P., 1992. Redox Potentials and Redox Reactions in Deep Groundwater Systems. *Chemical Geology*, 98(1): 131-150.
- Griffioen, J., Klaver, G., Westerhoff, W.E., 2016. The Mineralogy of Suspended Matter, Fresh and Cenozoic Sediments in the Fluvio-Deltaic Rhine-Meuse-Scheldt-Ems Area, the Netherlands: An Overview and Review. *Geologie en Mijnbouw/Netherlands Journal of Geosciences*, 95(1): 23-107.
- Gruner, W., Kunath, J., Kalnishevskaja, L.N., Posokin, J.V., Brainina, K.Z., 1993. Fundamentals and Limitations for the Application of the Carbon Paste Electroactive Electrode in the Electroanalysis of Solids. *Electroanalysis*, 5(3): 243-250.

- Grygar, T., 1995. Kinetics of Electrochemical Reductive Dissolution of Iron (Iii) Hydroxy-Oxides. *Collection of Czechoslovak chemical communications*, 60(8): 1261-1273.
- Han, Y., Yan, W., 2016. Reductive Dechlorination of Trichloroethene by Zero-Valent Iron Nanoparticles: Reactivity Enhancement through Sulfidation Treatment. *Environmental Science and Technology*, 50(23): 12992-13001.
- He, Y., Su, C., Wilson, J., Wilkin, R., Adair, C., Lee, T., Bradley, P., Ferrey, M., 2009. Identification and Characterization Methods for Reactive Minerals Responsible for Natural Attenuation of Chlorinated Organic Compounds in Ground Water. U.S. EPA(EPA/600/R-09/115).
- He, Y., Wilson, J., Su, C., Wilkin, R., 2015. Review of Abiotic Degradation of Chlorinated Solvents by Reactive Iron Minerals in Aquifers. *Groundwater Monitoring and Remediation*, 35(3): 57-75.
- He, Y.T., Wilson, J.T., Wilkin, R.T., 2010. Impact of Iron Sulfide Transformation on Trichloroethylene Degradation. *Geochimica et Cosmochimica Acta*, 74(7): 2025-2039.
- Herbel, M., Suarez, D., Goldberg, S., Gao, S., 2007. Evaluation of Chemical Amendments for Ph and Redox Stabilization in Aqueous Suspensions of Three California Soils. *Soil Science Society of America Journal*, 71(3): 927-939.
- Heron, G., Crouzet, C., Bourg, A.C., Christensen, T.H., 1994. Speciation of Fe(Ii) and Fe(Iii) in Contaminated Aquifer Sediments Using Chemical Extraction Techniques. *Environmental Science and Technology*, 28(9): 1698-705.
- Holliger, C., Regard, C., Diekert, G., 2003. Dehalogenation by Anaerobic Bacteria. *Dehalogenation: Microbial Processes and Environmental Applications* (Häggblom Mm & Bossert Id, Eds). Kluwer Academic Publishers, Boston, MA.
- Holmes, D.E., Finneran, K.T., O'Neil, R.A., Lovley, D.R., 2002. Enrichment of Members of the Family Geobacteraceae Associated with Stimulation of Dissimilatory Metal Reduction in Uranium-Contaminated Aquifer Sediments. *Applied and Environmental Microbiology*, 68(5): 2300-2306.
- Hoving, A.L., Sander, M., Bruggeman, C., Behrends, T., 2017. Redox Properties of Clay-Rich Sediments as Assessed by Mediated Electrochemical Analysis: Separating Pyrite, Siderite and Structural Fe in Clay Minerals. *Chemical geology*, 457: 149-161.
- Hua, H., Yin, X., Dyer, J.A., Landis, R., Axe, L., 2020. Characterizing Reactive Iron Mineral Coatings in Redox Transition Zones. *ACS Earth and Space Chemistry*, 4(12): 2337-2346.

- Huang, J., Jones, A., Waite, T.D., Chen, Y., Huang, X., Rosso, K.M., Kappler, A., Mansor, M., Tratnyek, P.G., Zhang, H., 2021. Fe(II) Redox Chemistry in the Environment. *Chemical Reviews*, 121(13): 8161-8233.
- Huang, K.-C., Zhao, Z., Hoag, G.E., Dahmani, A., Block, P.A., 2005. Degradation of Volatile Organic Compounds with Thermally Activated Persulfate Oxidation. *Chemosphere*, 61(4): 551-560.
- Hyun, S.P., Hayes, K.F., 2015. Abiotic Reductive Dechlorination of Cis-Dce by Ferrous Monosulfide Mackinawite. *Environmental Science and Pollution Research*, 22(21): 16463-16474.
- Iker, B.C., Bright, K.R., Pepper, I.L., Gerba, C.P., Kitajima, M., 2013. Evaluation of Commercial Kits for the Extraction and Purification of Viral Nucleic Acids from Environmental and Fecal Samples. *Journal of Virological Methods*, 191(1): 24-30.
- Ikkert, O.P., Gerasimchuk, A.L., Bukhtiyarova, P.A., Tuovinen, O.H., Karnachuk, O.V., 2013. Characterization of Precipitates Formed by H₂S-Producing, Cu-Resistant *Firmicute* Isolates of *Tissierella* from Human Gut and *Desulfosporosinus* from Mine Waste. *Antonie van Leeuwenhoek*, 103(6): 1221-34.
- Ikogou, M., Ona-Nguema, G., Juillot, F., Le Pape, P., Menguy, N., Richeux, N., Guigner, J.M., Noël, V., Brest, J., Baptiste, B., Morin, G., 2017. Long-Term Sequestration of Nickel in Mackinawite Formed by *Desulfovibrio Capillatus* Upon Fe(III)-Citrate Reduction in the Presence of Thiosulfate. *Applied Geochemistry*, 80: 143-154.
- Islam, F.S., Gault, A.G., Boothman, C., Polya, D.A., Charnock, J.M., Chatterjee, D., Lloyd, J.R., 2004. Role of Metal-Reducing Bacteria in Arsenic Release from Bengal Delta Sediments. *Nature*, 430(6995): 68-71.
- Islam, F.S., Pederick, R.L., Gault, A.G., Adams, L.K., Polya, D.A., Charnock, J.M., Lloyd, J.R., 2005. Interactions between the Fe(II)-Reducing Bacterium *Geobacter Sulfurreducens* and Arsenate, and Capture of the Metalloid by Biogenic Fe(II). *Applied and Environmental Microbiology*, 71(12): 8642-8648.
- Ivanov, V., Stabnikov, V., Zhuang, W.Q., Tay, J.H., Tay, S.T., 2005. Phosphate Removal from the Returned Liquor of Municipal Wastewater Treatment Plant Using Iron-Reducing Bacteria. *Journal of Applied Microbiology*, 98(5): 1152-61.
- Janot, N., Lezama Pacheco, J.S., Pham, D.Q., O'Brien, T.M., Hausladen, D., Noël, V., Lallier, F., Maher, K., Fendorf, S., Williams, K.H., Long, P.E., Bargar, J.R., 2016. Physico-Chemical Heterogeneity of Organic-Rich Sediments in the Rifle Aquifer, Co: Impact on Uranium Biogeochemistry. *Environmental Science and Technology*, 50(1): 46-53.
- Jeong, H.Y., Hayes, K.F., 2007. Reductive Dechlorination of Tetrachloroethylene and Trichloroethylene by Mackinawite (FeS) in the Presence of Metals: Reaction Rates. *Environmental Science and Technology*, 41(18): 6390-6396.

- Jeong, H.Y., Kim, H., Hayes, K.F., 2007. Reductive Dechlorination Pathways of Tetrachloroethylene and Trichloroethylene and Subsequent Transformation of Their Dechlorination Products by Mackinawite (FeS) in the Presence of Metals. *Environmental Science and Technology*, 41(22): 7736-7743.
- Jeong, H.Y., Lee, J.H., Hayes, K.F., 2008. Characterization of Synthetic Nanocrystalline Mackinawite: Crystal Structure, Particle Size, and Specific Surface Area. *Geochimica et Cosmochimica Acta*, 72(2): 493-505.
- Jian, R.-S., Sung, L.-Y., Lu, C.-J., 2014. Measuring Real-Time Concentration Trends of Individual Voc in an Elementary School Using a Sub-Ppb Detection Mgc and a Single Gc–Ms Analysis. *Chemosphere*, 99: 261-266.
- Johnson, C.A., Freyer, G., Fabisch, M., Caraballo, M.A., Küsel, K., Hochella Jr, M.F., 2014. Observations and Assessment of Iron Oxide and Green Rust Nanoparticles in Metal-Polluted Mine Drainage within a Steep Redox Gradient. *Environmental Chemistry*, 11(4): 377-391.
- Johnson, D.B., Ghauri, M., McGinness, S., 1993. Biogeochemical Cycling of Iron and Sulphur in Leaching Environments. *Federation of European Microbiological Societies Microbiology Reviews*, 11(1-3): 63-70.
- Johnson, D.B., Okibe, N., Roberto, F.F., 2003. Novel Thermo-Acidophilic Bacteria Isolated from Geothermal Sites in Yellowstone National Park: Physiological and Phylogenetic Characteristics. *Archives of Microbiology*, 180(1): 60-8.
- Johnson, T.L., Scherer, M.M., Tratnyek, P.G., 1996. Kinetics of Halogenated Organic Compound Degradation by Iron Metal. *Environmental Science and Technology*, 30(8): 2634-2640.
- Jones, E.J., Nadeau, T.L., Voytek, M.A., Landa, E.R., 2006. Role of Microbial Iron Reduction in the Dissolution of Iron Hydroxysulfate Minerals. *Journal of Geophysical Research: Biogeosciences*, 111(G1).
- Jonsson, S., Skjellberg, U., Nilsson, M.B., Westlund, P.O., Shchukarev, A., Lundberg, E., Björn, E., 2012. Mercury Methylation Rates for Geochemically Relevant Hg^{II} Species in Sediments. *Environmental Science and Technology*, 46(21): 11653-11659.
- Jordan, A., Stoy, P., Sneddon, H.F., 2021. Chlorinated Solvents: Their Advantages, Disadvantages, and Alternatives in Organic and Medicinal Chemistry. *Chemical Reviews*, 121(3): 1582-1622.
- Jurkevitch, E., Hadar, Y., Chen, Y., 1992. Differential Siderophore Utilization and Iron Uptake by Soil and Rhizosphere Bacteria. *Applied and Environmental Microbiology*, 58(1): 119-124.

- Kappler, A., Newman, D.K., 2004. Formation of Fe (Iii)-Minerals by Fe (Ii)-Oxidizing Photoautotrophic Bacteria. *Geochimica et Cosmochimica Acta*, 68(6): 1217-1226.
- Katsenovich, Y.P., Miralles-Wilhelm, F.R., 2009. Evaluation of Nanoscale Zerovalent Iron Particles for Trichloroethene Degradation in Clayey Soils. *Science of The Total Environment*, 407(18): 4986-4993.
- Kenneke, J.F., Weber, E.J., 2003. Reductive Dehalogenation of Halomethanes in Iron- and Sulfate-Reducing Sediments. 1. Reactivity Pattern Analysis. *Environmental Science and Technology*, 37(4): 713-720.
- Kerin, E.J., Gilmour, C.C., Roden, E., Suzuki, M.T., Coates, J.D., Mason, R.P., 2006. Mercury Methylation by Dissimilatory Iron-Reducing Bacteria. *Applied and Environmental Microbiology*, 72(12): 7919-21.
- Kestin, J., Sokolov, M., Wakeham, W.A., 1978. Viscosity of Liquid Water in the Range— 8 C to 150 C. *Journal of Physical and Chemical Reference Data*, 7(3): 941-948.
- Khoeurn, K., Sakaguchi, A., Tomiyama, S., Igarashi, T., 2019. Long-Term Acid Generation and Heavy Metal Leaching from the Tailings of Shimokawa Mine, Hokkaido, Japan: Column Study under Natural Condition. *Journal of Geochemical Exploration*, 201: 1-12.
- Khongkhaem, P., Intasiri, A., Luepromchai, E., 2011. Silica-Immobilized Methylobacterium Sp. Np3 and Acinetobacter Sp. Pk1 Degrade High Concentrations of Phenol. *Letters in Applied Microbiology*, 52(5): 448-455.
- Kim, E.-J., Murugesan, K., Kim, J.-H., Tratnyek, P.G., Chang, Y.-S., 2013. Remediation of Trichloroethylene by Fe-Coated Iron Nanoparticles in Simulated and Real Groundwater: Effects of Water Chemistry. *Industrial & Engineering Chemistry Research*, 52(27): 9343-9350.
- Kinnaird, J.A., Yudovskaya, M., McCreesh, M., Huthmann, F., Botha, T.J., 2017. The Waterberg Platinum Group Element Deposit: Atypical Mineralization in Mafic-Ultramafic Rocks of the Bushveld Complex, South Africa. *Economic Geology*, 112(6): 1367-1394.
- Klueglein, N., Kappler, A., 2013. Abiotic Oxidation of Fe(Ii) by Reactive Nitrogen Species in Cultures of the Nitrate-Reducing Fe(Ii) Oxidizer *Acidovorax* Sp. Bofen1 - Questioning the Existence of Enzymatic Fe(Ii) Oxidation. *Geobiology*, 11(2): 180-90.
- Klueglein, N., Zeitvogel, F., Stierhof, Y.D., Floetenmeyer, M., Konhauser, K.O., Kappler, A., Obst, M., 2014. Potential Role of Nitrite for Abiotic Fe(Ii) Oxidation and Cell Encrustation During Nitrate Reduction by Denitrifying Bacteria. *Applied and Environmental Microbiology*, 80(3): 1051-1061.

- Kocur, C.M.D., Fan, D., Tratnyek, P.G., Johnson, R.L., 2020. Predicting Abiotic Reduction Rates Using Cryogenically Collected Soil Cores and Mediated Reduction Potential Measurements. *Environmental Science and Technology Letters*, 7(1): 20-26.
- Kotopoulou, E., Godelitsas, A., Göttlicher, J., Steininger, R., Price, R., Fike, D.A., Amend, J.P., Gilhooly, W.P., Druschell, G., Nomikou, P., Gamaletsos, P.N., Lozios, S., 2022. Metastable Iron (Mono)Sulfides in the Shallow-Sea Hydrothermal Sediments of Milos, Greece. *ACS Earth and Space Chemistry*.
- Kozich, J.J., Westcott, S.L., Baxter, N.T., Highlander, S.K., Schloss, P.D., 2013. Development of a Dual-Index Sequencing Strategy and Curation Pipeline for Analyzing Amplicon Sequence Data on the Miseq Illumina Sequencing Platform. *Applied and Environmental Microbiology*, 79(17): 5112-5120.
- Kumar, N., Millot, R., Battaglia-Brunet, F., Omoregie, E., Chaurand, P., Borschneck, D., Bastiaens, L., Rose, J., 2016. Microbial and Mineral Evolution in Zero Valent Iron-Based Permeable Reactive Barriers During Long-Term Operations. *Environmental Science and Pollution Research*, 23(6): 5960-8.
- Kurt, Z., Spain, J.C., 2013. Biodegradation of Chlorobenzene, 1,2-Dichlorobenzene, and 1,4-Dichlorobenzene in the Vadose Zone. *Environmental Science and Technology*, 47(13): 6846-6854.
- Küsel, K., Dorsch, T., Acker, G., Stackebrandt, E., Drake, H.L., 2000. *Clostridium Scatologenes* Strain S11 Isolated as an Acetogenic Bacterium from Acidic Sediments. *International Journal of Systematic and Evolutionary Microbiology*, 50(2): 537-546.
- Küsel, K., Pinkart, H.C., Drake, H.L., Devereux, R., 1999. Acetogenic and Sulfate-Reducing Bacteria Inhabiting the Rhizoplane and Deep Cortex Cells of the Sea Grass *Halodule Wrightii*. *Applied and Environmental Microbiology*, 65(11): 5117-5123.
- Landis, R., Hua, H., Yin, X., Axe, L., Morgan, S., 2021. Biogeochemical Coring and Preservation Method for Unconsolidated Soil Samples. *Groundwater Monitoring and Remediation*, 41(3): 72-81.
- Larner, B.L., Seen, A.J., Townsend, A.T., 2006. Comparative Study of Optimised Bcr Sequential Extraction Scheme and Acid Leaching of Elements in the Certified Reference Material Nist 2711. *Analytica Chimica Acta*, 556(2): 444-449.
- Lawrence, S.J., 2006. Description, Properties, and Degradation of Selected Volatile Organic Compounds Detected in Ground Water--a Review of Selected Literature. Open-File Report(2006-1338).
- Lee, W., Batchelor, B., 2002a. Abiotic Reductive Dechlorination of Chlorinated Ethylenes by Iron-Bearing Soil Minerals. 1. Pyrite and Magnetite. *Environmental Science and Technology*, 36(23): 5147-5154.

- Liang, X., Dong, Y., Kuder, T., Krumholz, L.R., Philp, R.P., Butler, E.C., 2007a. Distinguishing Abiotic and Biotic Transformation of Tetrachloroethylene and Trichloroethylene by Stable Carbon Isotope Fractionation. *Environmental Science & Technology*, 41(20): 7094-7100.
- Liang, X., Dong, Y., Kuder, T., Krumholz, L.R., Philp, R.P., Butler, E.C., 2007b. Distinguishing Abiotic and Biotic Transformation of Tetrachloroethylene and Trichloroethylene by Stable Carbon Isotope Fractionation. *Environmental Science and Technology*, 41(20): 7094-7100.
- Liang, X., Howlett, M.R., Nelson, J.L., Grant, G., Dworatzek, S., Lacrampe-Couloume, G., Zinder, S.H., Edwards, E.A., Sherwood Lollar, B., 2011. Pathway-Dependent Isotope Fractionation During Aerobic and Anaerobic Degradation of Monochlorobenzene and 1,2,4-Trichlorobenzene. *Environmental Science and Technology*, 45(19): 8321-8327.
- Liang, X., Paul Philp, R., Butler, E.C., 2009. Kinetic and Isotope Analyses of Tetrachloroethylene and Trichloroethylene Degradation by Model Fe(II)-Bearing Minerals. *Chemosphere*, 75(1): 63-69.
- Lindsay, W.L., 1988. Solubility and Redox Equilibria of Iron Compounds in Soils, *Iron in Soils and Clay Minerals*. Springer, pp. 37-62.
- Liu, X., Peng, P.a., Fu, J., Huang, W., 2003. Effects of Fes on the Transformation Kinetics of Γ -Hexachlorocyclohexane. *Environmental Science and Technology*, 37(9): 1822-1828.
- Lovley, D.R., 1991. Dissimilatory Fe (Iii) and Mn (Iv) Reduction. *Microbiological Reviews*, 55(2): 259-287.
- Lovley, D.R., Anderson, R.T., 2000. Influence of Dissimilatory Metal Reduction on Fate of Organic and Metal Contaminants in the Subsurface. *Hydrogeology Journal*, 8(1): 77-88.
- Lovley, D.R., Holmes, D.E., Nevin, K.P., 2004. Dissimilatory Fe(Iii) and Mn(Iv) Reduction, *Advances in Microbial Physiology*, pp. 219-286.
- Lovley, D.R., Phillips, E.J., 1986. Organic Matter Mineralization with Reduction of Ferric Iron in Anaerobic Sediments. *Applied and Environmental Microbiology*, 51(4): 683-689.
- Lu, J., Zhang, B., He, C., Borthwick, A.G.L., 2020. The Role of Natural Fe(II)-Bearing Minerals in Chemoautotrophic Chromium (VI) Bio-Reduction in Groundwater. *Journal of Hazardous Materials*, 389: 121911.
- Lu, X., Wang, W., Zhang, L., Hu, H., Xu, P., Wei, T., Tang, H., 2019. Molecular Mechanism of N,N-Dimethylformamide Degradation in *Methylobacterium* Sp. Strain Dm1. *Applied and Environmental Microbiology*, 85(12).

- Lu, Y., Xie, Q., Tang, L., Yu, J., Wang, J., Yang, Z., Fan, C., Zhang, S., 2021. The Reduction of Nitrobenzene by Extracellular Electron Transfer Facilitated by Fe-Bearing Biochar Derived from Sewage Sludge. *Journal of Hazardous Materials*, 403: 123682.
- Ma, C., Wu, Y., 2008. Dechlorination of Perchloroethylene Using Zero-Valent Metal and Microbial Community. *Environmental Geology*, 55(1): 47-54.
- Mackay, D., Boethling, R.S., 2000. *Handbook of Property Estimation Methods for Chemicals: Environmental Health Sciences*. CRC press.
- Maithreepala, R.A., Doong, R.A., 2005. Enhanced Dechlorination of Chlorinated Methanes and Ethenes by Chloride Green Rust in the Presence of Copper(II). *Environmental Science and Technology*, 39(11): 4082-4090.
- McCarty, P.L., 1997. Breathing with Chlorinated Solvents. *Science*, 276(5318): 1521-1522.
- McElhinny, M.W., McFadden, P.L., 1999. *Paleomagnetism: Continents and Oceans*, 73. Elsevier.
- Mejia, J., Roden, E.E., Ginder-Vogel, M., 2016. Influence of Oxygen and Nitrate on Fe (Hydr)Oxide Mineral Transformation and Soil Microbial Communities During Redox Cycling. *Environmental Science and Technology*, 50(7): 3580-8.
- Mergaert, J., Webb, A., Anderson, C., Wouters, A., Swings, J., 1993. Microbial Degradation of Poly(3-Hydroxybutyrate) and Poly(3-Hydroxybutyrate-Co-3-Hydroxyvalerate) in Soils. *Applied and environmental microbiology*, 59(10): 3233-3238.
- Merinero, R., Lunar, R., Somoza, L., Díaz-del-Río, V., Martínez-Frías, J., 2009. Nucleation, Growth and Oxidation of Framboidal Pyrite Associated with Hydrocarbon-Derived Submarine Chimneys: Lessons Learned from the Gulf of Cadiz. *European Journal of Mineralogy*, 21(5): 947-961.
- Monferrán, M.V., Echenique, J.R., Wunderlin, D.A., 2005. Degradation of Chlorobenzenes by a Strain of *Acidovorax Avenae* Isolated from a Polluted Aquifer. *Chemosphere*, 61(1): 98-106.
- Moran, M.J., Zogorski, J.S., Squillace, P.J., 2007. Chlorinated Solvents in Groundwater of the United States. *Environmental Science and Technology*, 41(1): 74-81.
- Muller, E.E., Hourcade, E., Louhichi-Jelail, Y., Hammann, P., Vuilleumier, S., Bringel, F., 2011. Functional Genomics of Dichloromethane Utilization in *Methylobacterium Exorquens* Dm4. *Environmental Microbiology*, 13(9): 2518-2535.
- Nayak, A.S., Veeranagouda, Y., Lee, K., Karegoudar, T.B., 2009. Metabolism of Acenaphthylene Via 1,2-Dihydroxynaphthalene and Catechol by *Stenotrophomonas* Sp. Rmsk. *Biodegradation*, 20(6): 837.

- Nelson, J.L., Jiang, J., Zinder, S.H., 2014. Dehalogenation of Chlorobenzenes, Dichlorotoluenes, and Tetrachloroethene by Three Dehalobacter Spp. *Environmental Science and Technology*, 48(7): 3776-3782.
- Nidheesh, P.V., Khatri, J., Anantha Singh, T.S., Gandhimathi, R., Ramesh, S.T., 2018. Review of Zero-Valent Aluminium Based Water and Wastewater Treatment Methods. *Chemosphere*, 200: 621-631.
- Nie, X., Liu, J., Yue, D., Zeng, X., Nie, Y., 2013. Dechlorination of Hexachlorobenzene Using Lead-Iron Bimetallic Particles. *Chemosphere*, 90(9): 2403-2407.
- Ning, J., Zheng, Y., Young, D., Brown, B., Nešić, S., 2013. Thermodynamic Study of Hydrogen Sulfide Corrosion of Mild Steel. *Corrosion*, 70(4): 375-389.
- Noël, V., Boye, K., Kukkadapu, R.K., Bone, S., Lezama Pacheco, J.S., Cardarelli, E., Janot, N., Fendorf, S., Williams, K.H., Bargar, J.R., 2017. Understanding Controls on Redox Processes in Floodplain Sediments of the Upper Colorado River Basin. *Science of The Total Environment*, 603-604: 663-675.
- Noël, V., Marchand, C., Juillot, F., Ona-Nguema, G., Viollier, E., Marakovic, G., Olivi, L., Delbes, L., Gelebart, F., Morin, G., 2014. EXAFS Analysis of Iron Cycling in Mangrove Sediments Downstream a Lateritized Ultramafic Watershed (Vavouto Bay, New Caledonia). *Geochimica et Cosmochimica Acta*, 136: 211-228.
- Nunez Garcia, A., Boparai, H.K., Chowdhury, A.I.A., de Boer, C.V., Kocur, C.M.D., Passeport, E., Sherwood Lollar, B., Austrins, L.M., Herrera, J., O'Carroll, D.M., 2020. Sulfidated Nano Zerovalent Iron (S-Nzvi) for in Situ Treatment of Chlorinated Solvents: A Field Study. *Water Research*, 174.
- Nur, T., Loganathan, P., Ahmed, M.B., Johir, M.A.H., Nguyen, T.V., Vigneswaran, S., 2019. Removing Arsenic from Water by Coprecipitation with Iron: Effect of Arsenic and Iron Concentrations and Adsorbent Incorporation. *Chemosphere*: 431-438.
- Nurmi, J.T., Tratnyek, P.G., Sarathy, V., Baer, D.R., Amonette, J.E., Pecher, K., Wang, C., Linehan, J.C., Matson, D.W., Penn, R.L., 2005. Characterization and Properties of Metallic Iron Nanoparticles: Spectroscopy, Electrochemistry, and Kinetics. *Environmental Science and Technology*, 39(5): 1221-1230.
- Nzengung, V.A., Castillo, R.M., Gates, W.P., Mills, G.L., 2001. Abiotic Transformation of Perchloroethylene in Homogeneous Dithionite Solution and in Suspensions of Dithionite-Treated Clay Minerals. *Environmental Science and Technology*, 35(11): 2244-2251.
- Opdyke, N.D., Channell, J.E.T., 1996. 3 - Magnetization Processes and Magnetic Properties of Sediments. In: Opdyke, N.D., Channell, J.E.T. (Eds.), *International Geophysics*. Academic Press, pp. 26-48.

- Ouyang, B., Lu, X., Li, J., Liu, H., 2019. Microbial Reductive Transformation of Iron-Rich Tailings in a Column Reactor and Its Environmental Implications to Arsenic Reactive Transport in Mining Tailings. *Science of The Total Environment*, 670: 1008-1018.
- Palleroni, N.J., Bradbury, J.F., 1993. *Stenotrophomonas*, a New Bacterial Genus for *Xanthomonas Maltophilia* (Hugh 1980) Swings Et Al. 1983. *International Journal of Systematic and Evolutionary Microbiology*, 43(3): 606-609.
- Pankow, J.F., Cherry, J.A., 1996. *Dense Chlorinated Solvents and Other Dnaps in Groundwater: History, Behavior, and Remediation*.
- Pantke, C., Obst, M., Benzerara, K., Morin, G., Ona-Nguema, G., Dippon, U., Kappler, A., 2012. Green Rust Formation During Fe(II) Oxidation by the Nitrate-Reducing *Acidovorax* Sp. Strain Bofen1. *Environmental Science and Technology*, 46(3): 1439-46.
- Peretyazhko, T.S., Zachara, J.M., Kukkadapu, R.K., Heald, S.M., Kutnyakov, I.V., Resch, C.T., Arey, B.W., Wang, C.M., Kovarik, L., Phillips, J.L., Moore, D.A., 2012. Perchnetate (Tco_4^-) Reduction by Reactive Ferrous Iron Forms in Naturally Anoxic, Redox Transition Zone Sediments from the Hanford Site, USA. *Geochimica et Cosmochimica Acta*, 92: 48-66.
- Pham, H.T., Chihiro, I., 2019. Chlorinated Benzenes and Benzene Degradation in Aerobic Pyrite Suspension. vol. 45(No 1): 115-125-115-125.
- Phillips, E.J., Lovley, D.R., 1987. Determination of Fe (Iii) and Fe (Ii) in Oxalate Extracts of Sediment. *Soil Science Society of America Journal*, 51(4): 938-941.
- Plagentz, V., Ebert, M., Dahmke, A., 2006. Remediation of Ground Water Containing Chlorinated and Brominated Hydrocarbons, Benzene and Chromate by Sequential Treatment Using Zvi and Gac. *Environmental Geology*, 49(5): 684-695.
- Posfai, M., Buseck, P.R., Bazylinski, D.A., Frankel, R.B., 1998. Reaction Sequence of Iron Sulfide Minerals in Bacteria and Their Use as Biomarkers. *Science*, 280(5365): 880-3.
- Poulton, S.W., Canfield, D.E., 2005. Development of a Sequential Extraction Procedure for Iron: Implications for Iron Partitioning in Continentally Derived Particulates. *Chemical Geology*, 214(3-4): 209-221.
- Poulton, S.W., Krom, M.D., Raiswell, R., 2004. A Revised Scheme for the Reactivity of Iron (Oxyhydr) Oxide Minerals Towards Dissolved Sulfide. *Geochimica et Cosmochimica Acta*, 68(18): 3703-3715.
- Power, G., Ritchie, I., 1983. Mixed Potentials: Experimental Illustrations of an Important Concept in Practical Electrochemistry. *Journal of Chemical Education*, 60(12): 1022.

- Puigserver, D., Herrero, J., Nogueras, X., Cortés, A., Parker, B.L., Playà, E., Carmona, J.M., 2022. Biotic and Abiotic Reductive Dechlorination of Chloroethenes in Aquitards. *Science of The Total Environment*, 816: 151532.
- Qafoku, N.P., Gartman, B.N., Kukkadapu, R.K., Arey, B.W., Williams, K.H., Mouser, P.J., Heald, S.M., Bargar, J.R., Janot, N., Yabusaki, S., Long, P.E., 2014. Geochemical and Mineralogical Investigation of Uranium in Multi-Element Contaminated, Organic-Rich Subsurface Sediment. *Applied Geochemistry*, 42: 77-85.
- Qafoku, N.P., Kukkadapu, R.K., McKinley, J.P., Arey, B.W., Kelly, S.D., Wang, C., Resch, C.T., Long, P.E., 2009. Uranium in Framboidal Pyrite from a Naturally Bioreduced Alluvial Sediment. *Environmental Science and Technology*, 43(22): 8528-8534.
- Qafoku, O., Pearce, C.I., Neumann, A., Kovarik, L., Zhu, M., Ilton, E.S., Bowden, M.E., Resch, C.T., Arey, B.W., Arenholz, E., Felmy, A.R., Rosso, K.M., 2017. Tc(VII) and Cr(VI) Interaction with Naturally Reduced Ferruginous Smectite from a Redox Transition Zone. *Environmental Science and Technology*, 51(16): 9042-9052.
- Qiao, W., Luo, F., Lomheim, L., Mack, E.E., Ye, S., Wu, J., Edwards, E.A., 2018. A Dehalogenimonas Population Respires 1,2,4-Trichlorobenzene and Dichlorobenzenes. *Environmental Science and Technology*, 52(22): 13391-13398.
- Quiton, K.G.N., Lu, M.-C., Huang, Y.-H., 2021. Synthesis and Catalytic Utilization of Bimetallic Systems for Wastewater Remediation: A Review. *Chemosphere*, 262: 128371.
- Radianingtyas, H., Robinson, G.K., Bull, A.T., 2003. Characterization of a Soil-Derived Bacterial Consortium Degrading 4-Chloroaniline. *Microbiology*, 149(11): 3279-3287.
- RAE, 2010. Correction Factors, Ionization Energies*, and Calibration Characteristics. Technical Notes TN-106.
- Raju, S.C., Lagström, S., Ellonen, P., De Vos, W.M., Eriksson, J.G., Weiderpass, E., Rounge, T.B., 2018. Reproducibility and Repeatability of Six High-Throughput 16s Rdna Sequencing Protocols for Microbiota Profiling. *Journal of Microbiological Methods*, 147: 76-86.
- Rasigraf, O., van Helmond, N.A.G.M., Frank, J., Lenstra, W.K., Egger, M., Slomp, C.P., Jetten, M.S.M., 2020. Microbial Community Composition and Functional Potential in Bothnian Sea Sediments Is Linked to Fe and S Dynamics and the Quality of Organic Matter. *Limnology and Oceanography*, 65(S1): S113-S133.
- Real, F.J., Benitez, F.J., Rodriguez, C., 2007. Elimination of Benzene and Chlorobenzenes by Photodegradation and Ozonation Processes. *Chemical Engineering Communications*, 194(6): 811-827.

- Rennert, T., Eusterhues, K., De Andrade, V., Totsche, K.U., 2012. Iron Species in Soils on a Mofette Site Studied by Fe K-Edge X-Ray Absorption near-Edge Spectroscopy. *Chemical Geology*, 332: 116-123.
- Rice, E.W., Baird, R.B., Eaton, A.D., Clesceri, L.S., 2017. *Standard Methods for the Examination of Water and Wastewater*, 10. American Public Health Association Washington, DC.
- Rickard, D., Luther, G.W., 1997. Kinetics of Pyrite Formation by the H₂S Oxidation of Iron (II) Monosulfide in Aqueous Solutions between 25 and 125°C: The Mechanism. *Geochimica et Cosmochimica Acta*, 61(1): 135-147.
- Rickard, D., Luther, G.W., 2007. Chemistry of Iron Sulfides. *Chemical Reviews*, 107(2): 514-562.
- Rickard, D., Morse, J.W., 2005. Acid Volatile Sulfide (Avs). *Marine chemistry*, 97(3-4): 141-197.
- Rijal, M.L., Porsch, K., Appel, E., Kappler, A., 2012. Magnetic Signature of Hydrocarbon-Contaminated Soils and Sediments at the Former Oil Field Hänigsen, Germany. *Studia geophysica et geodaetica*, 56(3): 889-908.
- Robertson, W.J., Franzmann, P.D., Mee, B.J., 2000. Spore-Forming, Desulfosporosinus-Like Sulphate-Reducing Bacteria from a Shallow Aquifer Contaminated with Gasolene. *Journal of Applied Microbiology*, 88(2): 248-259.
- Roden, E.E., 2012. *Microbial Iron-Redox Cycling in Subsurface Environments*. Portland Press Limited.
- Rodgers, K.J., Hursthouse, A., Cuthbert, S., 2015. The Potential of Sequential Extraction in the Characterisation and Management of Wastes from Steel Processing: A Prospective Review. *International Journal of Environmental Research and Public Health*, 12(9): 11724-55.
- Rodríguez-Fernández, D., Heckel, B., Torrentó, C., Meyer, A., Elsner, M., Hunkeler, D., Soler, A., Rosell, M., Domènech, C., 2018. Dual Element (C-Cl) Isotope Approach to Distinguish Abiotic Reactions of Chlorinated Methanes by Fe(0) and by Fe(II) on Iron Minerals at Neutral and Alkaline Ph. *Chemosphere*, 206: 447-456.
- Rogers, R., 2015. Chapter Eight - Microbe, Mineral Synergy, and Seafloor Hydrate Nucleation. In: Rogers, R. (Ed.), *Offshore Gas Hydrates*. Gulf Professional Publishing, Boston, pp. 249-296.
- Sander, M., Hofstetter, T.B., Gorski, C.A., 2015. Electrochemical Analyses of Redox-Active Iron Minerals: A Review of Nonmediated and Mediated Approaches. *Environmental Science and Technology*, 49(10): 5862-5878.

- Schaefer, C.E., Ho, P., Berns, E., Werth, C., 2018a. Mechanisms for Abiotic Dechlorination of Trichloroethene by Ferrous Minerals under Oxic and Anoxic Conditions in Natural Sediments. *Environmental Science and Technology*, 52(23): 13747-13755.
- Schaefer, C.E., Ho, P., Berns, E., Werth, C., 2018b. Mechanisms for Abiotic Dechlorination of Trichloroethene by Ferrous Minerals under Oxic and Anoxic Conditions in Natural Sediments. *Environmental Science and Technology*, 52(23): 13747-13755.
- Schaefer, C.E., Ho, P., Berns, E., Werth, C., 2021. Abiotic Dechlorination in the Presence of Ferrous Minerals. *Journal of Contaminant Hydrology*, 241.
- Schaefer, C.E., Ho, P., Gurr, C., Berns, E., Werth, C., 2017. Abiotic Dechlorination of Chlorinated Ethenes in Natural Clayey Soils: Impacts of Mineralogy and Temperature. *Journal of Contaminant Hydrology*, 206: 10-17.
- Schaefer, C.E., Towne, R.M., Lippincott, D.R., Lacombe, P.J., Bishop, M.E., Dong, H., 2015. Abiotic Dechlorination in Rock Matrices Impacted by Long-Term Exposure to Tce. *Chemosphere*, 119: 744-749.
- Schaefer, C.E., Towne, R.M., Lippincott, D.R., Lazouskaya, V., Fischer, T.B., Bishop, M.E., Dong, H., 2013. Coupled Diffusion and Abiotic Reaction of Trichloroethene in Minimally Disturbed Rock Matrices. *Environmental Science and Technology*, 47(9): 4291-4298.
- Schecher, W.D., McAvoy, D.C., 2001. *Mineql+*: A Chemical Equilibrium Modeling System; Version 4.5 for Windows Workbook. Environmental Research Software.
- Scholz, F., Meyer, B., 1994. Electrochemical Solid State Analysis: State of the Art. *Chemical Society Reviews*, 23(5): 341-347.
- Schwertmann, U., Fitzpatrick, R.W., 1993. Iron Minerals in Surface Environments. *Catena Supplement*, 21: 7-7.
- Scouller, R.C., Snape, I., Stark, J.S., Gore, D.B., 2006. Evaluation of Geochemical Methods for Discrimination of Metal Contamination in Antarctic Marine Sediments: A Case Study from Casey Station. *Chemosphere*, 65(2): 294-309.
- Shi, Z., Nurmi, J.T., Tratnyek, P.G., 2011. Effects of Nano Zero-Valent Iron on Oxidation–Reduction Potential. *Environmental Science and Technology*, 45(4): 1586-1592.
- Silvester, E., Charlet, L., Tournassat, C., Gehin, A., Grenèche, J.-M., Liger, E., 2005. Redox Potential Measurements and Mössbauer Spectrometry of Feⁱⁱ Adsorbed onto Feⁱⁱⁱ (Oxyhydr) Oxides. *Geochimica et Cosmochimica Acta*, 69(20): 4801-4815.
- Smoluch, M., Grasso, G., Suder, P., Silberring, J., 2019. *Mass Spectrometry: An Applied Approach*. John Wiley & Sons.

- Soil, A.C.D.-o., Rock, 2017. Standard Practice for Classification of Soils for Engineering Purposes (Unified Soil Classification System) 1. ASTM International.
- Stackebrandt, E., Sproer, C., Rainey, F.A., Burghardt, J., Pauker, O., Hippe, H., 1997. Phylogenetic Analysis of the Genus *Desulfotomaculum*: Evidence for the Misclassification of *Desulfotomaculum Guttoideum* and Description of *Desulfotomaculum Orientis* as *Desulfosporosinus Orientis* Gen. Nov., Comb. Nov. *International Journal of Systematic and Evolutionary Microbiology*, 47(4): 1134-9.
- Stefaniuk, M., Oleszczuk, P., Ok, Y.S., 2016. Review on Nano Zerovalent Iron (Nzvi): From Synthesis to Environmental Applications. *Chemical engineering journal*, 287: 618-632.
- Stefánsson, A., Arnórsson, S., 2002. Gas Pressures and Redox Reactions in Geothermal Fluids in Iceland. *Chemical Geology*, 190(1): 251-271.
- Stefánsson, A., Arnórsson, S., Sveinbjörnsdóttir, Á.E., 2005. Redox Reactions and Potentials in Natural Waters at Disequilibrium. *Chemical Geology*, 221(3-4): 289-311.
- Stolze, L., Zhang, D., Guo, H., Rolle, M., 2019. Model-Based Interpretation of Groundwater Arsenic Mobility During in Situ Reductive Transformation of Ferrihydrite. *Environmental Science and Technology*, 53(12): 6845-6854.
- Straub, K.L., Benz, M., Schink, B., 2001. Iron Metabolism in Anoxic Environments at near Neutral Ph. *FEMS Microbiology Ecology*, 34(3): 181-186.
- Stumm, W., Sulzberger, B., 1992. The Cycling of Iron in Natural Environments: Considerations Based on Laboratory Studies of Heterogeneous Redox Processes. *Geochimica et Cosmochimica Acta*, 56(8): 3233-3257.
- Suarez, M.P., Rifai, H.S., 1999. Biodegradation Rates for Fuel Hydrocarbons and Chlorinated Solvents in Groundwater. *Bioremediation Journal*, 3(4): 337-362.
- Sumner, M., 1994. Measurement of Soil Ph: Problems and Solutions. *Communications in Soil Science & Plant Analysis*, 25(7-8): 859-879.
- Szczepanik, P., Sawlowicz, Z., 2010. Fe-S Mineralization in the Jurassic Biogenic Remains (Czestochowa, Poland). *Geochemistry*, 70(1): 77-87.
- Taillefert, M., Bono, A.B., Luther, G.W., 2000. Reactivity of Freshly Formed Fe(III) in Synthetic Solutions and (Pore)Waters: Voltammetric Evidence of an Aging Process. *Environmental Science and Technology*, 34(11): 2169-2177.
- Tessier, A., Campbell, P.G., Bisson, M., 1979. Sequential Extraction Procedure for the Speciation of Particulate Trace Metals. *Analytical chemistry*, 51(7): 844-851.

- Thamdrup, B., 2000. Bacterial Manganese and Iron Reduction in Aquatic Sediments, *Advances in Microbial Ecology*. Springer, pp. 41-84.
- Thorpe, C.L., Boothman, C., Lloyd, J.R., Law, G.T.W., Bryan, N.D., Atherton, N., Livens, F.R., Morris, K., 2014. The Interactions of Strontium and Technetium with Fe(II) Bearing Biominerals: Implications for Bioremediation of Radioactively Contaminated Land. *Applied Geochemistry*, 40: 135-143.
- Tobiszewski, M., Namieśnik, J., 2012. Abiotic Degradation of Chlorinated Ethanes and Ethenes in Water. *Environmental Science and Pollution Research*, 19(6): 1994-2006.
- Trivedi, P., Axe, L., 2000. Modeling Cd and Zn Sorption to Hydrous Metal Oxides. *Environmental Science and Technology*, 34(11): 2215-2223.
- U.S.EPA, 1980. Ambient Water Quality Criteria for Chlorinated Benzenes.
- U.S.EPA, 1995. Method 502.2: Volatile Organic Compounds in Water by Purge and Trap Capillary Column Gas Chromatography with Photoionization and Electrolytic Conductivity Detectors in Series, Cincinnati, Ohio.
- U.S.EPA, 2002. Method 5035a: Closed-System Purge-and-Trap and Extraction for Volatile Organics in Soil and Waste Samples. US Environmental Protection Agency, Washington, DC, USA.
- U.S.EPA, 2003. Epa Method 5030c (Sw-846): Purge-and-Trap for Aqueous Samples. US Environmental Protection Agency, Washington, DC, USA.
- U.S.EPA, 2012. Integrated Risk Information System (Iris) on Tetrachloroethylene., Washington, DC.
- U.S.EPA, 2014. Sw-846 Test Method 5021a: Volatile Organic Compounds (Vocs) in Various Sample Matrices Using Equilibrium Headspace Analysis. US Environmental Protection Agency, Washington, DC.
- U.S.EPA, 2020. Risk Evaluation for Perchloroethylene
- U.S.EPA., 2007. Method 6200 (Sw-846): Field Portable X-Ray Fluorescence Spectrometry for the Determination of Elemental Concentrations in Soil and Sediment.
- U.S.EPA., 2021. Toxics Release Inventory Program. Tri-Listed Chemicals.
- Ulucan-Altuntas, K., Debik, E., 2020. Dechlorination of Dichlorodiphenyltrichloroethane (Ddt) by Fe/Pd Bimetallic Nanoparticles: Comparison with Nzvi, Degradation Mechanism, and Pathways. *Frontiers of Environmental Science and Engineering*, 14(1).
- URS, 2013. Solid Phase B-Aquifer Material Characterization – Data Review.

- Usman, M., Byrne, J., Chaudhary, A., Orsetti, S., Hanna, K., Ruby, C., Kappler, A., Haderlein, S., 2018a. Magnetite and Green Rust: Synthesis, Properties, and Environmental Applications of Mixed-Valent Iron Minerals. *Chemical Reviews*, 118(7): 3251-3304.
- Usman, M., Byrne, J.M., Chaudhary, A., Orsetti, S., Hanna, K., Ruby, C., Kappler, A., Haderlein, S.B., 2018b. Magnetite and Green Rust: Synthesis, Properties, and Environmental Applications of Mixed-Valent Iron Minerals. *Chemical Reviews*, 118(7): 3251-3304.
- Valencia-Cantero, E., Hernández-Calderón, E., Velázquez-Becerra, C., López-Meza, J.E., Alfaro-Cuevas, R., López-Bucio, J., 2007. Role of Dissimilatory Fermentative Iron-Reducing Bacteria in Fe Uptake by Common Bean (*Phaseolus Vulgaris* L.) Plants Grown in Alkaline Soil. *Plant and Soil*, 291(1-2): 263-273.
- Velimirovic, M., Larsson, P.-O., Simons, Q., Bastiaens, L., 2013. Reactivity Screening of Microscale Zerovalent Irons and Iron Sulfides Towards Different Cations under Standardized Experimental Conditions. *Journal of Hazardous Materials*, 252: 204-212.
- Venkidusamy, K., Megharaj, M., 2016. Identification of Electrode Respiring, Hydrocarbonoclastic Bacterial Strain *Stenotrophomonas Maltophilia* Mk2 Highlights the Untapped Potential for Environmental Bioremediation. *Frontiers in microbiology*, 7: 1965-1965.
- Vivier, V., Cachet-Vivier, C., Mezaille, S., Wu, B., Cha, C., Nedelec, J.Y., Fedoroff, M., Michel, D., Yu, L., 2000. Electrochemical Study of Bi₂O₃ and Bi₂O₂Co₃ by Means of a Cavity Microelectrode. I. Observed Phenomena and Direct Analysis of Results. *Journal of The Electrochemical Society*, 147(11): 4252-4262.
- Wan, J., Li, Z., Lu, X., Yuan, S., 2010. Remediation of a Hexachlorobenzene-Contaminated Soil by Surfactant-Enhanced Electrokinetics Coupled with Microscale Pd/Fe Prb. *Journal of Hazardous Materials*, 184(1): 184-190.
- Weatherill, J.J., Atashgahi, S., Schneidewind, U., Krause, S., Ullah, S., Cassidy, N., Rivett, M.O., 2018. Natural Attenuation of Chlorinated Ethenes in Hyporheic Zones: A Review of Key Biogeochemical Processes and in-Situ Transformation Potential. *Water Research*, 128: 362-382.
- Weerasooriya, R., Dharmasena, B., 2001. Pyrite-Assisted Degradation of Trichloroethene (Tce). *Chemosphere*, 42(4): 389-396.
- Whiting, K., Evans, P.J., Lebrón, C., Henry, B., Wilson, J.T., Becvar, E., 2014. Factors Controlling in Situ Biogeochemical Transformation of Trichloroethene: Field Survey. *Groundwater Monitoring and Remediation*, 34(3): 79-94.
- Wilkins, M.J., Livens, F.R., Vaughan, D.J., Lloyd, J.R., 2006. The Impact of Fe(II)-Reducing Bacteria on Uranium Mobility. *Biogeochemistry*, 78(2): 125-150.

- Wolfe, A.L., Liu, R., Stewart, B.W., Capo, R.C., Dzombak, D.A., 2007. A Method for Generating Uniform Size-Segregated Pyrite Particle Fractions. *Geochemical Transactions*, 8: 9-9.
- Xing, J., Tan, W., He, H., 2021. Morphology Dominated Rapid Oxidation of Framboidal Pyrite. *R. Du*, 2, 3, H. Xian, 2.
- Xiu, W., Yu, X., Guo, H., Yuan, W., Ke, T., Liu, G., Tao, J., Hou, W., Dong, H., 2019. Facilitated Arsenic Immobilization by Biogenic Ferrihydrite-Goethite Biphasic Fe(III) Minerals (Fh-Gt Bio-Bi-Minerals). *Chemosphere*: 755-764.
- Xu, J., Pu, Y., Yang, X.J., Wan, P., Wang, R., Song, P., Fisher, A., 2018. Rapid Removal of Chloroform, Carbon Tetrachloride and Trichloroethylene in Water by Aluminum-Iron Alloy Particles. *Environmental Technology*, 39(22): 2882-2890.
- Xu, Y., Zhang, W.-x., 2000. Subcolloidal Fe/Ag Particles for Reductive Dehalogenation of Chlorinated Benzenes. *Industrial & Engineering Chemistry Research*, 39(7): 2238-2244.
- Yamada, N., Takahashi, J., Sakata, K.i., 2002. The Effects of Cell-Gas Impurities and Kinetic Energy Discrimination in an Octopole Collision Cell ICP-MS under Non-Thermalized Conditions. *Journal of Analytical Atomic Spectrometry*, 17(10): 1213-1222.
- Yang, Z., Xu, X., Dai, M., Wang, L., Shi, X., Guo, R., 2017. Accelerated Ciprofloxacin Biodegradation in the Presence of Magnetite Nanoparticles. *Chemosphere*, 188: 168-173.
- Yin, X., Hua, H., Burns, F., Fennell, D., Dyer, J., Landis, R., Axe, L., 2021. Identifying Redox Transition Zones in the Subsurface of a Site with Historical Contamination. *Science of The Total Environment*, 762: 143105.
- Yu, J., Liu, Q., Liu, L., Chen, J., 2017. Cloning and Characterization of Dichloromethane Dehalogenase from *Methylobacterium Rhodesianum* for Dichloromethane Degradation. *Bioremediation Journal*, 21(2): 71-80.
- Yu, K., Rinklebe, J., 2013. Soil Redox Potential and Ph Controllers. *Methods in Biogeochemistry of Wetlands(methodsinbiogeo)*: 107-116.
- Yu, R., Andrachek, R.G., Lehmicke, L.G., Freedman, D.L., 2018. Remediation of Chlorinated Ethenes in Fractured Sandstone by Natural and Enhanced Biotic and Abiotic Processes: A Crushed Rock Microcosm Study. *Science of The Total Environment*, 626: 497-506.
- Yu, Z.G., Orsetti, S., Haderlein, S.B., Knorr, K.H., 2016. Electron Transfer between Sulfide and Humic Acid: Electrochemical Evaluation of the Reactivity of Sigma-Aldrich Humic Acid toward Sulfide. *Aquatic Geochemistry*, 22(2): 117-130.

- Zachara, J.M., Kukkadapu, R.K., Fredrickson, J.K., Gorby, Y.A., Smith, S.C., 2002. Biomineralization of Poorly Crystalline Fe (Iii) Oxides by Dissimilatory Metal Reducing Bacteria (Dmrb). *Geomicrobiology Journal*, 19(2): 179-207.
- Zegeye, A., Bonneville, S., Benning, L.G., Sturm, A., Fowle, D.A., Jones, C., Canfield, D.E., Ruby, C., MacLean, L.C., Nomosatryo, S., 2012. Green Rust Formation Controls Nutrient Availability in a Ferruginous Water Column. *Geology*, 40(7): 599-602.
- Zhang, J., Ma, T., Feng, L., Yan, Y., Abass, O.K., Wang, Z., Cai, H., 2017. Arsenic Behavior in Different Biogeochemical Zonations Approximately Along the Groundwater Flow Path in Datong Basin, Northern China. *Science of The Total Environment*, 584-585: 458-468.
- Zhang, T., Tremblay, P.L., Chaurasia, A.K., Smith, J.A., Bain, T.S., Lovley, D.R., 2014. Identification of Genes Specifically Required for the Anaerobic Metabolism of Benzene in *Geobacter Metallireducens*. *Front Microbiology*, 5(MAY): 245.
- Zhang, Y., Gao, K., Dang, Z., Huang, W., Reinfelder, J.R., Ren, Y., 2021a. Microbial Reduction of as(V)-Loaded Schwertmannite by *Desulfosporosinus Meridiei*. *Science of The Total Environment*, 764: 144279.
- Zhang, Y., Ozcer, P., Ghoshal, S., 2021b. A Comprehensive Assessment of the Degradation of C1 and C2 Chlorinated Hydrocarbons by Sulfidated Nanoscale Zerovalent Iron. *Water Research*, 201: 117328.
- Zheng, Z., Yuan, S., Liu, Y., Lu, X., Wan, J., Wu, X., Chen, J., 2009. Reductive Dechlorination of Hexachlorobenzene by Cu/Fe Bimetal in the Presence of Nonionic Surfactant. *Journal of Hazardous Materials*, 170(2): 895-901.
- Zhou, Y., Gao, Y., Xie, Q., Wang, J., Yue, Z., Wei, L., Yang, Y., Li, L., Chen, T., 2019. Reduction and Transformation of Nanomagnetite and Nanomaghemite by a Sulfate-Reducing Bacterium. *Geochimica et Cosmochimica Acta*.
- Zhu, M.-X., Chen, K.-K., Yang, G.-P., Fan, D.-J., Li, T., 2016. Sulfur and Iron Diagenesis in Temperate Unsteady Sediments of the East China Sea Inner Shelf and a Comparison with Tropical Mobile Mud Belts (Mmbs). *Journal of Geophysical Research: Biogeosciences*, 121(11): 2811-2828.
- Zwank, L., Elsner, M., Aeberhard, A., Schwarzenbach, R.P., Haderlein, S.B., 2005. Carbon Isotope Fractionation in the Reductive Dehalogenation of Carbon Tetrachloride at Iron (Hydr) Oxide and Iron Sulfide Minerals. *Environmental Science and Technology*, 39(15): 5634-5641.